IMPERIAL COLLEGE LONDON

FEASIBILITY OF THICKNESS MAPPING USING ULTRASONIC GUIDED WAVES

by

Pierre Belanger

A thesis submitted to Imperial College London for the degree of

Doctor of Philosophy

Department of Mechanical Engineering
Imperial College London
London SW7 2AZ

December 2009

Abstract

Detection and sizing of corrosion in pipelines and pressure vessels over large, partially accessible areas is of growing interest in the petrochemical and nuclear industries. Traditionally, conventional ultrasonic thickness gauging and eddy current techniques have been used to precisely measure the thickness in structures. These techniques only allow the measurement of the local thickness under the probe. Consequently obtaining the remnant thickness of a specimen over a large area requires the probe to be scanned, which is a long and tedious process. Moreover, with these techniques, the scanning may become impossible when the area of inspection is inaccessible. There is therefore a need for a rapid, accurate, long range inspection technique to measure the remaining thickness in corrosion patches.

Low frequency guided waves are now routinely used to screen large area of pipes and other structures for cracks and corrosion. Their detection and location capability is very good, but the standard screening technique only gives a rough estimate of the remaining wall thickness. Guided waves have multiple properties which can be used for thickness mapping over large partially accessible areas e.g. dispersion and cutoff frequency thickness product of the high order modes.

The present work aims to demonstrate the potential of guided waves for thickness mapping over large partially accessible areas. It starts with a general introduction on ultrasonic guided waves and a literature review of the different techniques for the evaluation of thickness with guided waves. The severity of the errors introduced in time-of-flight tomography for thickness reconstruction by breaking the assumption of the ray theory are investigated. As these errors are significant, the possibility of using the cutoff property of the high order modes is investigated in a frequency range where the ray theory is valid. It is found that the attenuation due to the scattering of the waves in corrosion is too large for this technique to work. Finally the use of low frequency guided wave for diffraction tomography is examined. Finite element simulations of a 64 element circular array on a plate show that when the scattering mechanism of the object to be reconstructed satisfies the Born approximation the

reconstruction of the thickness is accurate. However the practical implementation is more challenging when the incident field is not known. Experimental results demonstrate that ultimately the scattering from the array of transducer is a major source of error in the tomographic reconstruction, but when there is no scattering from the array of transducers the reconstructions are very similar to the finite element simulations.

Acknowledgements

A number of people have contributed to my personal and professional development and to my well-being during this period.

My deepest thanks to Prof. Peter Cawley for his time, guidance and support as well as his devotion in his activities both in the research group and as a supervisor. My thanks to Prof. Mike Lowe for his dedication to the NDT group and for all the valuable discussions. I am very grateful for having been given the opportunity to work in their NDT research group and have enjoyed the truly stimulating environment.

A special thanks to Dr Francesco Simonetti for his help and advice and without whom the diffraction tomography chapter of this thesis would certainly be very different. To all the people in the NDT Group, thank you for your companionship and support. I would like to specifically thank Dr Frederic Cegla, Dr Daniel Hesse, Dr Jacob Davies, Dr Thomas Clarke, Dr Ken Ma, Dr Tindaro Cicero, Dr Prabhu Rajagopal, Dr Giuseppe Sposito, Dr Matthew Flemming and Mr Anders Løvstad for their friendship.

For inspiration and for their unyielding support, I would like to thank my father, Yvan and my mother, Helene.

Finally, I could not have ever come this far without the contagious happiness, precious support and strength of my wonderful wife Stephanie. Thanks for believing in my dream 4 years ago!

Contents

List of Figures

List of Tables

Chapter 1

Introduction

1.1 Motivation

Corrosion of pipelines, pressure vessels and storage tanks is a very important issue in the petrochemical and nuclear industries. In these industries the pipelines, pressure vessels and storage tanks are often carrying hazardous or valuable liquids. The environmental and economic impacts of any leakage can have severe consequences. The structures that need inspection are often large and only partially accessible. A good example is the inspection of slug catcher lines presented in figure 1.1 (a) which are sitting on large supports as shown in figure 1.1 (b). In order to accurately evaluate the remnant thickness in the pipe at the support, the inspection technique involves lifting the pipe, which is time consuming and can be dangerous. There is therefore a clear need for corrosion detection and sizing over large partially accessible structures.

Traditionally conventional ultrasonic thickness gauging [1] and eddy current techniques [2] have been used to precisely measure the thickness in structures. These techniques only allow the measurement of the local thickness under the probe. Consequently obtaining the remnant thickness of a specimen over a large area requires the probe to be scanned, which is a long and tedious process. Moreover, with these techniques, the scanning may become impossible when the area of inspection is

(*a*) (*b*)

Figure 1.1: *(a) slug catcher lines and (b) close up on a large pipe support. Photographs from Shell Global Solutions.*

inaccessible.

In the last 10 years the ultrasound non-destructive evaluation (NDE) method based on guided wave propagation has seen a gradual transfer from scientific and technological development to the commercial and industrial environments. Successful commercial application was achieved by use of deployable arrays of transducers generating and receiving guided waves in pipelines [3–7], allowing fast screening of these structures and evaluation of loss of cross sectional area. The detection and location capability of low frequency guided waves is very good, but the standard screening technique only gives a rough estimate of the remaining wall thickness. A conventional NDE technique usually then complements the guided wave inspection for exact sizing. Pipeline inspection with such equipment has become widespread and most large oil companies are developing protocols of usage.

Guided waves have interesting properties that can be used for the evaluation of the remnant thickness in the structure they are propagating. The dispersive nature, variation of the velocity with the frequency thickness product, and the cutoff frequency thickness product of the high order modes can both be exploited for thickness evaluation over large areas. The petrochemical industry is particularly interested in mapping the remaining pipe wall over a large area with defects of a diameter 3 to 4 times the pipe wall. Therefore the purpose of this initial study is to investigate the feasibility of guided wave based techniques to map the thickness of a large area where the diameter of the defects is of the order of 60 mm diameter and the separation distance between the source and the sensor is approximately 1 m in a 10 mm plate. The 60 mm diameter defect is seen here as a relatively undemanding case but close enough to reality in a feasibility study. All the results presented in this thesis were obtained on plates, but the conclusions also apply to large diameter pipes, as in this case the curvature has an insignificant effect on the propagation of guided waves [8].

1.2 Thesis outline

This thesis will follow the sequence of topics described below.

Initially a background on ultrasonic guided waves and a literature review of the different techniques for the evaluation of thickness using guided waves is given in chapter 2.

Chapter 3 investigates the possibility of using ray tomography with low frequency guided waves. A review of the possible points of operation, frequency and guided wave mode, for time-of-flight tomography is presented. However the ray theory is not valid with the possible points of operation for the problem of interest, accurately sizing a 60 mm defect in a 10 mm plate over a propagation distance of approximately 1 m. Therefore the chapter focuses on the severity of the errors introduced by breaking the assumptions of the ray theory. Finite element modelling and experimental results were used to demonstrate that breaking the validity of the ray theory causes serious errors in the reconstruction. The material of this chapter is the basis of a paper published in NDT & E International (P3 in the list of publications).

From the conclusion of chapter 3 the obvious option is to increase the frequency up to the point where the ray theory becomes valid. However the number of modes that can propagate increases with the frequency and the signal processing becomes more complex. Above the cutoff of the higher order modes it is difficult to excite and detect a single mode, as required in time-of-flight tomography. Chapter 4 investigates the possibility of using the cutoff property of the high order guided wave modes to obtain an estimation of the minimum remaining thickness between a source and a sensor. Finite element simulations were used to demonstrate the concept. Experimental results obtained on an accelerated corrosion patch were used to evaluate the attenuation of high frequency guided waves in corrosion.

It is possible to use the low frequency points of operation described in chapter 3 with more complex diffraction tomography algorithms. In contrast, with the time-of-flight straight ray tomography algorithms which reconstruct the thickness from time-of-flight projections, the input to a diffraction tomography algorithm is the wave field scattered by the defects to be imaged. In order to perform a diffraction tomography reconstruction, an approximation of the wave equation must be used to calculate the scattered field from the total and incident fields. The incident field corresponds to the wave field when the structure has no defect whereas the total field is the superposition of the incident and scattered fields. Finite element simulations were used to generate the data and verify the detection, location and sizing capabilties of the technique. The experimental implementation challenges were also studied with an array of transducers. A novel approach in which the incident field is not required to perform a diffraction tomography reconstruction is proposed. The material of this chapter is the basis of a paper submitted to the IEEE Transactions in Ultrasonics, Ferroelectrics and Frequency Control [P5 in the list of publications].

Finally, the conclusions and major contributions of the thesis are outlined in Chapter 6.

Chapter 2

Guided Wave Background and Literature Review

2.1 Ultrasonic Wave Background

Before being able to evaluate the minimum remaining thickness of a structure using ultrasonic waves, a thorough understanding of how waves propagate and interact with defects is necessary. Bulk waves can only propagate far from any boundaries where the longitudinal and shear waves are uncoupled. At the interfaces of the material, the bulk waves interact with these interfaces by means of reflection and refraction. Mode conversion between longitudinal and shear wave can also occur at the interfaces. It is these interactions of bulk waves with the interfaces of the material that lead to the development of elasto-dynamic guided waves (hereafter called guided waves) in a structure. In contrast with bulk waves, a condition for guided waves to develop is the existence of interfaces between two materials. Guided waves are waves that, like light in an optical fibre, are guided by the boundaries of the structure in which they propagate. There are multiple types of guided waves. For example Rayleigh waves are free waves on the surface of a semi-infinite solid [9]. The boundary conditions for this problem are a traction-free surface and the waves must decay with depth from the surface. Another example is Lamb waves which are plane-strain solutions to the free plate problem [10]. Stoneley waves are the waves that occur at the flat interface of two media and decay away from the interface [11]. The basic principles of guided waves are very well known and several textbooks discuss the topic [12–14]. Therefore an extensive review is omitted and only the main characteristics are reviewed in this chapter.

2.1.1 Wave Propagation in Bulk Media

The propagation of elastic waves in infinite isotropic media is well documented in textbooks [14–16]. Therefore here the principal equations are briefly outlined.

The equation of motion for an isotropic elastic medium in the absence of body forces (Navier's equation) is

$$(\lambda + \mu)\nabla\nabla \cdot \mathbf{u} + \mu\nabla^2\mathbf{u} = \rho\frac{\partial^2\mathbf{u}}{\partial t^2} \tag{2.1}$$

where $\mathbf{u}$ is the three dimensional displacement vector, ρ is the material density, λ and μ are the Lamé constants and the ∇^2 is the three dimensional Laplace operator.

Using the Helmholtz decomposition, $\mathbf{u}$ can be expressed as the sum of the gradient of a scalar, ϕ and the curl of a vector potential, $\mathbf{\Phi}$,

$$\mathbf{u} = \nabla\phi + \nabla \times \mathbf{\Phi} \tag{2.2}$$

where $\mathbf{\Phi}$ has zero divergence or

$$\nabla \cdot \mathbf{\Phi} = 0. \tag{2.3}$$

Substition of these potential functions into Navier's equation 2.1 means that the equation of motion can be separated into two independent equations; one for the dilatation or equivoluminal motion ϕ

$$\frac{\partial^2\phi}{\partial t^2} = c_l^2\nabla^2\phi, \tag{2.4}$$

which governs longitudinal waves and one for rotational motion $\mathbf{\Phi}$

$$\frac{\partial^2\mathbf{\Phi}}{\partial t^2} = c_s^2\nabla^2\mathbf{\Phi}, \tag{2.5}$$

which governs shear waves. c_l and c_s are the velocities of longitudinal and shear waves in the infinite isotropic medium and can be expressed as

$$c_l = \sqrt{\frac{\lambda + 2\mu}{\rho}} \tag{2.6}$$

$$c_s = \sqrt{\frac{\mu}{\rho}}. \tag{2.7}$$

This reveals that there are only two types of wave which can propagate in an unbounded isotropic medium. Equations 2.4 and 2.5 are independent of each other meaning that longitudinal and shear waves can propagate without interaction in unbounded media. The general solution to equations 2.4 and 2.5 which fully describes the propagation of the two waves is

$$\phi, \mathbf{\Phi} = Ae^{i(k_{l,s}z - \omega t)} \tag{2.8}$$

where z is the spatial coordinate of the wave, t is the time variable, A is an arbitrary wave amplitude constant, ω is the angular frequency and $k_{l,s}$ are the longitudinal and shear wavenumbers which can be expressed as

$$k_{l,s}^2 = \frac{\omega^2}{c_{l,s}^2} \tag{2.9}$$

where $c_{l,s}$ are the longitudinal and shear velocities.

2.1.2 Guided Waves

Two different solutions of the free plate case will now be detailed i.e. the shear horizontal guided waves and the Lamb waves. These two solutions are briefly introduced in what follows. For a more detailed insight see [14, 15].

Shear Horizontal Wave Modes in Plates

Consider a free isotropic plate with thickness b with traction free surfaces as in figure 2.1. These are the boundary conditions to the free plate problem. The solution to the free plate problem by the method of potentials seeks to solve equations 2.4 and

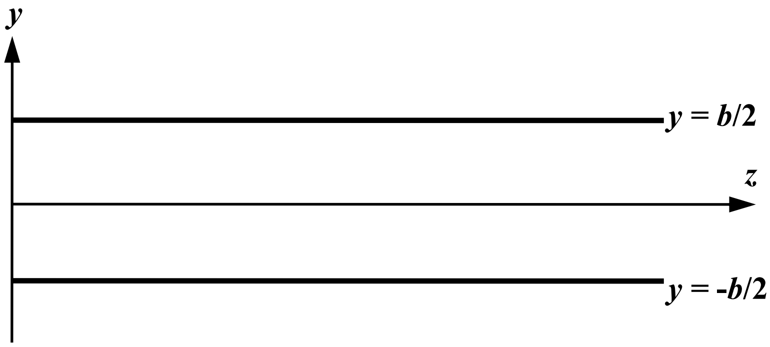

Figure 2.1: *Schematic of a free plate with thickness b and surfaces at $-b/2$ and $b/2$.*

2.5 for the two potentials ϕ and $\mathbf{\Phi}$ respectively. Solutions when the scalar potential ϕ vanishes are known as Shear Horizontal (SH) plate modes.

If the assumption is made that guided waves propagate in the z direction then the solution to equation 2.5 takes the form

$$\mathbf{\Phi} = \mathbf{\Phi}_0(y)e^{i(k_z z - \omega t)}, \tag{2.10}$$

where k_z is the propagation wavenumber. The form of the solution is similar to the form of the general solution expressed in equation 2.8. This solution is a function of y and represents waves traveling in the z direction. Substitution of the assumed potential into equation 2.5 yields an equation for the unknown potential in terms of through-thickness sinusoids

$$\mathbf{\Phi}_0(y) = \mathbf{A}\sin(k_y y) + \mathbf{B}\sin(k_y y), \tag{2.11}$$

where

$$k_y^2 = k_s^2 - k_z^2, \tag{2.12}$$

where k_s is the bulk shear wavenumber introduces in equation 2.9 and k_y is the through-thickness wavenumber. The strain-displacement relations are used to find the strains in terms of the unknown vector potential $\mathbf{\Phi}$. Then Hooke's law is used to find the stresses in terms of the strains and hence in terms of the unknown potential. The boundary conditions state that the surfaces are traction free which leads to the condition that

$$(\lambda + \mu)\frac{\partial v_x}{\partial y} = (\lambda + \mu)\frac{\partial}{\partial y}\left(\frac{\partial}{\partial y}\Phi_z + ik_z\Phi_y\right) = 0 \tag{2.13}$$

at $y = b/2$ and $y = -b/2$. A thorough analysis is presented in [15]. Substition of the potential 2.11 shows that equation 2.13 is satisfied when

$$k_y = \frac{p\pi}{b}, \tag{2.14}$$

where p is an integer from 0 to infinity. Then by substituting equations 2.9 and 2.14 in 2.12 an expression for k_z is obtained

$$k_z^2 = \left(\frac{\omega}{c_s}\right)^2 - \left(\frac{p\pi}{b}\right)^2. \tag{2.15}$$

By using the definition of wavenumber $k_z = \omega/c_p$, where c_p is the phase velocity of the mode of interest, equation 2.15 can be solved for the phase velocity in terms of the frequency thickness product

$$c_p(fb) = \pm 2c_s\left(\frac{fb}{\sqrt{4(fb)^2 - p^2c_s^2}}\right). \tag{2.16}$$

When $p = 0$, corresponding to the zeroth-order SH mode (SH_0) the phase velocity c_p is equal to c_s. The velocity of SH_0 is therefore constant for any frequency thickness product. For all other SH modes ($p > 0$) the phase velocity is varying with the frequency thickness product. The phenomenon of a changing phase velocity with frequency is called dispersion, and results in the distortion of the shape of a wave packet containing multiple frequencies that propagates for long distances. The distortion of the shape of a wave packet generally reduces the signal amplitude and increases the length of the time domain signal. These effects are both detrimental to long range propagation of ultrasonic guided waves. This is therefore a very important effect that has to be taken care of when working with long range guided wave applications. Traditionally guided waves have been mainly used in non-dispersive regions [17,18] to avoid the distortion of the signals. The SH mode dispersion curves for the first few modes generated using equation 2.16 are shown in figure 2.2 for aluminium ($c_s = 3130$ m/s). The phase velocity of all the SH modes converge to c_s as the frequency thickness product becomes large. Mode cutoffs occur at specific frequency thickness products for modes higher than SH_0. At these frequency thickness products, the phase velocity approaches infinity. The cutoff frequency thickness products of the high order SH modes (SH_1, SH_2, ...) can be found by setting the

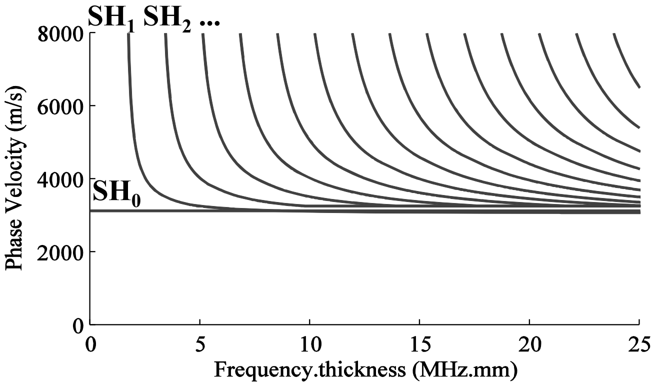

Figure 2.2: *Phase velocity dispersion curves for the SH modes in an aluminium plate (c_s = 3130 m/s).*

denominator in equation 2.16 equal to zero. The cutoff frequency product of the p^{th} is therefore given by

$$fb_p = \frac{pc_s}{2}, \tag{2.17}$$

where p is an integer. If the excitation is below the cutoff frequency thickness product of a given mode then no energy of that mode will propagate. This property of the SH modes will be further investigated for thickness mapping in chapter 4.

The phase velocity represents the velocity at which a mode at a given frequency is traveling in a medium. If this mode is dispersive, then the group velocity is associated with the propagation velocity of a group of waves of similar frequency. The group velocity corresponds to the velocity at which the energy of a multi-frequency wave packet is traveling. By differentiating equation 2.15 and after some algebra an expression for the group velocity is obtained [14]

$$c_g(fb) = c_s\sqrt{1 - \frac{(p/2)^2}{(fb/c_s)^2}}. \tag{2.18}$$

Figure 2.3 presents the group velocity dispersion curves for an aluminium plate.

Lamb Wave Modes in Plates

Lamb wave modes are formed from the combination of vertically polarised shear waves (SV) and longitudinal waves (P). SV and P waves cannot exist individually in

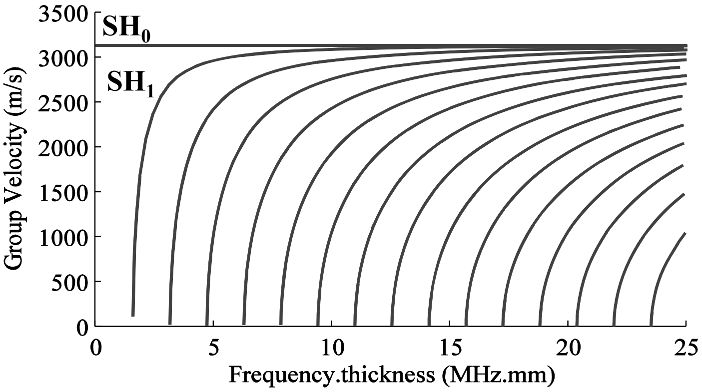

Figure 2.3: *Group velocity dispersion curves for the SH modes in an aluminium plate (c_s = 3130 m/s).*

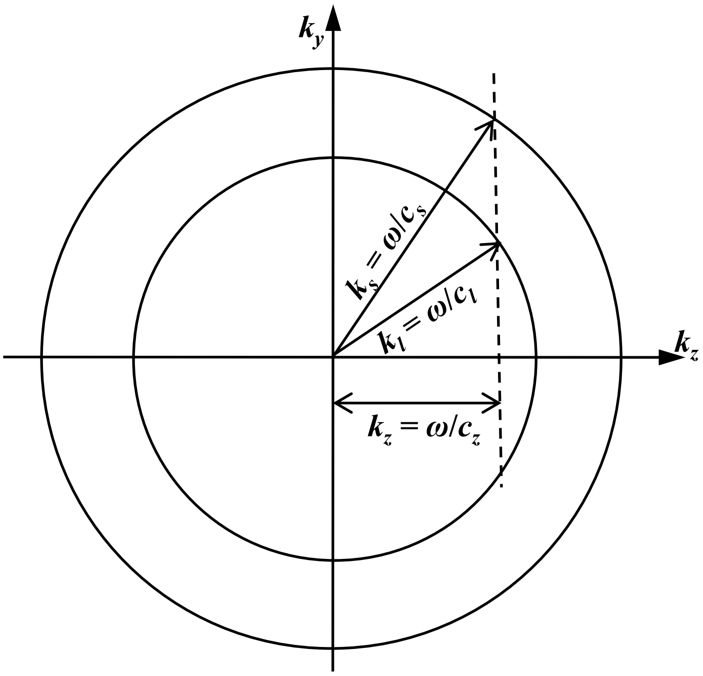

Figure 2.4: *Wavenumber graphical representation of the free plate dispersion relation for coupled SV and P partial waves.*

the free plate case but are coupled, making the solution more complex. The traction free surfaces at $y = \pm b/2$ of figure 2.1 leads to the condition that both SV and P wave vectors must have the same wavevector component in the z direction [15]. This is illustrated graphically in figure 2.4. The two wavevectors prescribe two different circles of radii k_s and k_l whose axial component k_z must match to obtain a propagating modal solution. Some geometric algebra, see for example [15], leads to the Rayleigh-Lamb frequency equations

$$\frac{\tan k_{ys}b/2}{\tan k_{yl}b/2} = -\frac{4k_z^2 k_{ys} k_{yl}}{(k_{ys}^2 - k_z^2)^2} \tag{2.19}$$

for the symmetric modes and

$$\frac{\tan k_{ys}b/2}{\tan k_{yl}b/2} = -\frac{(k_{ys}^2 - k_z^2)^2}{4k_z^2 k_{ys} k_{yl}} \tag{2.20}$$

for the antisymmetric modes. The transverse wavevector components are linked to ω and the z component of the wavevector by

$$k_{ys}^2 = k_s^2 - k_z^2 = \left(\frac{\omega}{c_s}\right)^2 - k_z^2 \tag{2.21}$$

and

$$k_{yl}^2 = k_l^2 - k_z^2 = \left(\frac{\omega}{c_l}\right)^2 - k_z^2. \tag{2.22}$$

The dispersion relations of the Lamb waves can be obtained by substituting equations 2.21 and 2.22 in equation 2.19 for the symmetric (S) modes or in equation 2.20 for the antisymmetric (A) modes. The dispersion relations are transcendental and are solved numerically, for example, using DISPERSE [19]. Figure 2.5 shows (a) the phase velocity and (b) the group velocity of the Lamb wave symmetric and antisymmetric modes for aluminium with $c_s = 3130$ m/s and $c_l = 6320$ m/s. In contrast with the SH modes the Lamb modes are all dispersive. The phase velocity of the fundamental symmetric and antisymmetric modes (S_0 and A_0) converges to c_R, the Rayleigh wave velocity of the material, and all the other Lamb modes converge to c_s, the shear wave velocity of the material. The high order Lamb modes also exhibit a frequency thickness product cutoff. As for the SH modes, the phase velocity approaches infinity as the group velocity approaches zero. These frequency thickness products occur whenever a standing longitudinal or shear waves are present across the thickness of the plate [13]. The dispersive property of the fundamental Lamb modes will be further investigated in chapters 3 and 5 for time-of-flight and diffraction tomography.

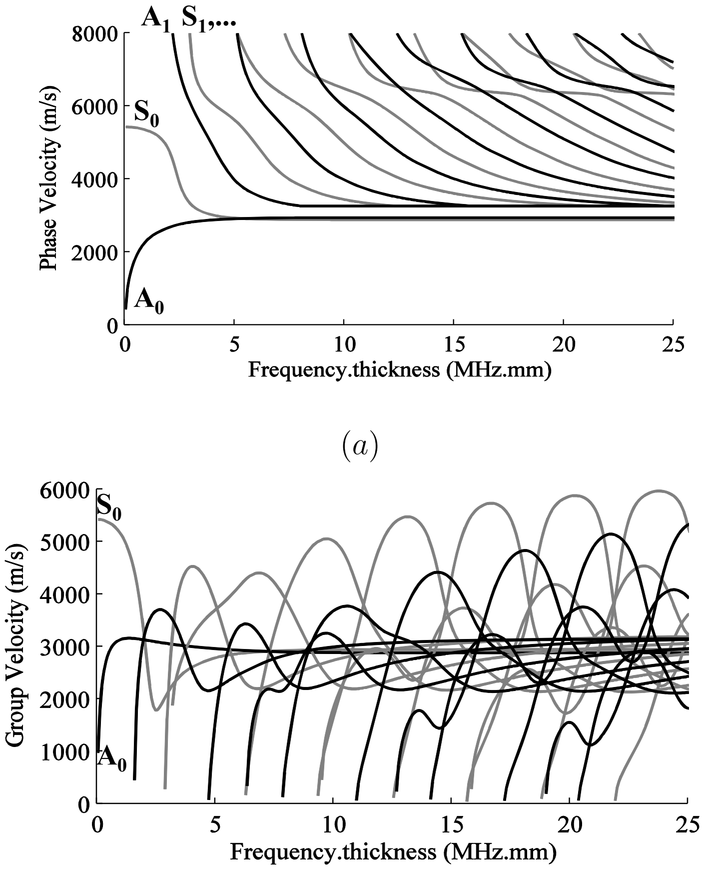

(a)

(b)

Figure 2.5: *(a) Phase velocity and (b) group velocity dispersion curves for the Lamb wave symmetric and antisymmetric modes in an aluminium plate (c_s = 3130 m/s and c_l = 6320 m/s).*

2.2 Literature Review of Thickness Mapping using Guided Waves

This section reviews the literature on the use of guided waves for thickness measurement over large areas using different properties of guided waves.

2.2.1 Ray Tomography

Tomography is derived from the Greek word $\tau o \mu o s$ which means slice. It is a method which aims at recovering the cross-section of an object from projection data. A

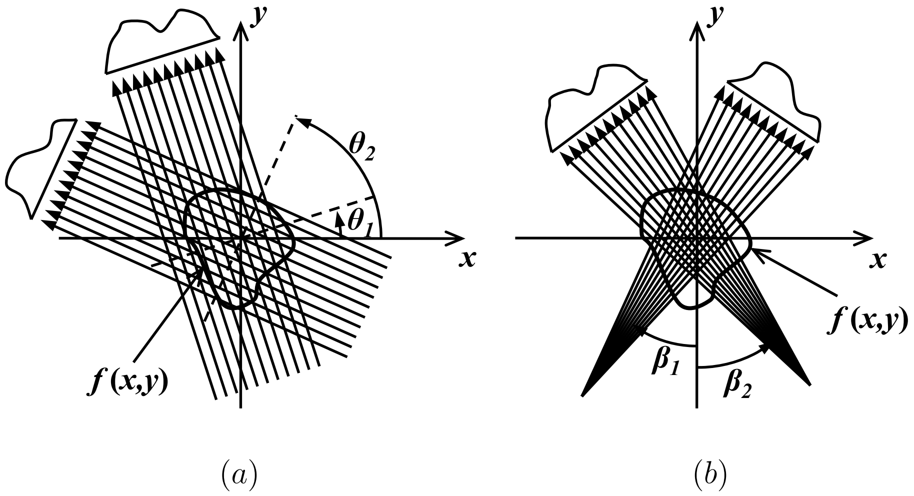

Figure 2.6: *(a) Two parallel projections at different angles and (b) two fan beam projections at different angles.*

projection corresponds to a set of line integrals of a given parameter through an object at a given angle. The reconstruction of a function from its projections was first achieved in a paper by Radon in 1917 [20]. Fifty-five years later Hounsfield received a Nobel prize for the invention of the first x-ray computed tomography scanner. Since the invention of Hounsfield, research on tomographic imaging has been focusing on new applications as well as faster and more accurate reconstruction algorithms.

There are two main bodies of literature in tomography. The first is medical imaging and is primarily concerned with computed tomography scanning. Hounsfield developed an iterative algorithm for his scanner; however, medical imaging research has, since then, focused on convolution backprojection algorithms. The convolution backprojection algorithms are well suited to only two scanning geometries: the parallel beam and the fan beam, see figure 2.6. These algorithms take advantage of the scanning geometry and the Fourier Slice theorem [21] to reconstruct the unknown object.

The second body of literature is geophysical imaging. Geophysical tomography differs from medical tomography in terms of the physical scale but also of the scanning geometry. It would be impossible to use a parallel or fan beam geometry for geophysical tomography. Consequently this field of imaging carried on developing the iterative methods first presented by Hounsfield. They developed iterative algorithms that are more general than the convolution backprojection algorithms because they can work with random scanning geometries. Some scanning geometries are however more suitable than others. Ray tomography is investigated in the context of guided wave time-of-flight tomography in chapter 3.

Convolution Backprojection Algorithms

The convolution backprojection algorithms were first presented by Ramachandran and Lakshminarayanan [22] in 1971 and later developed and popularized by Shepp and Logan [23] in 1974. The algorithm was originally dedicated to the parallel beam scanning geometry.

The filtered backprojection is an algorithm developed in straight-ray medical tomography. The straight-ray assumption implies that the ray paths are not influenced by the inhomogeneities in the specimen. As the name implies, the filtered backprojection is a two step algorithm: the filtering and the backprojection steps. This algorithm takes advantage of the Fourier Slice theorem. A schematic of the theorem is presented in figure 2.7. This theorem is stated as [21]:

> The Fourier transform of a parallel projection of an object $f(x, y)$ taken at an angle θ gives a slice of the two-dimensional transform $F(u, v)$, subtending an angle θ with the u-axis.

This theorem is valid for parallel beam geometry and only in the case of straight-ray tomography. In the frequency domain, the Fourier transform of a parallel projection is bandlimited to Ω which is a function of the sampling in the space domain and is given by equation 2.23.

$$\Omega = \frac{\pi}{\Delta t} \tag{2.23}$$

where Δt is the distance between each transducer.

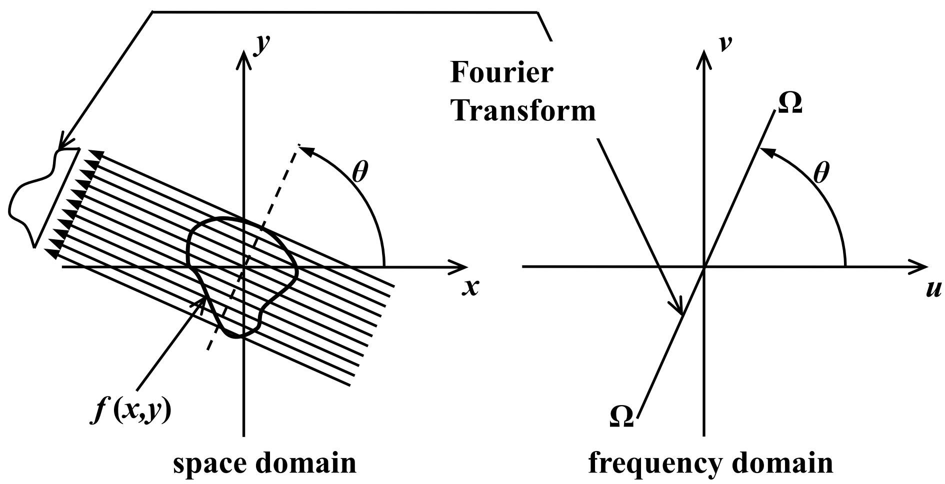

Figure 2.7: *Schematic of the Fourier Slice theorem.*

The idea of the filtered backprojection is to calculate projections at as many angles θ as possible to obtain a discrete estimate of the two-dimensional Fourier transform of the object. Then the object is recovered by taking the inverse Fourier transform of this discrete estimate of the two-dimensional Fourier transform of the object.

Jansen and Hutchins [24] were the first to publish on Lamb wave tomography in 1990. They inspected a 0.688 mm aluminum sheet immersed in a water bath. They suspended above the plate two immersion transducers, inclined at the critical angle for the generation of the desired Lamb wave mode. The transducers were separated by a distance of 120 mm and they were scanned across the surface by a stepping motor system to create the parallel projections. They investigated tomography using the attenuation and the slowness of the S_0 mode. For the attenuation tomography, the energy of S_0 was determined with the Fourier transform of the signal recorded at the receiving transducer. The energy of S_0 was compared with a reference value to obtain the attenuation. For the slowness reconstruction, the time-of-flight of each ray needs to be evaluated. In order to obtain an accurate value they used the cross-correlation between the reference waveform and the data waveform to obtain the time difference due to defects. These two reconstruction parameters were compared for a 5 by 7 mm oval through hole and were implemented with the filtered backprojection algorithm. Each reconstruction was built using 32 projections at different angles over 180° each consisting of 51 rays. The oval shape was detected to some degree in both cases. However the attenuation reconstruction is not as accurate as the slowness reconstruction in terms of the dimensions of the defect. In the attenuation reconstruction the defect area was much larger than the original defect size and this is due to diffraction effects around the defect. They also investigated the reconstruction of a 40% part-through cylindrical hole of 7.8 mm diameter. In this specific case, no significant variations in velocity or attenuation of S_0 were noticed. Hence they decided to use attenuation of the A_1 and S_1 modes and the frequency shift of the centroid of S_1. The frequency shift of the centroid is obtained from the Fourier transform of the signal recorded by the receiving transducer. All reconstructions had a peak at the centre of the part-through hole and they were all equally effective. However the size and depth of the defect cannot be evaluated from this peak because the reconstructions show a defect region much smaller than the original hole. This problem might be solved by increasing the number of rays per projection and the total number of projections.

In 1992 Hutchins et al [25] investigated a slightly different technique. Instead of using inconvenient immersion transducers, they used a Nd:YAG laser to generate the Lamb waves and they compared in-plane and normal motion EMAT transducers for detection. The in-plane motion transducer is used to detect S_0 and the normal motion transducer is used to detect A_0. The excitation frequency was chosen to be below the cut-off of the high order modes so that only the three fundamental modes can propagate. They compared three different reconstruction techniques implemented again with the filtered backprojection algorithm for parallel projections: the attenuation, the slowness and the frequency centroid shift. The sample they used was a 0.68 mm thick aluminium plate containing a 8mm diameter through thickness hole. With both the in-plane and normal motion EMAT the attenuation reconstruction gives a defect larger than the original hole. The slowness and frequency centroid shift methods were the most accurate; the frequency centroid shift being the best of the two.

More recently Wright et al [26] used micromachined silicon air-coupled capacitance transducers to image defects in a 0.69 mm aluminium sheet. They compared two image reconstruction techniques: the attenuation and the shift in centroid frequency for a non-circular defect and for a multiple defects case. The two techniques were implemented with the filtered backprojection algorithm using parallel projections at a frequency below the cut-off of the high order modes. The first case they studied was a through thickness 1 mm by 10 mm slot and the second case was two through thickness holes of 10 mm and 5 mm respectively. In the first case the slot shape was not reproduced accurately, possibly due to the size of the defect in relation to the scan resolution and the wavelength of the chosen Lamb wave mode. In the second case the two defects were resolved, with greater change in attenuation or centroid frequency shift associated with the larger defect. However the shape of the smaller defect was distorted, possibly due to its position inside the image area. It was in fact close to the edge of the image area where the ray density is smaller.

Pei et al [27] used a pair of patented pin transducers (see [28]) to implement tomography with the A_0 mode. The frequency was chosen such that the transducer excites a very pure A_0 mode. They used the time-of-flight together with a filtered backprojection algorithm to reconstruct the slowness of a 1 mm aluminium plate with a 6.4 mm by 12.7 mm 50% part-through slot. They extracted the time-of-flight from the difference in time between the first zero crossing of the input signal and the first zero crossing of the signal recorded by the receiving transducer. From the dispersion relation of the A_0 mode they converted the slowness map into a thickness map. They calculated 60 parallel projections spread over 180° around the object to be reconstructed. Each projection had 64 rays. The slot area was clearly shown on the map but its shape and depth were not reconstructed accurately.

As seen in the references mentioned above, the parallel projection scanning geometry can easily be implemented with the filtered backprojection, however this scanning geometry is not practically convenient because it cannot be carried out with a fixed array of transducers. Figure 2.8 (a) presents the position of the transducers for four projections at different angles. On figure 2.8 each dot represents the location of a transducer, either a receiver or a transmitter required for one of the projection. In reality more than four projections are required to reconstruct an object accurately

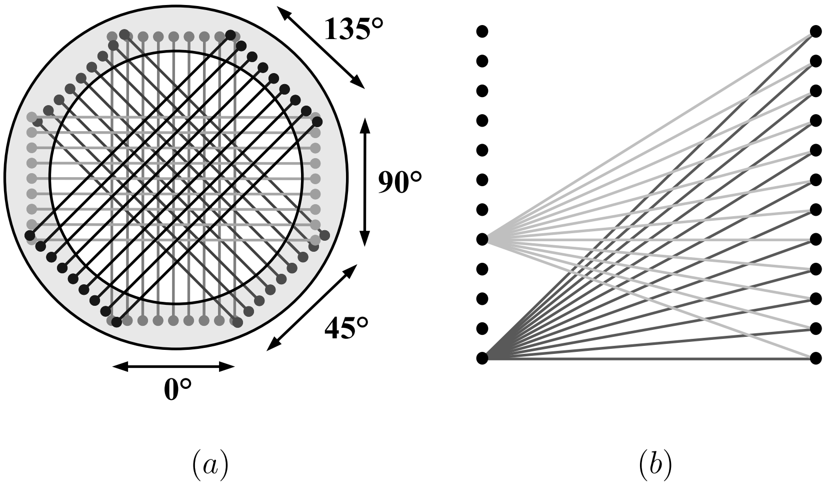

Figure 2.8: *Two possible scanning geometries: (a) the parallel projection and (b) the crosshole.*

and thus the number of transducer required would be too large to be implemented on an array. Hence in order to collect the projections with the minimum number of transducers either the object or the transducers needs to be rotated. McKeon and Hinders [29] compared the parallel projection scanning geometry implemented with the filtered backprojection and the crosshole scanning geometry implemented with an iterative algorithm. The crosshole scanning geometry is presented in figure 2.8 (b). This scanning geometry contains only two lines of transducers, on both sides of the reconstruction area and the signals are recorded between each pair. Their measurements were performed at a frequency thickness product of 2 MHz.mm, where S_0 is the fastest mode. They used the time-of-flight of S_0 to reconstruct the slowness in the image area. One advantage of the crosshole technique is that it requires access to only two sides of the region. However with the crosshole tomography, the ray density varies inside the image area and the rays do not pass through the region of interest from all orientations. The authors claim that these drawbacks in the reconstruction quality are offset by the increased practicality of the measurement. Figure 2.9 presents (a) the reconstruction they obtained with the parallel scanning geometry and (b) with the crosshole scanning geometry where the defect is a 20 cm^2 circular region of 50% thickness reduction in a 2.45 mm thick aluminium plate.

The images covers 100 × 100 mm, in (a) the image was reconstructed from 18

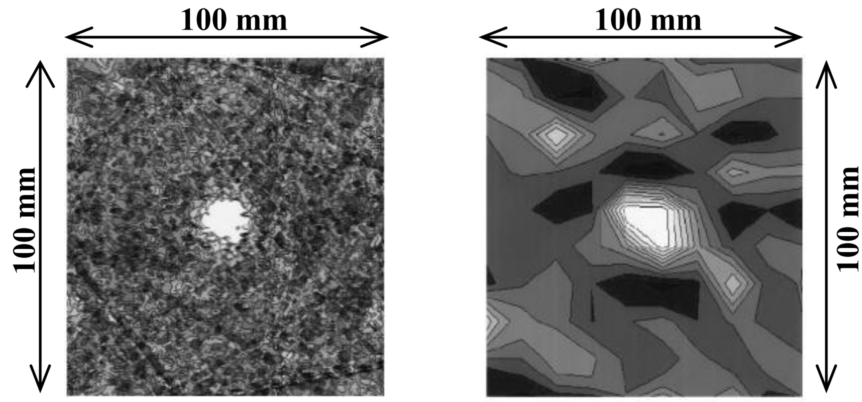

(*a*) (*b*)

Figure 2.9: *The results of McKeon and Hinders [29] obtained for (a) a parallel projection scanning geometry with the filtered backprojection and (b) a crosshole scanning geometry with an iterative algorithm.*

projections of 100 rays for a total of 1800 rays and in (b) it was reconstructed from 400 rays. In (a) the image is noisy but the dimensions of the defect are close to reality. The ray density in (b) is insufficient and the reconstruction is not accurate enough to extract the exact size of the defect.

By slightly modifying the filtered backprojection it can be adapted from the parallel scanning geometry to the fan beam scanning geometry. The advantage of the fan beam is that it can be implemented on a circular array. Thus there is no need to rotate the object or the transducers. Malyarenko and Hinders [30] compared the circular array implementation of the filtered backprojection with a double crosshole scanning geometry implemented with an iterative algorithm. Figure 2.10 presents these two scanning geometries, (a) the circular array and (b) the double crosshole.

The images they obtained with both methods show good quantitative agreement with the defect shape. However, for the circular array, they said that the fraction of the area inside the scanning ring that is free from reconstruction artefacts, the fill factor, is relatively small. This is due to the fact that they used a fast algorithm that makes an approximation that should be avoided if a large fill factor is desired. They concluded that this low fill factor is a serious limitation to the circular array

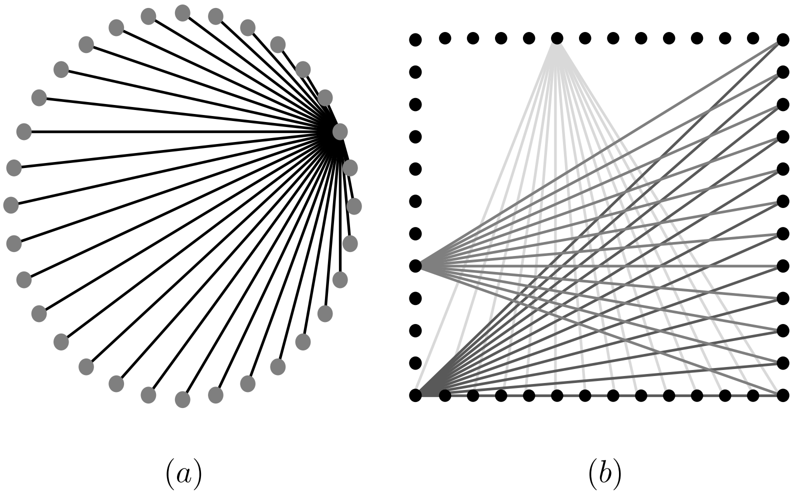

Figure 2.10: *Two possible scanning geometries: (a) the circular array and (b) the double crosshole.*

implementation of the filtered backprojection and that the double crosshole is a more appropriate scanning geometry for Lamb wave tomography.

Iterative Algorithms

As stated above the iterative algorithms were first introduced by Hounsfield in 1972 for the first x-ray computed tomography scanner. However these algorithms were later developed in geophysical imaging. The iterative algorithm approach is completely different from the convolution backprojection approach. To illustrate the principle, assume there is only one transmitter and one receiver as shown in figure 2.11.

In figure 2.11 the arrow represents a straight ray between the transmitter and the receiver. A mesh of square cells is drawn between the two transducers; the idea is to find the path of the ray between the 2 transducers and to calculate the length of the path in each cell. If the ray does not pass in a cell the length in this cell is set to zero. If the velocity of propagation of a wave is assumed constant within a cell than the time-of-flight of a wave is given by

$$T_{estimate} = \sum_{i,j} \frac{d_{i,j}}{Vgr_{i,j}} \tag{2.24}$$

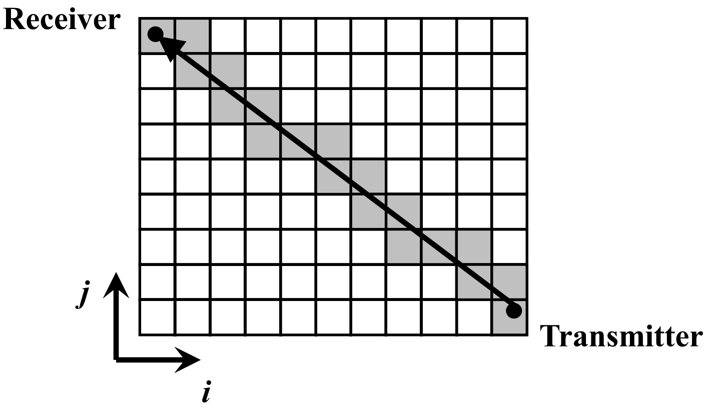

Figure 2.11: *Schematic of the iterative algorithms.*

where $d_{i,j}$ and $Vgr_{i,j}$ are respectively the length and the group velocity in the cell i, j. The estimate of the time-of-flight $T_{estimate}$ is then compared with the measured value and the group velocity for all cells in the path is updated until the estimate and the actual values of the time-of-flight are close together. The principle of the iterative algorithms was illustrated with the time-of-flight but the same procedure can be applied to any other parameters used in tomography.

In the case of the algebraic reconstruction technique (ART) the procedure described above is repeated for all rays. However ART reconstructions usually suffer from noise which is caused by the inconsistencies introduced at each iteration, [21]. The mesh of cells is usually chosen such that there is more than one ray passing through each cell. As a consequence each cell is updated by more than one ray and this results in inconsistencies. An alternative to the ART is the simultaneous iterative reconstruction technique (SIRT). The approach is identical to the ART until the last step. Instead of updating the cells after processing each ray, the cells are updated with the average of all computed changes. This algorithm usually leads to smoother reconstruction at the expense of slower convergence.

As presented previously McKeon and Hinders [29] and Malyarenko and Hinders [30] respectively compared the filtered backprojection implemented on a parallel beam scanning geometry with the ART implemented on a crosshole scanning geometry (see figure 2.8) and the filtered backprojection implemented on a circular array with the SIRT implemented on double crosshole scanning geometry (see figure 2.10). In

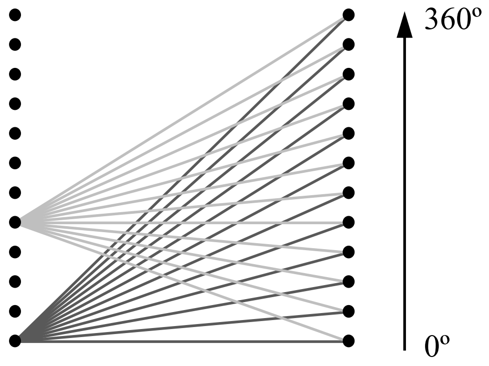

Figure 2.12: *Schematic of a crosshole scanning geometry on a pipe.*

both these investigations they concluded that the iterative methods were superior to the convolution backprojection techniques. Amongst the advantages of the iterative method is its great flexibility, allowing practically any scanning geometry and incomplete data sets. The reconstruction quality of the iterative methods is, though, poorer than the convolution backprojection techniques. However the reconstruction quality drawbacks are offset by the increased practicality of the measurement.

Another advantage of the iterative methods and especially of the crosshole scanning geometry is that it can be applied to pipes. Figure 2.12 presents a schematic of a crosshole scanning geometry on a pipe. The pipe simply has to be unwrapped and the crosshole scanning geometry can be applied; the shortest helical path between a transducer and a receiver needs to be carefully evaluated.

Leonard and Hinders [31, 32] investigated Lamb wave tomography on a steel pipe with an inner radius of 75 mm and an outer radius of 102 mm with SIRT. The distance between the two rings of transducers was 320 mm. The input signal was a 15-cycle toneburst centred at 2.25 MHz. They used the travel time of the first arriving mode, which in their case was the S_6 mode, to reconstruct the slowness and the thickness of the pipe wall. Figure 2.13 shows four reconstructions of a 25% wall thinning of increasing length. The grey horizontal striations and the black criss-cross artifacts indicate the location of the flaws (area contained within the black ellipse), which can be seen to increase in size, as expected. Note that the scans are shown for different angular positions of the flaws, but all other scanning, reconstruction,

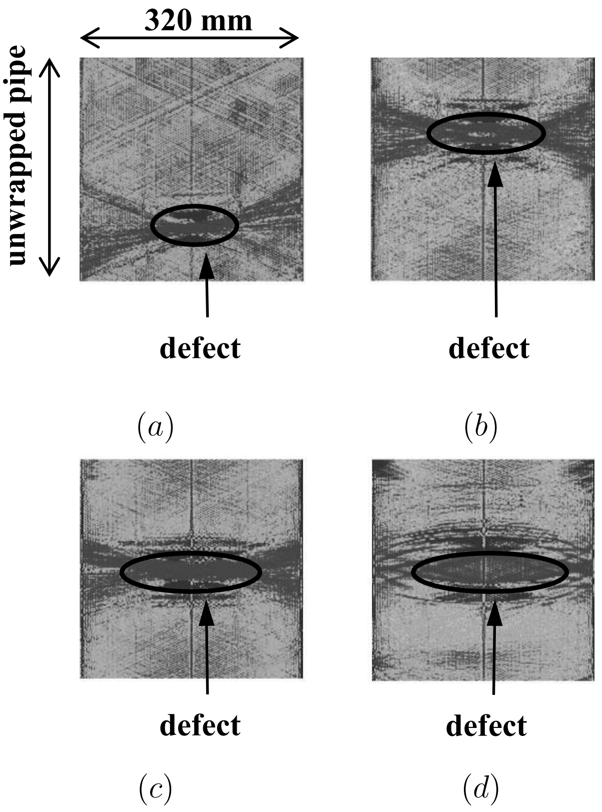

Figure 2.13: *Four reconstructions are shown of a 25% wall thinning increasing in size. Figure from [32].*

and rendering parameters were remained unchanged. The flaw is not clear and its size and depth cannot be evaluated. Hence in order to improve the image quality they examined frequency compounding. This technique can be viewed as a way of enhancing the contrast between the flawed and unflawed region by reconstructing the image for input signals centred at multiple frequencies. Figure 2.14 presents (a) the reconstruction of an irregular 2×2 in^2 gouge on the inner diameter of a steel pipe for a single frequency and (b) when 10 frequencies are compounded. In this case the pipe wall was 20 mm and its outer diameter was 175 mm. The distance between the rings of transducers is again 320 mm. It can be seen that the tomographic frequency compounding technique significantly reduced the noise in the reconstructed images.

The iterative algorithms can be implemented on various types of scanning geometry and they are flexible due to their iterative nature. A major advantage of the iterative algorithms and especially of the crosshole scanning geometry is that it can

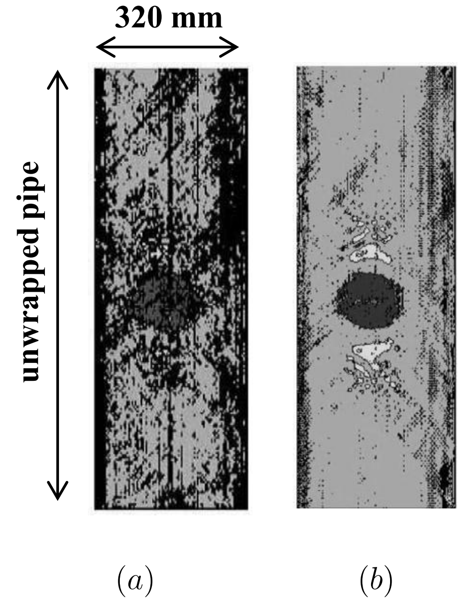

Figure 2.14: *Reconstruction of an irregular gouge on the inner diameter of a steel pipe. (a) single frequency reconstruction and (b) compounded image using 10 frequencies. Figure from [32].*

be implemented to reconstruct an image of a pipe wall. The pipe simply has to be unwrapped and any of the iterative algorithms can then be employed. Frequency compounding was presented as a good technique to enhance the contrast of a tomographic reconstruction and to reduce noise.

2.2.2 Diffraction Tomography

In their investigation McKeon and Hinders [29] and Malyarenko and Hinders [30] recognised that diffraction was a major issue to the successful implementation of low frequency guided wave tomography for thickness mapping in plates or pipes. Assuming that a thickness reduction only causes the frequency thickness product of guided wave to shift to a lower value is only a reasonable assumption when the ray theory is valid. Moreover when the size of the defects is comparable to or smaller than the wavelength of the signal the diffraction effect becomes dominant [21]. When using low frequency guided waves it is common that the defects have dimensions in the range of the wavelength. Diffraction tomography is investigated in the context

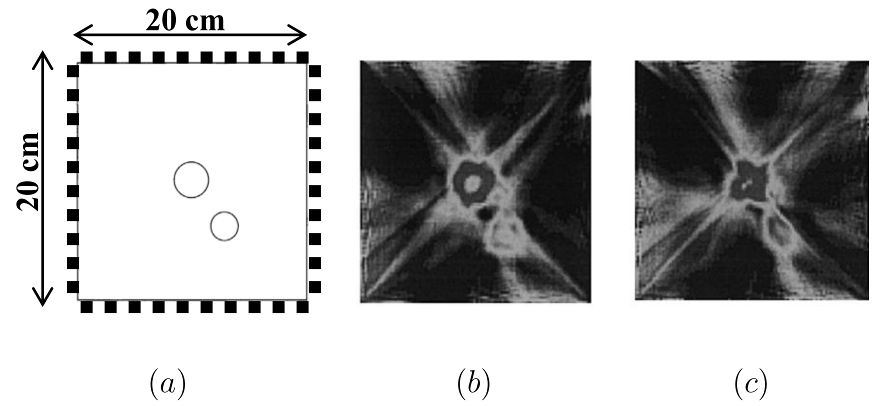

Figure 2.15: *Aluminium plate with two circular thinned areas. The squares are a schematic of the position of the transducer around the reconstructed area. (b) is the straight-ray reconstruction and (c) is the bent ray reconstruction. Figure from [33].*

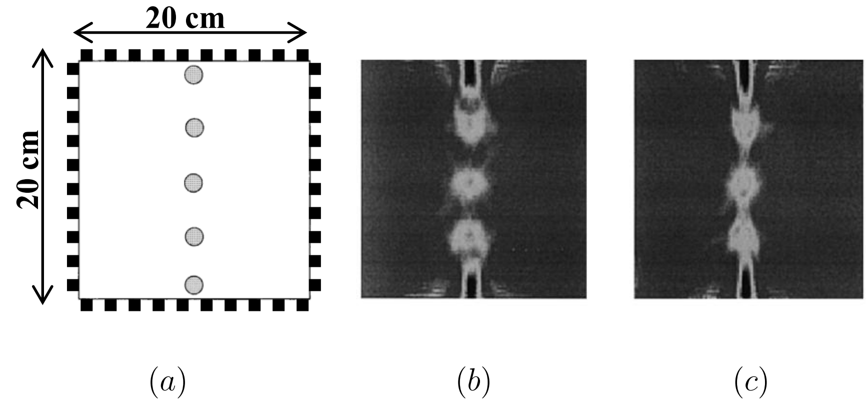

Figure 2.16: *Aluminium plate with five through holes. The squares are a schematic of the position of the transducer around the reconstructed area.(b) is the straight-ray reconstruction and (c) is the bent ray reconstruction. Figure from [33].*

of thickness reconstruction with guided waves in chapter 5.

Malyarenko and Hinders [33] investigated Lamb wave diffraction tomography with SIRT (see the previous subsection). Instead of assuming a straight ray between each transmitter and receiver they compared two ray tracing algorithms: the simulated annealing ray tracing and the iterative shooting ray tracing. Once the bent ray path is obtained the SIRT is exactly the same as the straight ray version. Figures 2.15 to 2.17 present three comparisons of reconstruction with straight ray SIRT (b) and bent ray SIRT (c) for double crosshole reconstructions (see figure 2.10). The area reconstructed is a square of size 20 × 20 cm on an aluminium plate.

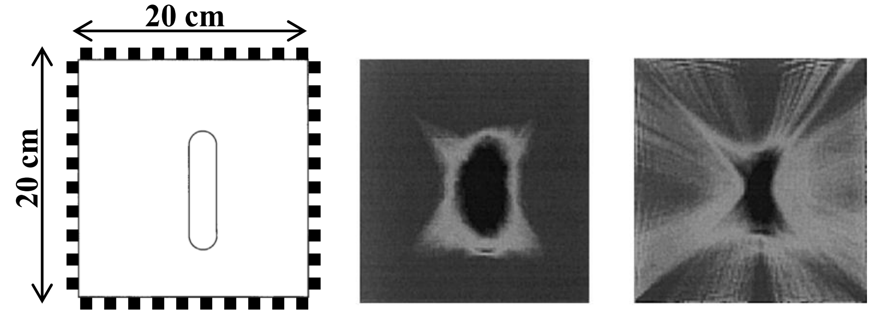

(*a*) (*b*) (*c*)

Figure 2.17: *Aluminium plate with oblong thinned. The squares are a schematic of the position of the transducer around the reconstructed area.(b) is the straight-ray reconstruction and (c) is the bent ray reconstruction. Figure from [33].*

From visual comparison their conclusions are that the size of the defects reconstructed with straight ray SIRT often exceeds reality whereas with bent ray SIRT the defects appear smaller and closer to their actual size. Furthermore the bent ray SIRT partially eliminates the artifacts at the centre of the defect that are visible on the straight ray reconstructions. Both the straight ray and bent ray SIRT have reconstruction artifacts due to non uniform ray density. In the case of straight ray tomography it is possible to have uniform ray density. However if diffraction effects are taken into account the ray bending distorts the uniformity and the distortion grows with the size and severity of the defects. In fact the most severe artifacts are observed on figure 2.17 (c) with the largest defect area and the weakest artifacts are on figure 2.15 (c) where defects are small and do not introduce large changes to the ray density. They found that this distortion can be minimized by sufficient smoothing of the reconstructed image.

For the parallel projection scanning geometry or with a circular array the diffraction effects can be taken into account with the Fourier Diffraction theorem. The Fourier Diffraction theorem relates the Fourier transform of the measured scattered data with the Fourier transform of the object. Figure 2.18 presents a schematic of the Fourier Diffraction theorem. The statement of the theorem is as follows [21]:

> When an object is illuminated with a plane wave, the Fourier transform

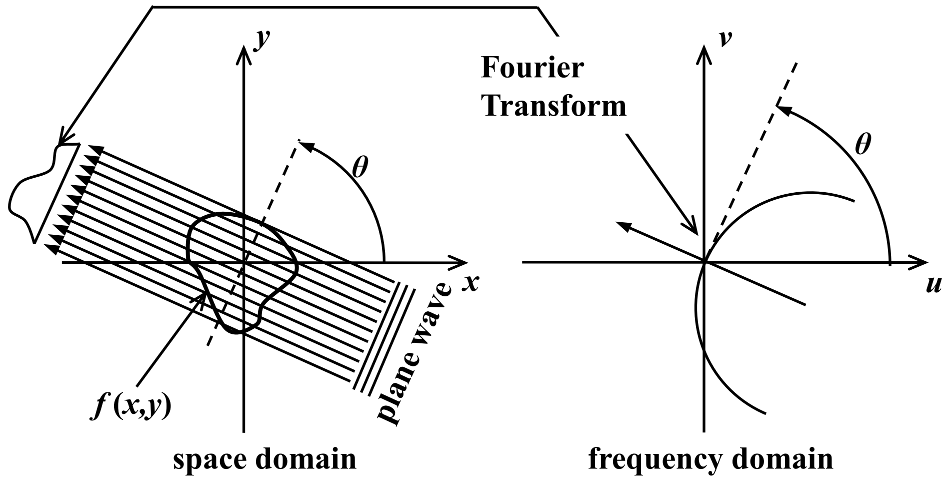

Figure 2.18: *Schematic of the Fourier Diffraction theorem.*

> of the forward scattered field measured on a line gives the values of the 2D Fourier transform of the object along a semicircular arc in the frequency domain.

The radius of the semicircular arc is related to the wavelength. As the frequency increases, the wavelength decreases and the radius of the arc in the Fourier domain increases. By varying the orientation of the plane wave the data can be collected on various semicircular arcs and by varying the frequency of the incident plane wave the data can be collected on arcs of different radius. If the source is much smaller than the wavelength and the object $f(x, y)$ is far from a circular array of transducers the incident wave field can be considered as a plane wave at the object and therefore the Fourier Diffraction theorem applies.

The object is reconstructed from the phase and amplitude of the scattered field. The scattered field corresponds to the field generated by the object when illuminated by an incident field. In a typical implementation of diffraction tomography the total field, or the superposition of the incident and scattered fields is measured. In order to perform a diffraction tomography reconstruction, an approximation of the wave equation must be used to calculate the scattered field. The Born and the Rytov approximations are the most common [34,35]. These approximations can be expressed as

$$\begin{aligned}
\text{Born: } U_a &= U_t - U_i \\
\text{Rytov: } U_a &= U_i \log\left(\frac{U_t}{U_i}\right)
\end{aligned} \tag{2.25}$$

where U_a is the data for the diffraction tomography algorithm when using either the Born or the Rytov approximation, U_t is the total field and U_i is the incident field. Therefore both approximations require the incident field in the evaluation of the scattered field. The incident field corresponds to the wave field that propagates in a structure when there are no inhomogeneities.

The two approximations have quite different validity criteria [36, 37]. For the Born approximation the phase difference between the incident field and the wave propagating through the unknown object must be less than π. Consequently this approximation is only valid for small or low contrast objects, the contrast being defined as the difference between the background medium velocity and the velocity in the unknown object. For the Rytov approximation it is the change in the scattered phase over a wavelength that is important and not the total phase change.

Rohde et al [38] recently examined diffraction tomographic imaging of flexural inhomogeneities i.e. change in thickness, density, Young's modulus or shear modulus in plates within the Born approximation for structural health monitoring applications. Using a structural health monitoring approach greatly simplifies the implementation of diffraction tomography because it implies that baseline measurement can be used as the incident field in the evaluation of the scattered field. Figure 2.19 shows tomographic reconstructions of a circular defect in a 1.02 mm aluminium plate for three different defect diameters and relative thickness changes. The dimension of the thickness map is 100 × 100 mm. In all cases the location, diameter and relative thickness change is accurate, which is a major improvement from the time-of-flight tomography results presented in the previous subsection. A simulated incident field was used in the evaluation of the Born approximation. Parallel linear arrays of sources and sensors were revolved around the area of inspection to obtain the data required for the reconstruction.

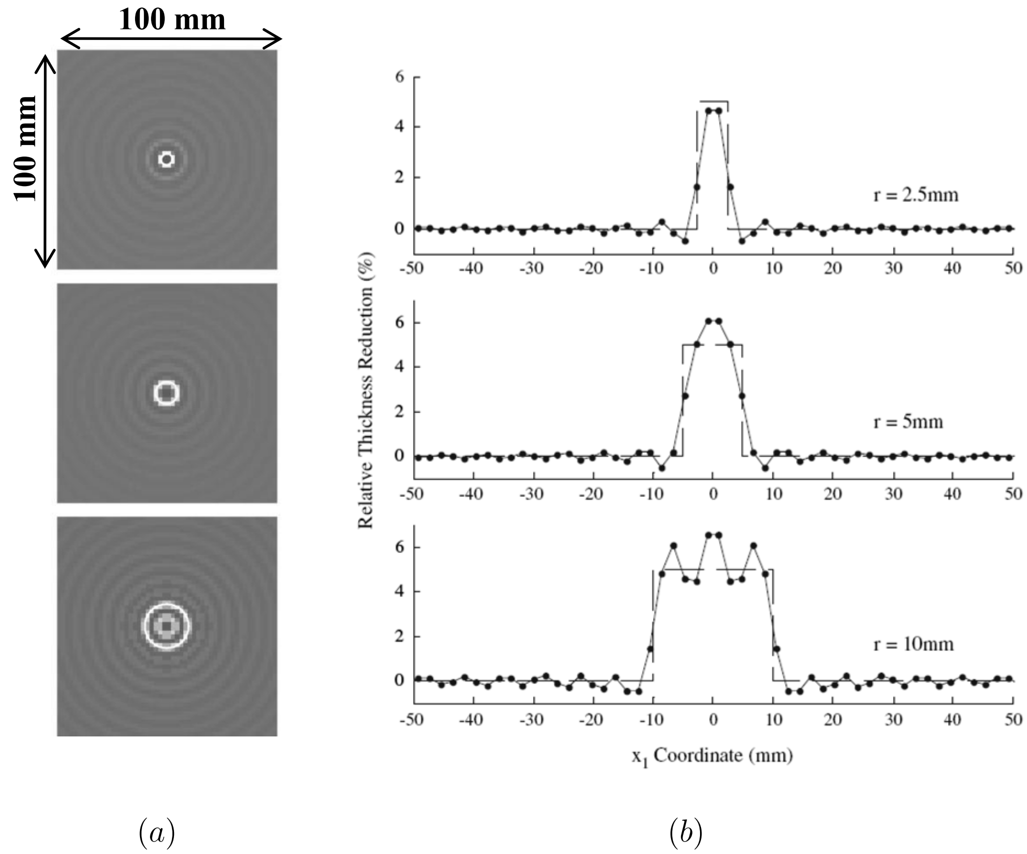

Figure 2.19: *Tomographic reconstructions presented in [38] for three relative thickness changes with three different diameters. (a) thickness map and (b) the corresponding thickness profile. The dashed line in (b) corresponds to the theoretical thickness profile.*

2.2.3 High Order Guided Wave Mode Cutoff for Thickness Gauging

Fundamentally the presence of corrosion is simply a change in the waveguide thickness. The significance of the high order modes cutoff property explained in the first section of this chapter is that if a thickness reduction is present along a propagation path such that the frequency thickness product was shifted below the cutoff frequency thickness product of a given mode no energy of that mode would propagate through the reduced thickness region. The energy would be partially reflected and converted into lower order modes. Therefore by identifying which modes propagate through a thickness reduction or corrosion patch, it is in principle possible to obtain an estimation of the minimum remaining thickness in the propagation path.

This idea has been investigated in the past [39–42]. In all these studies the A_1 mode was excited at a frequency thickness product slightly above its frequency thickness product cutoff on one side a thickness reduction and depending whether this mode was detected on the other side of the thickness or not they were able to evaluate whether thickness was smaller or larger than a given value. This value of the thickness corresponding to the thickness at the frequency thickness product cutoff of A_1. This technique is investigated in chapter 4.

2.3 Summary

Bulk waves can travel in two ways, as a shear wave and as a longitudinal wave and the two wave types are uncoupled in an infinite medium. In a finite medium the bulk waves interact with the boundaries of the medium to generate guided waves. A brief overview of two possible solutions was presented: the SH guided wave family and the Lamb guided wave family. Except for the SH_0 mode, all the guided wave modes are dispersive i.e. the phase velocity varies with the frequency thickness product. This is an important properties of the guided waves that can be used in thickness measurement. Except for the three fundamental modes (A_0, S_0 and SH_0), all the guided wave modes can only propagate above a specific frequency thickness product cutoff. This property of the high order modes can also be used for thickness measurement.

The literature review presented three different techniques for thickness evaluation. Ray theory can be implemented in multiple ways that can be divided into two families i.e. the convolution backprojection algorithm and the iterative algorithms. The iterative algorithms have the advantage that they can be implemented with various scanning geometries. It is, for example, easy to use a crosshole scanning geometry on a pipe. The results obtained in a number of studies with various ray tomography algorithms and scanning geometries demonstrated that, to some extent, it is possible to get an approximation of the shape of the defect. Ray tomography is investigated in the context of guided wave time-of-flight tomography in chapter 3.

However Malyarenko and Hinders [30] recognised that diffraction was a major issue to the successful implementation of low frequency guide wave ray tomography for thickness mapping. They attempted to take the diffraction effect into account with a bent ray iterative algorithm. The results they obtained were a slight improvement from their ray tomography reconstructions. Rohde et al [38] used a more complex algorithms that takes the scattering from inhomogeneities into account and obtain very accurate results for the thickness reconstruction. Diffraction tomography is investigated in the context of thickness reconstruction with guided waves in chapter 5.

The high order mode cutoff property has also been studied in the past to obtain an approximation of the remaining thickness between a source and a sensor. The significance of the high order modes cutoff property explained in the first section of this chapter is that if a thickness reduction is present along a propagation path such that the frequency thickness product was shifted below the cutoff frequency thickness product of a given mode no energy of that mode would propagate through the reduced thickness region. The idea is that if a high order mode is excited close to its cutoff frequency thickness product and it is possible to identify whether this mode is detected or not by a sensor, it is then possible to evaluate whether the thickness is smaller or larger than the thickness required at the cutoff frequency thickness product of that mode. This technique is examined in chapter 4.

Chapter 3

Guided Wave Time-Of-Flight Tomography

3.1 Introduction

Low frequency Lamb wave tomography has been used in a range of applications for the detection of defects and is potentially attractive to evaluate the remnant wall thickness in corroded structures. If the frequency is limited to below the cutoff of the high order modes, only the three fundamental guided wave modes can propagate and thus the signal processing and time-of-flight measurement is greatly simplified. Guided waves have traditionally been used at non-dispersive frequencies in order to simplify the signal processing. For thickness reconstruction using guided wave time-of-flight tomography the velocity must vary with the thickness. Consequently dispersion of the chosen guided wave mode is required.

Straight ray time-of-flight tomography algorithms assume that the ray theory is valid and this may not be the case in the low frequency regime. For the ray theory to be valid the size of the defect to image must be larger than the wavelength and larger than the width of the first Fresnel zone. When either of these conditions is not met the scattering from defects interferes with the direct ray.

The aim of this chapter is to investigate the severity of the errors introduced by breaking the assumption of the ray theory. The results presented in this chapter were published in P1, P2 and P3 in the list of publications. In the first section two likely points of operation, guided wave mode and frequency, in the low frequency range are discussed. Three criteria were established to find the optimal points of operation, velocity sensitivity to thickness change, the excitability and detectability and the leakage attenuation.

The second section demonstrates, via finite element (FE) simulations, that the ray theory criteria cannot be relaxed for thickness reconstruction with defects of the size of interest in this study using guided wave time-of-flight tomography. Finally the last section verifies the conclusions obtained in simulations experimentally.

3.2 Likely Points of Operation

The results of any of the straight ray tomography algorithms largely depends on the accuracy of the projection data. Consequently three selection criteria were established in order to find the most suitable point of operation for guided wave time-of-flight tomography:

- **Velocity sensitivity to thickness change**

  The velocity sensitivity to a thickness change is defined as the amount of variation in the velocity of the chosen guided wave mode due to a given change in the thickness. Both the phase and group velocities vary if the thickness changes. The variations of the group velocity can be evaluated with the time-of-flight of the wave packet. On the other hand the variations of the phase velocity are more subtle to measure. Intanes et al. [43] have presented a method that uses the point of constant group velocity to evaluate the variations of phase velocity due to corrosion and erosion in pipes. In any case the sensitivity is directly related to the amount of dispersion at the chosen point of operation.

- **Excitability and detectability**

The excitability of a particular mode is defined in [44] as the ratio of displacement of that mode to applied force when both quantities are measured at the same location and direction in the cross section. A large excitability and detectability increases the ratio of the desired mode to the other excited/detected modes.

- **Attenuation due to fluid loading**

  This project is interested in evaluating the severity of corrosion in pipes that may contain fluid. In this specific application, it is important to take the leakage attenuation into account because fluid loading can severely attenuate the chosen mode. The attenuation due to fluid loading or leakage attenuation is defined in this study as the attenuation due to a half space of water on one side of a plate.

In this chapter the quest for the optimum point of operation is carried out for a 10mm steel plate. However it is possible to use a similar point of operation in other materials at a slightly different frequency-thickness product, such that results presented here would apply.

3.2.1 Velocity Sensitivity to Thickness Change

The sensitivity to a thickness change is probably the most important criterion. In fact time-of-flight tomography relies only on the variations of velocity through the defect to reconstruct the thickness. Hence the dispersion of the chosen mode must be significant. With the aim of simplifying the practical implementation only the fundamental Lamb wave modes are considered in this investigation. Figure 3.1 presents the group velocity dispersion curves in a steel plate. The thick parts of the curves represent the area where the sensitivity to thickness change is suitable for time-of-flight tomography. To make sure the high order modes do not contaminate the signals, the frequency of the point of operation needs to be limited to about 2.0 MHz.mm. Above this frequency the velocities of A_0, S_0 and A_1 are close and the modes overlap for short propagation distances.

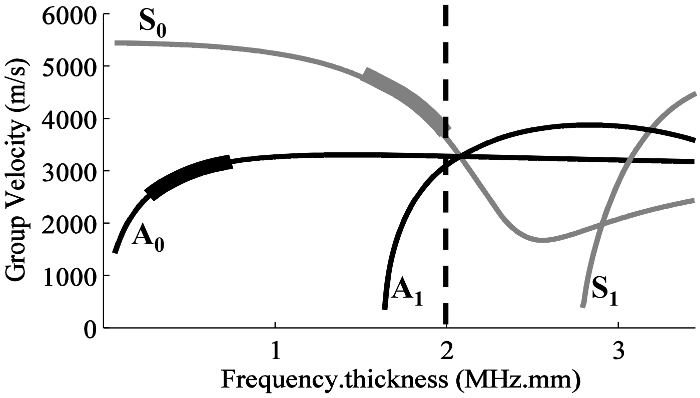

Figure 3.1: *Group velocity dispersion curves in a steel plate. The vertical dashed line at 2 MHz.mm corresponds to the highest frequency thickness product to avoid contamination from the high order modes.*

A_0 is significantly dispersive in the range between 0.15 and 0.75 MHz.mm. Above this range there is virtually no dispersion of the group velocity. A major drawback of A_0 in this frequency range is that the faster S_0 always arrives before A_0. If S_0 and A_0 are excited with the same amplitude, the fact that A_0 will arrive after S_0 will make the time-of-flight measurement much harder. Moreover the two modes might overlap if the propagation distances are short.

In terms of dispersion, S_0 at a frequency between 1.25 and 2.0 MHz.mm is a much better candidate. Moreover in the frequency range of interest it is always faster than any other mode. However, as the frequency increases the velocity difference between S_0, A_0 and A_1 decreases. Consequently, if the three modes are excited with the same amplitude at a frequency close to 2.0 MHz.mm it would take a longer distance for the 3 wave packets to separate than at a lower frequency. In practice, though, the modes are not going to be excited with the same amplitude. The ratios between the amplitudes of the excited modes are given by the excitability.

3.2.2 Excitability and Detectability

The mode excitability and detectability is a very important criterion to consider for practical implementation. The excitability corresponds to the ratio between the

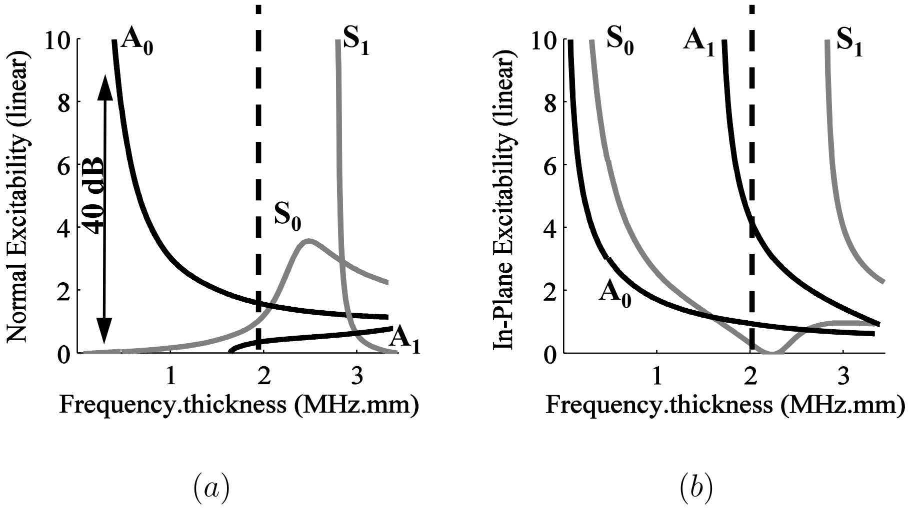

Figure 3.2: *(a) Normal and (b) In-plane excitability for the first four Lamb wave modes.*

surface displacement in a given direction and the surface excitation force in the same direction and at the same location. Figure 3.2 presents (a) the normal excitability and (b) the in-plane excitability in a 10 mm steel plate.

At low frequency a normal force excites A_0 with an amplitude 40 dB above S_0. Hence, in the frequency range of interest, this ratio of excitability provides a virtually pure A_0 mode. On the other hand in the frequency range of interest of S_0, an in-plane or normal force excites high amplitude A_0 and A_1. Consequently if the chosen mode of operation is S_0 the accuracy of the time-of-flight measurement would rely on the group velocity difference between S_0 and the other modes. Long propagation distances would make sure the S_0 wave packet is pure and not contaminated by other modes.

The effect of excitability on the signal is simulated in a 400 mm long 10 mm thick steel plate. Figure 3.3 presents (a) a schematic of the 2D plane strain FE model, (b) the normal displacement at the end of the plate when the excitation is a 5 cycle Hanning windowed toneburst normal force centered at 50 kHz and (c) the in-plane displacement at the end of the plate when the excitation is a 5 cycle Hanning windowed toneburst in-plane force centered at 150 kHz. An absorbing boundary was inserted at both ends of the plate to ensure there is no reflection.

The signal recorded with the normal force at 50 kHz is a virtually pure A_0 mode, as

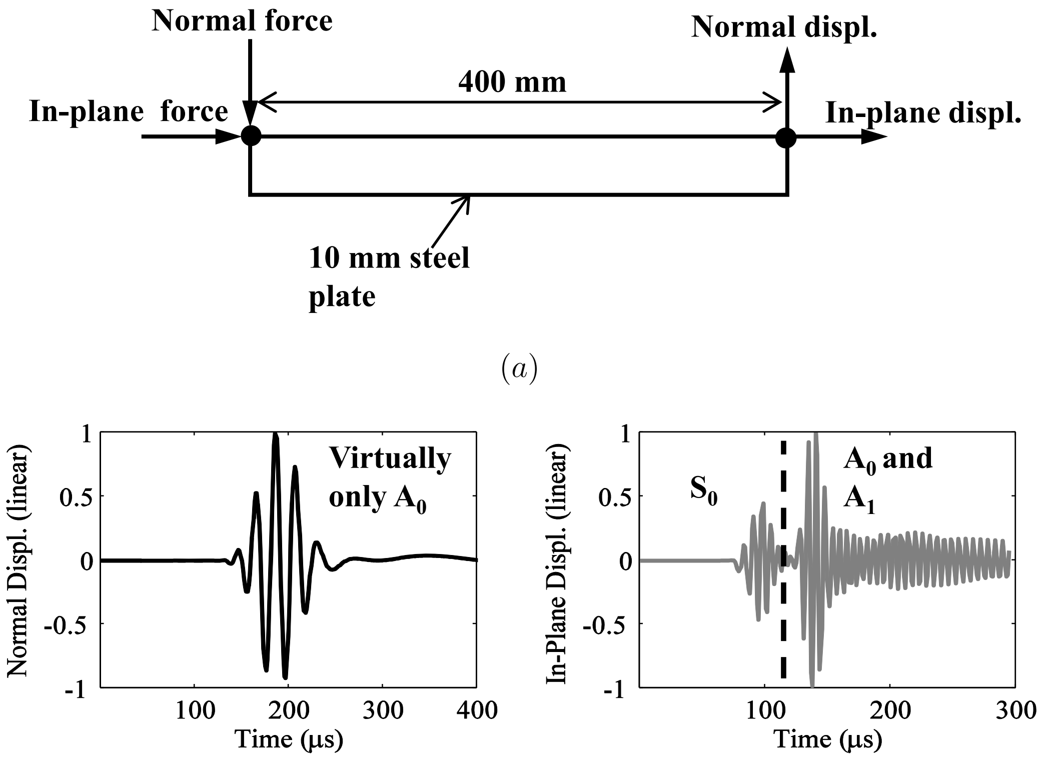

(a)

(b) *(c)*

Figure 3.3: *(a) Schematic of the FE model of a 10 mm steel plate, (b) normal displacement at the end of the plate for a normal force 5 cycle Hanning windowed toneburst centered at 50 kHz and (c) in-plane displacement at the end of the plate for an in-plane force 5 cycle Hanning windowed toneburst centered at 150 kHz.*

was predicted from the excitability curve. The S_0 component theoretically arrives slightly before the A_0 wave packet but the normal displacement component is 40 dB below A_0. Moreover S_0 is also hardly detected because the source and sensor are exactly the same. If A_0 and S_0 were propagating with the same amplitude the detected normal displacement of A_0 would be 40 dB above S_0.

The signal recorded with the in-plane force at 150 kHz is much more complex. All three possible modes are detected by the in-plane sensor. S_0 is, as expected, the first wave packet to arrive closely followed by A_0 and A_1. With a shorter propagation distance all three modes would have overlapped.

The two signals presented on figure 3.3 correspond to the case where the plate has no defect. If a defect is introduced mode conversion will modify the signals because the converted modes will superpose with the incoming modes. Figure 3.4 presents (a) a schematic of the 2D plane strain FE model of a 10 mm steel plate with a defect, (b) the normal displacement at the end of the plate when the excitation is a 5 cycle Hanning windowed toneburst normal force centered at 50 kHz and (c) the in-plane displacement at the end of the plate when the excitation is a 5 cycle Hanning windowed toneburst in-plane force centered at 150 kHz. The defect on the plate is a 20% surface thinning with square edges. The amplitude of the converted modes is related to the sharpness of the edges of the defect in comparison with the wavelength of the incoming mode. Square edges are thus the worst possible case in terms of mode conversion.

On figure 3.4 (b), the normal displacement on the top surface of the plate is virtually unaffected by the mode conversion. At this frequency the incoming A_0 can only convert to S_0 and fortunately the normal surface displacement is nearly insensitive to S_0. It also appears that double mode conversion is not polluting the incoming A_0. The mode converted signal from the incoming A_0 to S_0 back to A_0 would have arrived slightly before the incoming A_0. Each time the modes are converting, the amplitude of the converted mode represents a fraction of the incoming mode. Hence the double mode conversion has a negligible amplitude.

The signal on figure 3.4 (c) is much more complex. S_0 is the first mode to arrive but it is overlapping with 4 different converted modes, S_0 to A_0, S_0 to A_1, A_0 to S_0 and A_1 to S_0. At this frequency the detectability makes the amplitude of the converted modes significant. The time separation between the incoming S_0 and the converted modes can be increased with longer propagation distances. In order to separate the incoming S_0 from the S_0 to A_0 and S_0 to A_1 the propagation distance before the defect needs to be increased and to separate it from the A_0 to S_0 and A_1 to S_0 the propagation distance after the defect must be increased. It was found in the Disperse software [19] that at 150 kHz a 5 cycle Hanning windowed toneburst S_0 would be free from overlapping modes after approximately 300 mm. Hence in order to avoid any mode overlapping a distance of approximately 300 mm is required before and after the inspection area.

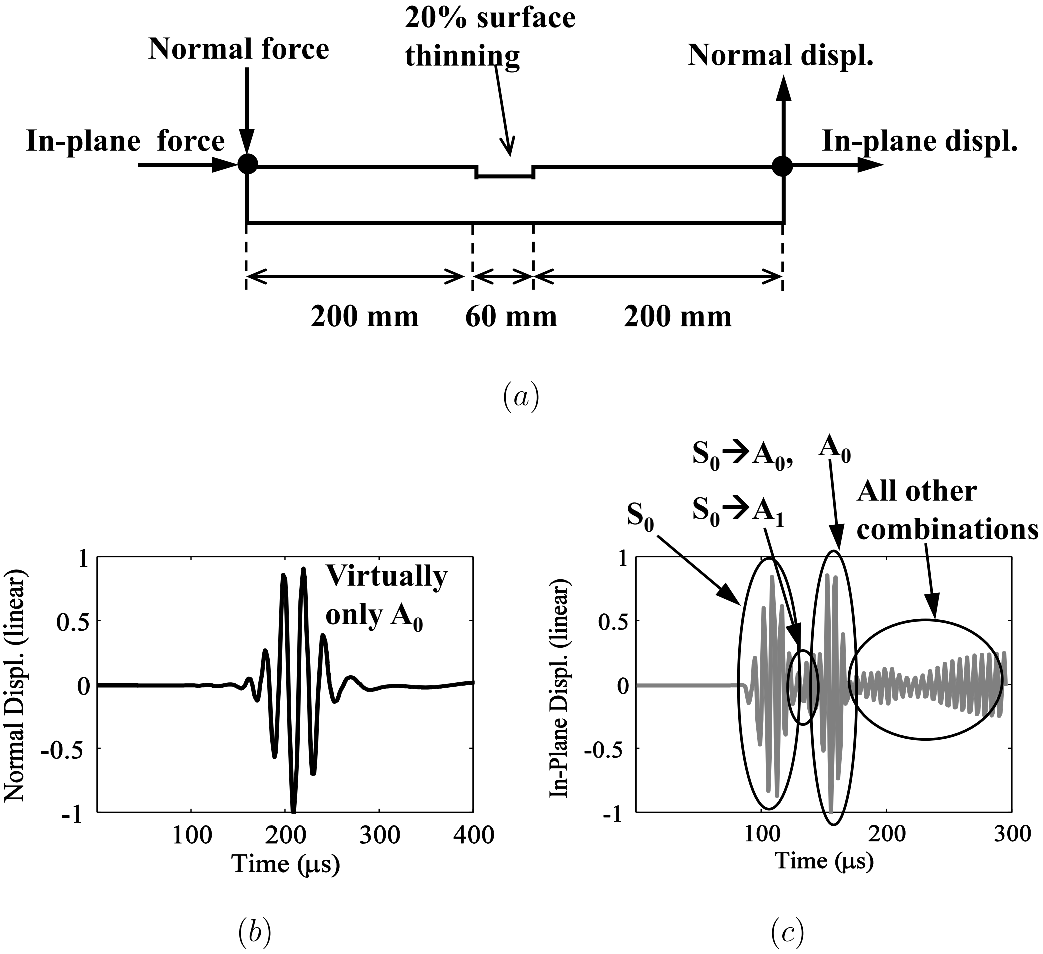

Figure 3.4: *(a) Schematic of the FE model of a 10 mm steel plate with a defect, (b) normal displacement at the end of the plate, normal force 5 cycle Hanning windowed toneburst centered at 50 kHz and (c) in-plane displacement at the end of the plate, in-plane force 5 cycle Hanning windowed toneburst centered at 150 kHz.*

3.2.3 Attenuation Due to Fluid Loading

Fluid loading could have a disastrous effect on the propagation of guided waves over long distances and can severely compromise long range inspection if the point of operation is not carefully selected. Figure 3.5 presents the attenuation of the fundamental Lamb wave modes in a 10 mm steel plate due to a semi-infinite layer of water coupled to the top surface of the plate.

The attenuation due to fluid loading is very high at low frequency for A_0. At 50 kHz the attenuation of A_0 is 37 dB/m. Hence from the perspective of long range

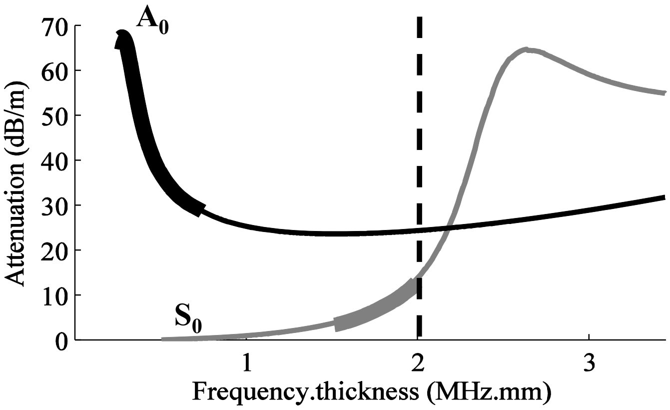

Figure 3.5: *Attenuation of the fundamental Lamb wave modes in a 10 mm steel plate with a semi-infinite water layer coupled to the top surface of the plate.*

inspection, A_0 would be difficult to use. Even with the 40 dB difference in excitability and detectability, after propagation of 1 m, A_0 and S_0 would have approximately the same amplitude. On the other hand S_0 has an attenuation below 11 dB/m in its frequency range of interest.

The similarities between the normal excitability curve of figure 3.2 (a) and the leakage attenuation curve of A_0 on figure 3.5 are obvious. The leakage attenuation is the result of the coupling between the normal surface displacement of the plate and the bulk waves in the semi-infinite layer of water. Correspondingly the normal excitability is the coupling between a normal force and the normal surface displacement. Consequently the modes with a large component of normal surface displacement have a high normal excitability but also a high leakage attenuation, and on the other hand the modes with a small component of normal surface displacement have low normal excitability and low leakage attenuation.

If fluid loading is taken into account S_0 at a frequency around 1.75 MHz.mm, where the velocity difference between S_0 and the other modes is still high, is the best choice provided the propagation distances before and after the defect are long enough for the wave packets to separate. However when there is no fluid loading, the 40 dB difference in normal excitability and detectability shifts the choice to A_0 at a frequency around 0.5 MHz.mm.

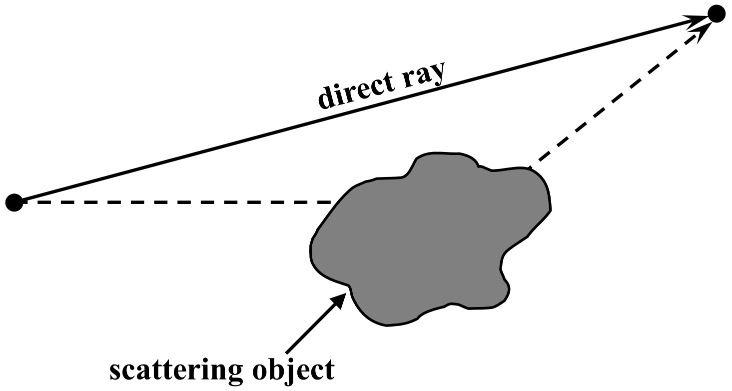

Figure 3.6: *Schematic of the scattering from an object.*

3.3 Ray Theory

Menke and Abbott [45] and later Červený [46] have demonstrated that the ray theory is valid when the characteristic size of an object d is larger than the wavelength λ and the width L_F of the first Fresnel zone (hereafter called the Fresnel zone)

$$d \gg \lambda \quad \text{and} \quad d \gg L_F \tag{3.1}$$

When either of these conditions is not met the scattering from inhomogeneities modifies the received wave packet. Figure 3.6 presents a schematic of the scattering from an object close to the direct ray.

If the scattering object is within the Fresnel zone of the direct ray, the direct and scattered rays superpose at the receiver with different phase and thus the arrival time and amplitude of the time trace is modified. The Fresnel zone consists of all the geometrical points between a source and a sensor such that the difference between the length of the path from the source to the receiver via the scatterer and the length of the direct ray is less than half a wavelength. According to Červený [46], at the mid point between the source and the receiver the width of the Fresnel zone is approximately

$$L_F(L/2) = \sqrt{\lambda L} \tag{3.2}$$

where L is the distance between the source and the receiver. This corresponds to the Fresnel zone in the case of a one wavelength long signal. For a signal with a finite length the zone of interference affecting the accuracy of the time-of-flight measurement is larger. In this case the length of the signal and the method used for the measurement must be taken into account in the computation of the zone of interference. Hence approximating the zone of interference with the Fresnel zone is an underestimation in the case of a finite length signal.

For the problem of interest (see chapter 1), imaging a 60 mm diameter thickness reduction with a propagation distance of approximately 1 m, the ray theory is not valid at the points of operation quoted in the previous section. The rest of the chapter studies the possibility of relaxing the ray theory criteria for guided wave time-of-flight tomography.

3.4 Evaluation of the Time-of-Flight

In the present study the accuracy of the time-of-flight measurement is critical. Ernst and Herman [47] proposed the generalised travel time method for the evaluation of the phase velocity at the frequencies contained in the input signal in seismic wave propagation. The main limitation of this method is that each mode must be separated in time at the receiver. In guided wave propagation mode conversion at the defects would normally prevent this condition from being satisfied. More recently Hou et al [48] have compared various group time-of-flight measurement techniques for guided waves and proposed a multi-mode travel time measurement technique called the dynamic wavelet fingerprint.

The method proposed in this chapter is the cross-correlation of the Hilbert transform of the signal recorded by a receiver and the Hilbert transform of a simulated propagation of the input signal over the distance between the source and the receiver. The simulated propagation takes the dispersion properties of the plate into account. In order to extract the time-of-flight accurately the Hilbert transform of the mode of interest must be free from overlapping modes at least up to its maximum value. Consequently the length of the plate was chosen such that even if there is mode conversion at a defect in the area of inspection, the length of the plate after the

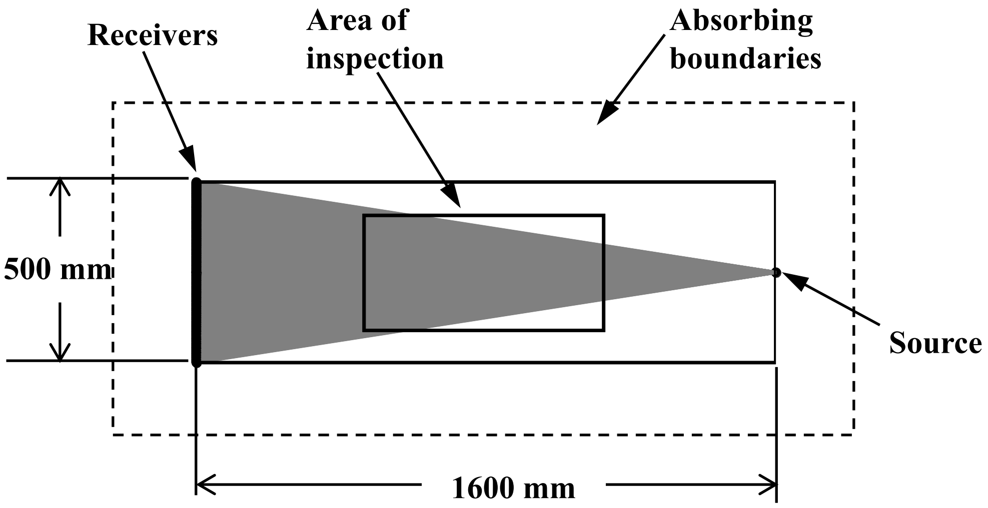

Figure 3.7: *Schematic of the FE model.*

defect is long enough to ensure that the mode of interest separates in time from the other propagating modes. The method proposed in this chapter was compared with the dynamic wavelet fingerprint proposed by Hou et al [48] and both methods showed consistent results when the mode of interest is not overlapping with other modes up to the maximum of amplitude of the Hilbert envelope of the signal. The cross-correlation of the Hilbert transforms was used in this chapter because of its simpler implementation in comparison with the dynamic wavelet fingerprint.

3.5 Finite Element Simulations

3.5.1 Finite Element Model

In order to study the severity of the errors in the evaluation of the thickness due to the invalidity of the ray theory, a FE model was designed in ABAQUS. A schematic of the ABAQUS model is presented in figure 3.7; it was designed to calculate only one projection. The results presented in this chapter are also valid for large diameter pipes as the curvature has an insignificant effect on the propagation of guided waves in that case [8].

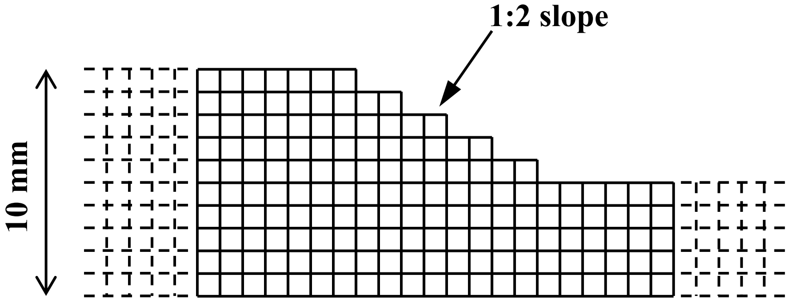

Figure 3.8: *Schematic of a stepped defect.*

Absorbing boundaries [49, 50] were introduced on all sides of the plate to avoid reflections from its edges. The steel ($E = 216.9$ GPa, $\nu = 0.29$ and $\rho = 7932$ kg/m^3) plate was 1600 mm long, 500 mm wide and 10 mm thick. Linear cubic-shaped 3D brick elements were used in the model and the length of all sides was 1 mm. The time step of the simulations was chosen in accordance with the element size. A point source was located on the right-hand side and on the axis of symmetry of the plate. In order to obtain a full projection in one simulation, a linear array of receivers with a 5 mm spacing was placed on the left-hand side of the plate.

Actual corrosion patches are not like flat-bottomed holes so stepped boundaries are a better representation. Hence in order to model realistic corrosion patches the 10 elements through the thickness were used to model a stepped defect. Figure 3.8 presents a schematic of a 50% deep stepped defect; a 10% defect was modelled in one step and a 50% defect was modelled in five steps.

3.5.2 Finite Element Simulations with A_0 at 50 kHz

In this case the excitation on the plate was a force normal to the plate so as to take advantage of the normal excitability of the mode, and the input signal was a five cycle toneburst. The linear array of receivers recorded the displacement normal to the plate. A stepped defect with an outer diameter of 60 mm was introduced in the middle of the plate. Figure 3.9 presents a schematic of the plate and the location of the defect. The parameters for this set of simulations are summarised in table 3.1.

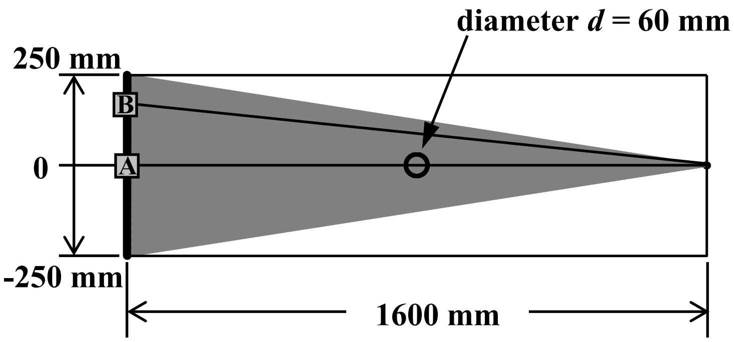

Figure 3.9: *Schematic of the FE model when there is one defect at the mid length centered on the plane of symmetry.*

Table 3.1: Parameters for the FE simulations using A_0.

Mode	A_0
Frequency (kHz)	50
Wavelength (mm)	40
Width of Fresnel zone (mm)	250
Nominal group velocity (m/s)	2947
Defect diameter (mm)	60

The defect diameter corresponded to 1.5 wavelengths and the width of the Fresnel zone corresponded to more than 6 wavelengths. Consequently the characteristic size of the defect d (60 mm) had a size comparable to the wavelength λ but was much smaller than the width of the Fresnel zone. Therefore the conditions of the ray theory are not met but it is interesting to evaluate the severity of the errors introduced. Figure 3.10 presents (a) the group velocity as computed from the FE data across the linear array of receivers for 10%, 20%, 30%, 40% and 50% defects and (b) a comparison between the ray theory projection and the FE projection for a 50% defect. According to the ray theory only the rays that are passing through the defect should be affected by the defect. These rays correspond to those contained within the black vertical lines in figure 3.10.

As shown in figure 3.10 (b), the ray theory projection and the FE simulated projection are rather different. If the simulated projection was used in a tomographic

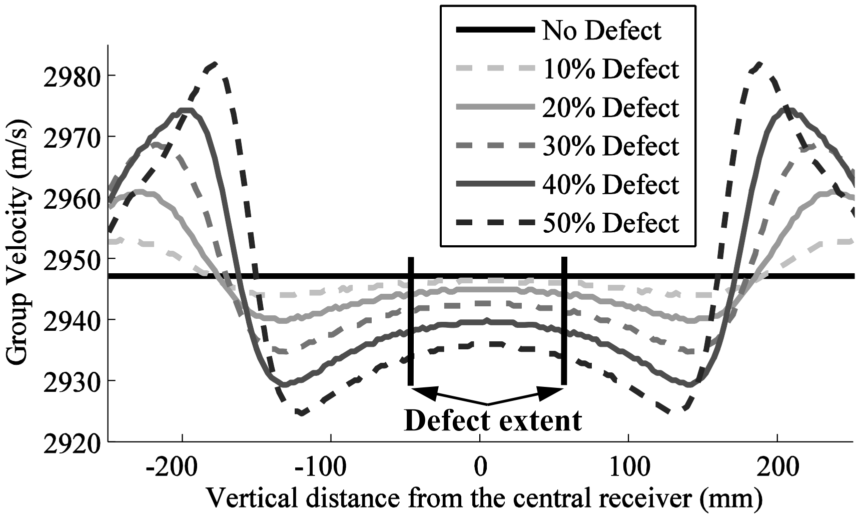

(*a*)

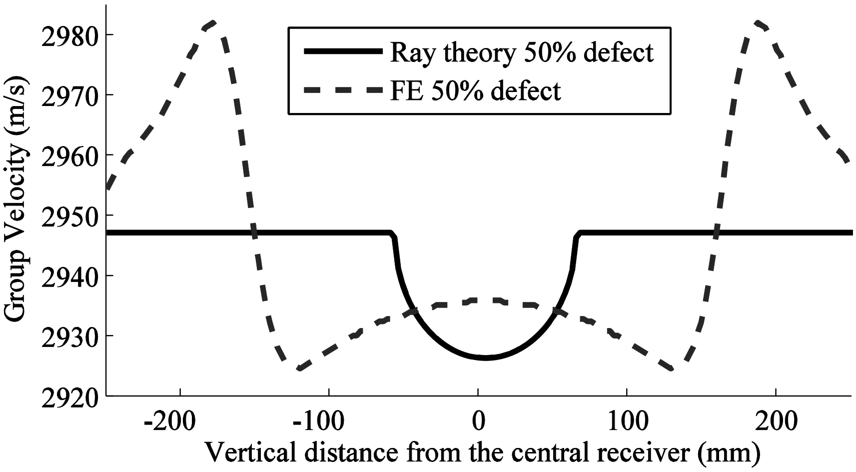

(*b*)

Figure 3.10: *(a) A_0 Group velocity centered at 50 kHz evaluated at all the receivers for the cases where there is no defect, a 10% defect, a 20% defect, a 30% defect, a 40% defect and a 50% defect. (b) Comparison between the group velocity from the ray theory and the FE group velocity for a 50% defect.*

reconstruction the diameter of the surface thinning would appear to be about twice the actual extent; moreover instead of having the maximum depth at the centre of the defect it would be at the edge of the reconstructed defect. Also, beyond the edge of the reconstructed defect, there would be an area where the thickness appears to have increased. These results show that the invalidity of the ray theory created a significant error in the projection.

(*a*)

(*b*)

Figure 3.11: *Displacement field of the plate when (a) there is no defect and (b) when there is a 30% defect.*

Within the Fresnel zone the sensitivity to the defect is not constant [51] but varies with the distance from the geometrical ray. Consequently the arrival time and amplitude of the signals at the receivers vary according to the location of the defect within the Fresnel zone. This is due to the destructive and constructive interference between the incident and scattered fields at the receiver. Figure 3.11 presents a snapshot of the predicted displacement field in the plate after interaction with the defect.

In the no defect case the amplitude of the displacement field was approximately uniform across the width of the plate; however with the 30% defect the amplitude varies greatly across the width of the plate. The interference between the incident and scattered fields within the Fresnel zone is also what caused the apparent velocity

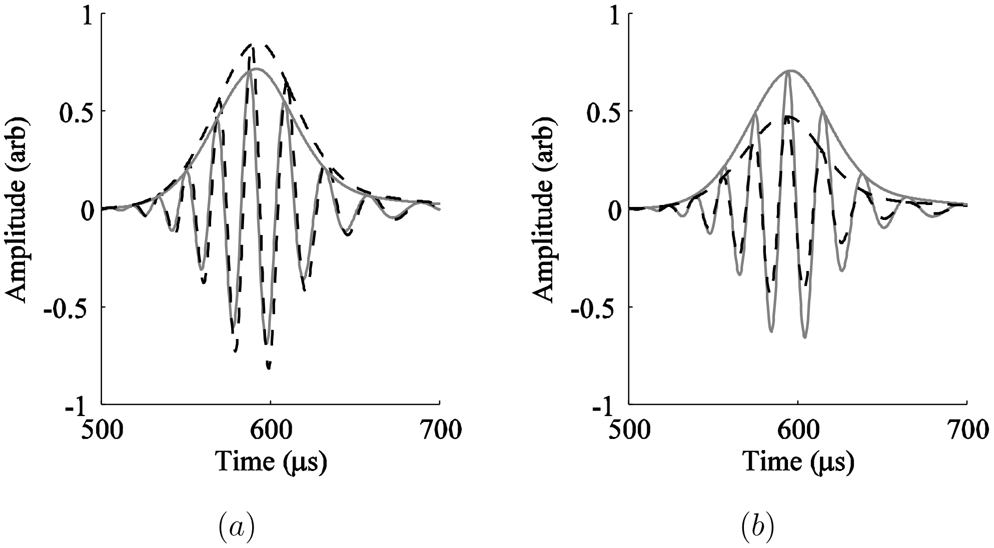

Figure 3.12: *Time traces simulated (a) at A (through the defect geometrical ray) in figure 3.9 and (b) at B (defect free geometrical ray) in figure 3.9. The grey line is without defect and the black dashed line is with a 30% defect.*

variation across the receiver array of figure 3.10. Figure 3.12 (a) and (b) show respectively the time traces simulated at the receiver locations A and B in figure 3.9. With the defect the signal recorded by the receiver at location A had a larger amplitude and was slightly delayed whereas at location B the amplitude was lower and the wave packet was slightly advanced.

In order for the ray theory to be valid the defect needs to be larger than the width of the Fresnel zone. The only way it is possible to achieve that with a 60 mm defect is to reduce the width of the Fresnel zone by reducing the distance between the source and the receiver in equation 3.2. In order to respect the Fresnel zone criterion the propagation distance would need to be reduced to 90 mm. Such a propagation distance is too short to be of practical interest.

In theory [52], if there is only one defect in the Fresnel zone, it is possible to calculate the sensitivity to velocity change as a function of the distance from the geometrical ray. Hence if there is only one defect within the Fresnel zone it would be possible to reconstruct the thickness accurately. However in practice we are interested in mapping the thickness over a region that might contain multiple defects and not a

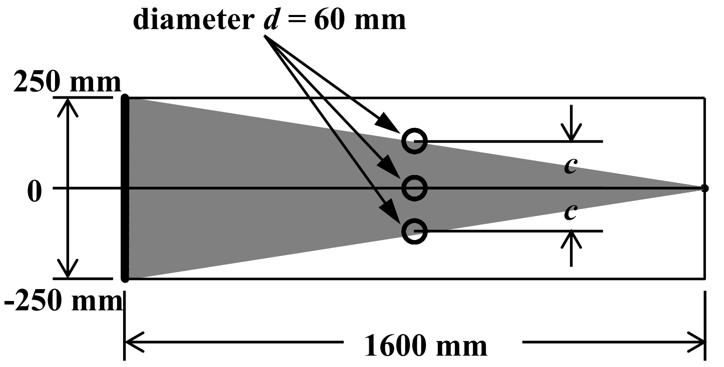

(*a*)

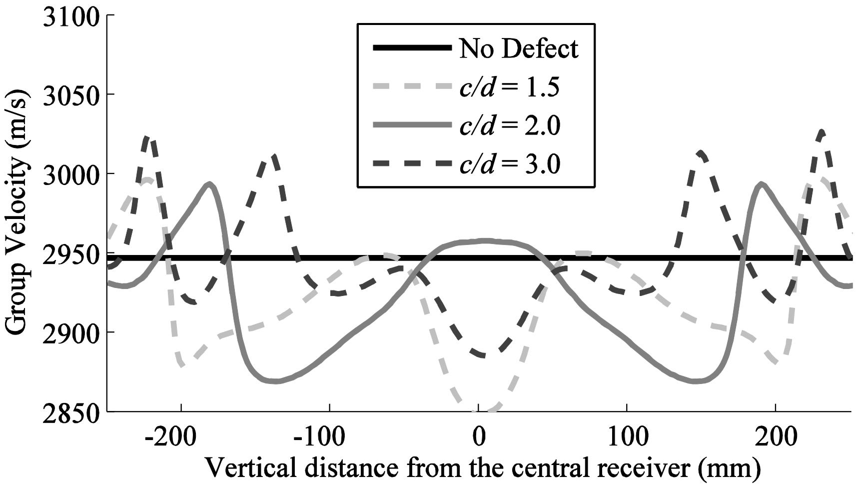

(*b*)

Figure 3.13: *(a) Schematic of the FE model when there are three defects at the mid length of the plate. The spacing between the defects is c. (b) Group velocity evaluated at all the receivers for the cases where there is no defect, three 50% defects with defect spacing over defect diameter (c/d) ratios of 1.5, 2.0 and 3.0.*

single discrete defect. Hence it is impossible to ensure that the Fresnel zone contains only one defect. Figure 3.13 (a) presents a schematic of the FE model when there are 3 defects. Three ratios of defect spacing to defect diameter (c/d) were investigated: 1.5, 2.0 and 3.0 which correspond to a separation distance of 2.3, 3.1 and 4.6 λ at the frequency of interest. In all the cases investigated the defects were 50% deep. Figure 3.13 (b) presents the simulated group velocity as computed from the FE data across the receiving array for the three values of c/d. The parameters for this set of simulations are presented in table 3.1.

From the three projections shown in figure 3.13 (b) it is clear that it is not possible to identify reliably the number or extent of the defects. These projections cannot be used for tomographic reconstruction because the resulting thickness map would be erroneous. Despite having good dispersion properties A_0 at 0.5 MHz.mm cannot be used for straight-ray tomography because it does not fulfill the conditions of validity of the ray theory. The next section will demonstrate that the same conclusion applies to another likely point of operation, S_0 at 1.75 MHz.mm.

3.5.3 Finite Element Simulations with S_0 at 175 kHz

In this case the excitation on the plate was a force in the plane of the plate in the direction of propagation of the wave and the input signal was a fifteen cycle toneburst. In this case a longer toneburst was required in order to reduce the frequency content of the signal and thus avoid the frequency regime where S_0 has the same group velocity as A_0 and A_1. A shorter toneburst would make the evaluation of the time-of-flight very difficult because of the mode superposition. The displacement was simulated at the position of the array of receivers shown in figure 3.9 in the plane of the plate in the direction of propagation of the wave. A stepped defect with an outer diameter of 60 mm was introduced in the middle of the plate centered on the axis of symmetry (as shown in figure 3.9). The characteristic size of the defect d (60 mm) was twice the wavelength λ but was again much smaller than the width of the Fresnel zone. The parameters for this set of simulations are summarised in table 3.2.

Figure 3.14 (a) shows the group velocity as computed from the FE data across the linear array of receivers for 10%, 20%, 30%, 40% and 50% defects and figure 3.14 (b) shows a comparison between the ray theory projection and the FE projection for a 50% defect. The black vertical lines in figure 3.14 (a) contains the rays that are theoretically passing through the defect.

The velocity change is not as large as with A_0 because of the dispersion characteristic of S_0 at 1.75 MHz.mm. If this projection was used in a tomographic reconstruction

Table 3.2: Parameters for the FE simulations using S_0.

Mode	S_0
Frequency (kHz)	175
Wavelength (mm)	30
Width of Fresnel zone (mm)	220
Nominal group velocity (m/s)	4376
Defect diameter (mm)	60

the diameter of the surface thinning would appear to be about twice as large as the real extent. As for A_0 the maximum depth of the defect would be at the edge of the reconstructed defect. Beyond the edge of the reconstructed defect there would be an area where the thickness is increased. Therefore again this projection would result in an incorrect thickness map.

Hence the FE simulations indicate that neither A_0 nor S_0 in the low frequency regime can be used for quantitative ray theory tomography. The next section verifies that conclusion experimentally.

3.6 Experimental Validation

In order to reproduce the FE simulations experimentally a 1200 × 1200 × 10 mm aluminium plate was used. Aluminium was chosen instead of steel for ease of handling in the laboratory and because the two materials have very similar dispersion curves so that the wave propagation characteristics are comparable. A schematic of the experimental setup is presented in figure 3.15.

A 10 mm diameter A_0 source [53] was located on the right-hand side of plate and the input signal was a five cycle toneburst centred at 50 kHz. The wavelength λ of A_0 at 50 kHz in a 10 mm aluminium plate is approximately 40 mm and the source diameter is approximately a quarter of the wavelength. The point source model used

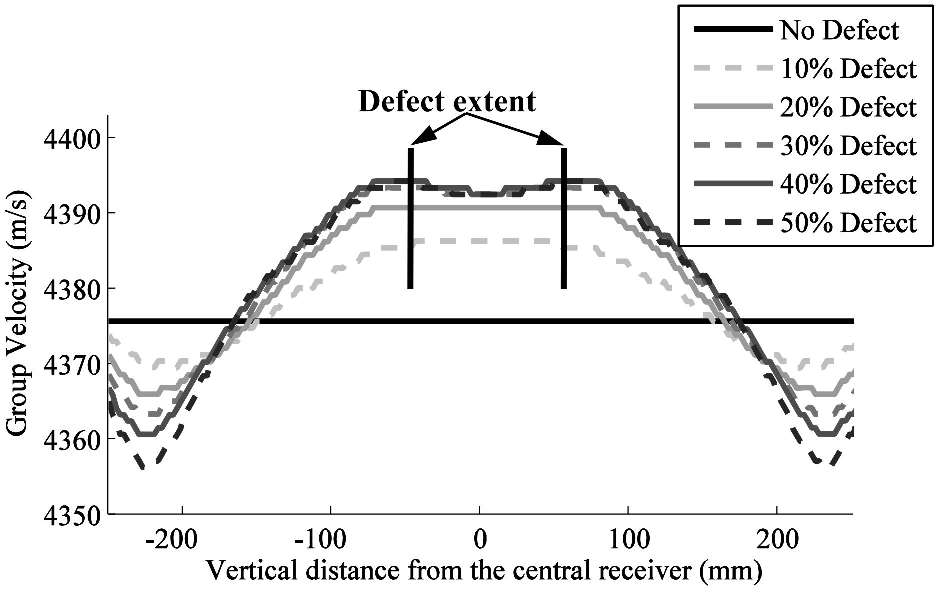

(*a*)

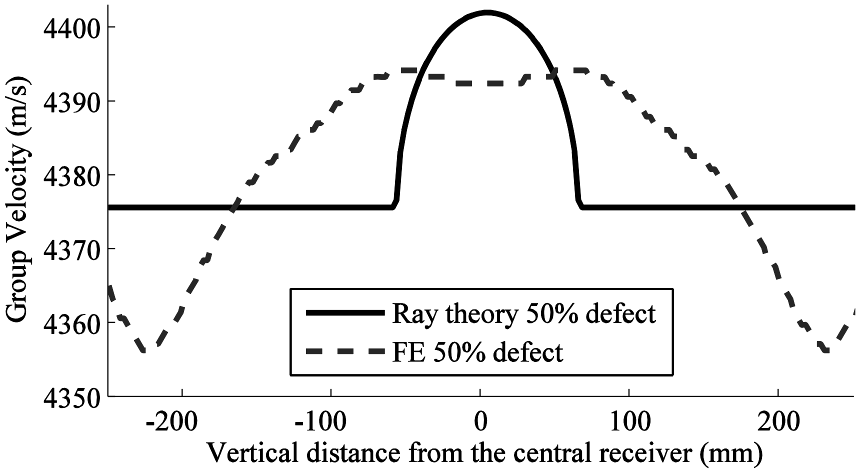

(*b*)

Figure 3.14: *(a) S_0 Group velocity centered at 175 kHz evaluated at all the receivers for the cases where there is no defect, a 10% defect, a 20% defect, a 30% defect, a 40% defect and a 50% defect. (b) Comparison between the group velocity from the ray theory and the FE group velocity for a 50% defect.*

in the FE simulations is therefore a reasonable representation. On the left-hand side a laser Doppler vibrometer Polytec OFV-505 was used to acquire the time traces. They were obtained at the same locations as the linear array of receivers in the FE model in figure 3.9. The profile of the circular defect machined in the plate is shown

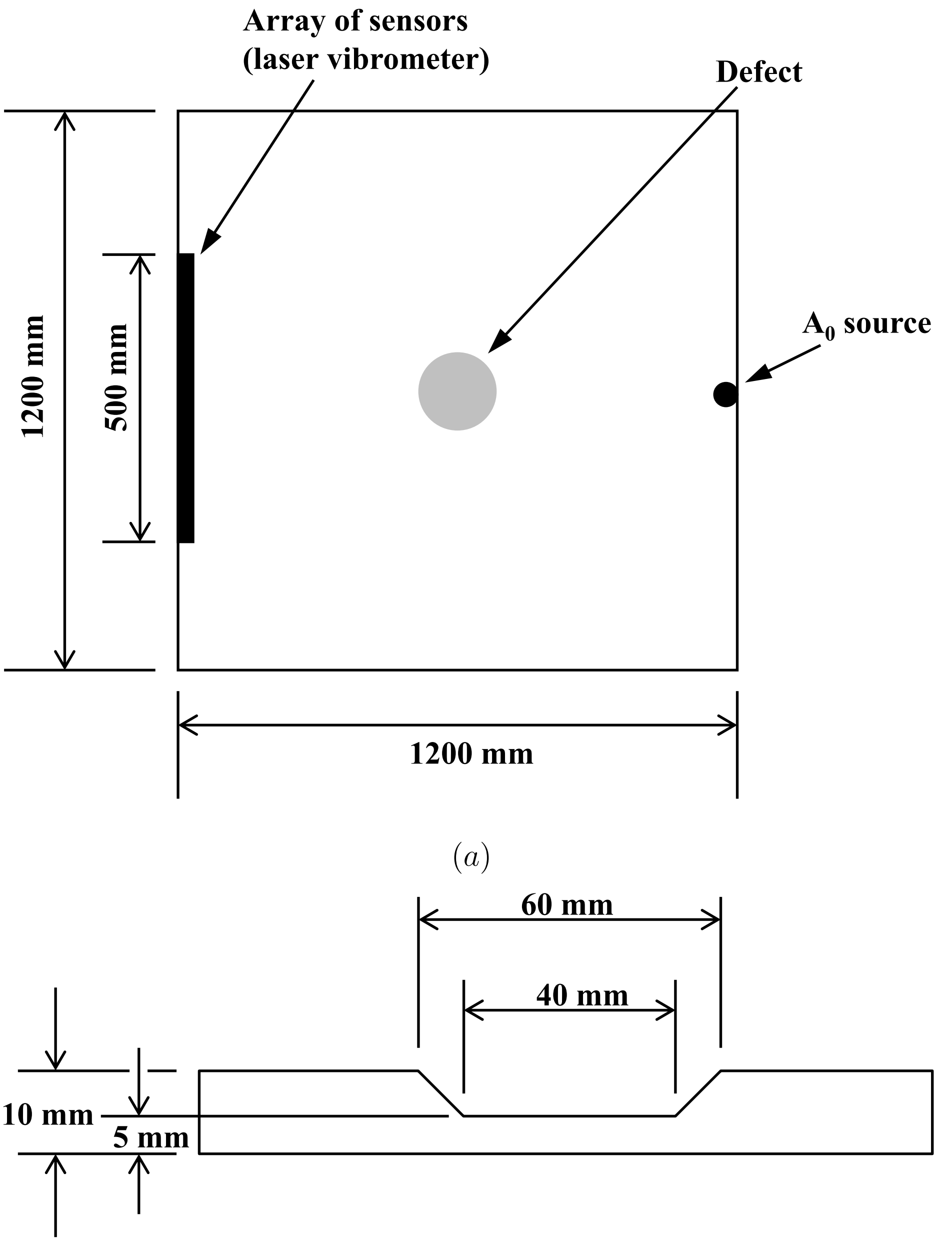

(*a*)

(*b*)

Figure 3.15: *(a) Schematic of the experimental setup and (b) profile of the defect machined in the middle of the plate.*

in figure 3.15 (b). The outer diameter of the defect was 60 mm, which corresponds to the diameter of the defect used in the FE simulations. Figure 3.16 presents a comparison between the FE and experimental velocity projections. The FE curve was obtained from a model of the experimental setup on an aluminium plate and not from the FE results on steel presented in the previous section. The velocity

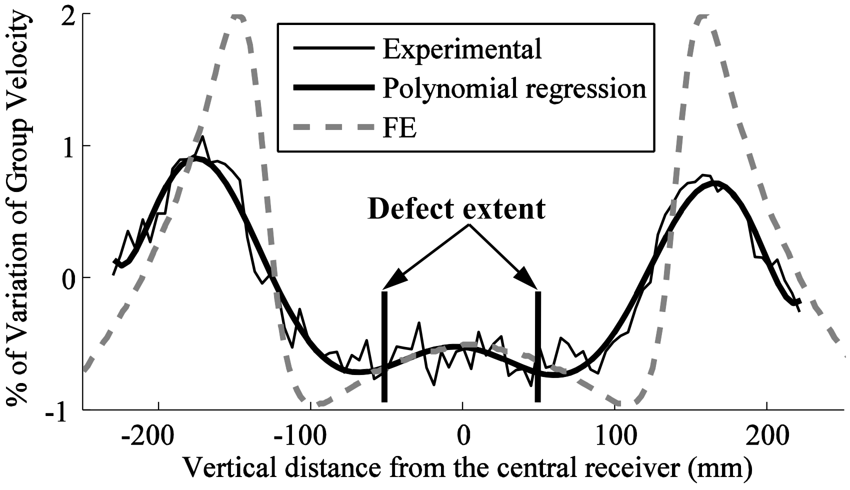

Figure 3.16: *Comparison between FE and experiment of the percentage of variation of the group velocity measured at all the receiver location for a 50% defect.*

projections are plotted as a percentage variation of the nominal group velocity to remove the anisotropy in the propagation velocity of the experimental plate and to make the comparison with FE easier.

Qualitatively the FE and experimental results are similar, both showing an average group velocity reduction extent larger than the size of the defect and having peaks on both sides of the defect. The results at the central rays agree very well but outside this zone the FE prediction overestimate the variations of the average group velocity. The reasons for this are not clear but the agreement is sufficient to validate the conclusion that the method is not suitable for quantitative determination of the depth of corrosion patches.

3.7 Summary

Two points of operation, frequency and guided wave mode, were identified using three criteria: the velocity sensitivity to thickness change, the mode excitability and detectability and the attenuation due to fluid loading. If fluid loading is taken into account S_0 at a frequency around 1.75 MHz-mm, where the velocity difference between S_0 and the other modes is still high, is the best choice provided the propagation distances before and after the defect are long enough for the wave packets to separate. However when there is no fluid loading, the 40 dB difference in normal excitability and detectability shifts the choice to A_0 at a frequency around 0.5 MHz-mm.

It has been shown, with FE simulations and experiments, that low frequency guided waves cannot be used for time-of-flight straight-ray quantitative tomography to evaluate the maximum depth of defects of the diameter of interest in practice due to the invalidity of the ray theory. When the ray theory is violated the incident and scattered signals interfere which changes the received wave packet and thus makes the time-of-flight calculations inaccurate.

If the propagation distance is reduced, the ray theory becomes valid in the low frequency regime, but the required reduction is too large to be of practical use. The characteristic size of the defect can also be increased to satisfy the ray theory but again this is not of interest in practical applications.

As the low frequency regime cannot be used for quantitative tomographic reconstruction the obvious solution is to increase the frequency up to where the ray theory is valid. The disadvantage of increasing the frequency is that the scattering of the wave from generally corroded surfaces becomes larger and it is thus harder to achieve the propagation distance required for inspection at pipe supports. This possibility is investigated in chapter 4. However the low frequency regime can be used with the more complex diffraction tomography algorithms. This possibility is examined in chapter 5

Chapter 4

Guided Wave Mode Cutoff for Thickness Gauging

4.1 Introduction

Chapter 3 demonstrated that the ray theory is not valid when using low frequency guided waves to detect and size defects of the dimension of interest in this project: 60 mm diameter over a propagation distance of approximately 1 m. From this conclusion the obvious option is to increase the frequency up to the point where the ray theory becomes valid.

However the number of modes that can propagate increases with the frequency and the signal processing becomes more complex. Above the cutoff of the high order modes it is difficult to excite and detect a single mode or allow for time of any mode as required in time-of-flight tomography. It is therefore difficult to produce a map of the thickness using high frequency guided wave modes with a time-of-flight tomography algorithm. But ultrasonic guided waves have other features that can be exploited to obtain the thickness of a partially accessible structure.

The aim of this chapter is to examine the possibility of using the high order modes cutoff property mentioned in chapter 2 to obtain the minimum thickness between a source and a sensor. The petrochemical industry is particularly interested in obtaining the minimum remaining thickness over a large area without necessarily having the precise location of the various thickness reductions. The principle investigated in this chapter is to excite a large number of guided wave modes and have a sensor on the other side of the area of inspection to detect the guided wave modes that propagate through the inspection area. If the guided wave modes detected by the sensor can be identified, it is possible to obtain an approximation of the minimum thickness between the source and the sensor. This idea, using a single guided wave mode, has been investigated in the past [39–42]. However the limitation of this technique using a single mode is that it is only possible to evaluate whether the thickness is smaller or larger than a given value depending whether the mode is detected or not. Moreover for this technique to interrogate only the path between two transducers the ray theory needs to be valid, which was not taken into account in the previously published studies.

This chapter investigates the possibility of using multiple guided wave modes to obtain an estimation of the thickness and proposes a novel approach using the validity of the ray theory to select the frequency of excitation. The first section details the theoretical principle to use the cutoff property of the high order guided wave modes as well as the principle for the excitation and detection of the guided wave modes of interest with an array of transducers. The second section discusses details of the FE simulations for randomly varying thickness in the area of inspection. In the third section the issues of the experimental implementation are examined.

4.2 Theory

Figure 4.1 presents (a) the Lamb wave and (b) the SH wave phase velocity dispersion curves in an aluminium plate (E = 70.8 GPa, $\nu = 0.34$ and $\rho = 2700$ kg/m^3). Only the three fundamental modes (A_0, S_0 and SH_0) can propagate at all frequency thickness products. As detailed in chapter 2 the high order modes exhibit a cutoff frequency thickness product where the phase velocity approaches infinity. For the

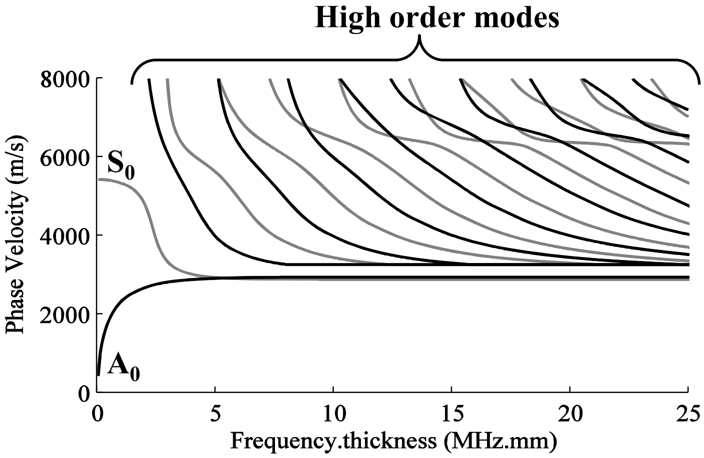

(*a*)

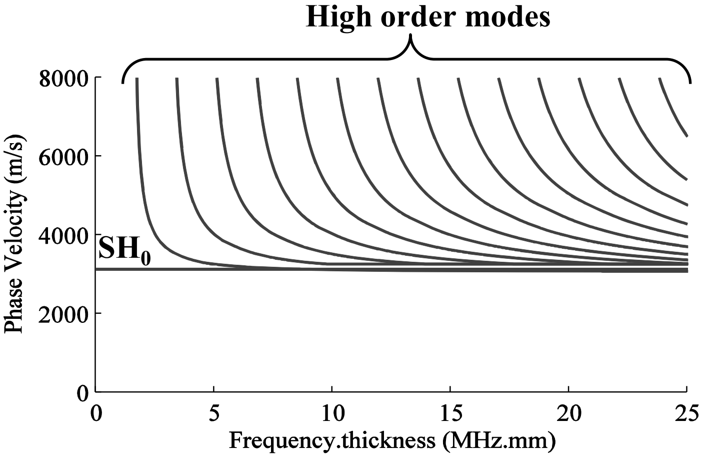

(*b*)

Figure 4.1: *(a) Lamb wave phase velocity dispersion curves in an aluminium plate (E = 70.8 GPa, ν = 0.34 and ρ = 2700 kg/m^3). The black solid lines correspond to the* A_n *modes, the light grey solid lines correspond to the* S_n *modes. (b)* SH *wave phase velocity dispersion curves in an aluminium plate.*

Lamb wave modes these cutoffs represent the frequency thickness product at which a standing longitudinal or shear wave is present across the thickness of the wave guide [13]. Traditionally ultrasonic guided waves have been mainly used below the cutoff frequency thickness product of the high order modes, the signal processing being simpler because only the three fundamental modes can propagate. Below the cutoff frequency thickness product of any given high order mode, no energy of this given mode can propagate in the structure.

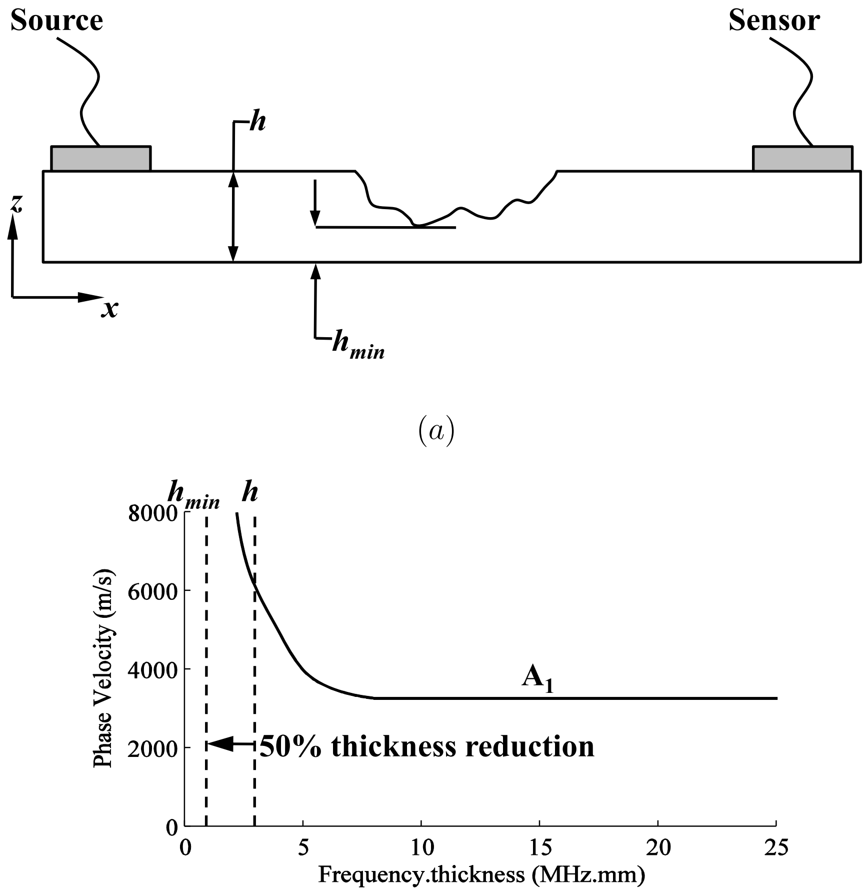

(*a*)

(*b*)

Figure 4.2: *(a) Source and sensor configuration to use the mode cutoff property to detect the minimum thickness h_{min} and (b) the phase velocity dispersion curve for the* A_1 *mode in an aluminium plate. The vertical dashed lines correspond to the frequency thickness product at h and h_{min} when the input signal is at 0.3 MHz in a 10 mm aluminium plate.*

Fundamentally the presence of corrosion is simply a change in the waveguide thickness. The significance of the high order modes cutoff property is that if a thickness reduction is present along the propagation path such that the frequency thickness product was shifted below the cutoff frequency thickness product of a given mode no energy of that mode would propagate through the reduced thickness region. The energy would be partially reflected and converted into lower order modes. If there is a source and a sensor on either side of a reduced thickness area as shown in figure 4.2 (a) then only the guided wave modes that can propagate at the corresponding frequency thickness product at h_{min} will be detected by the sensor. Therefore the effect of the thickness reduction in this case is similar to the effect of a low pass filter in signal processing. For example if h was 10 mm and h_{min} was 5 mm in an aluminium plate and a pure A_1 mode was excited by the source at 0.3 MHz, which corresponds to a frequency thickness product of 3 MHz.mm, then the A_1 mode would not be detected by the sensor because its cutoff frequency thickness product is 1.56 MHz.mm and the frequency thickness product at h_{min} is 1.5 MHz.mm. This phenomenon is illustrated in figure 4.2 (b). The limitation of this technique using a single mode is that it is only possible to determine whether the thickness is smaller or larger than a given value depending whether the mode is detected or not. However the technique becomes much more interesting if multiple guided wave modes with different cutoff frequency thickness products are excited as it becomes possible to get a good estimate of the minimum thickness between a source and a sensor by identifying the guided wave modes detected by the sensor. The SH modes are particularly interesting as they appear at regular intervals on the frequency thickness product axis (see figure 4.1 (b)). The benefit of using SH modes is that it is possible to estimate the minimum remaining thickness at a regular interval.

For this technique to interrogate only the path between the two transducers the ray theory must be valid. In chapter 3 the validity criteria of the ray theory were detailed and can be expressed as

$$d \gg \lambda \quad \text{and} \quad d \gg L_F \tag{4.1}$$

where d is the characteristic size of the defect, λ is the wavelength at the frequency of interest and L_F is the width of the Fresnel zone at the mid point between the source and the sensor which can expressed as

$$L_F(L/2) = \sqrt{\lambda L} \tag{4.2}$$

where L is the distance between the source and the sensor. The problem of interest is to obtain the maximum depth of a defect with a diameter of 60 mm or more and a separation distance between the source and the sensor of approximately 1 m. The ray theory would become valid if the wavelength λ is 3.6 mm or smaller. The frequency required to have a wavelength of this size depends on the thickness of the

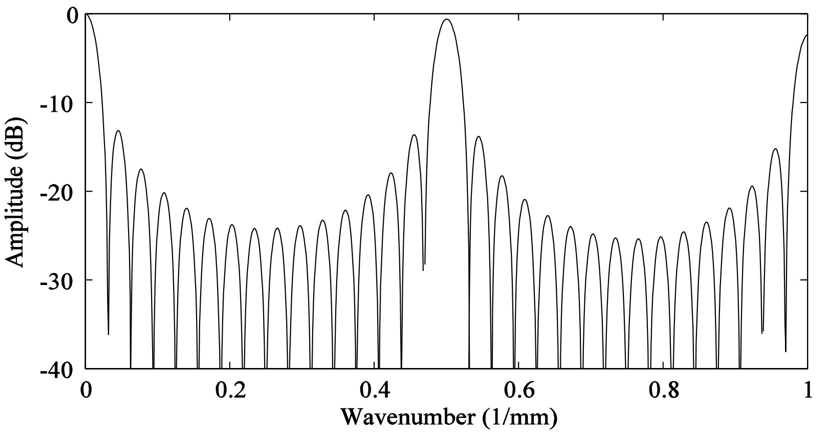

Figure 4.3: *Amplitude of excitation as a function of the wavenumber for a 16 element array with a spacing of 2 mm between each element.*

plate under inspection. The initial study will be carried out on a 10 mm aluminium plate on which the wavelength is 3.6 mm around 1 MHz for the fundamental SH mode.

The strategy for the excitation and detection of multiple modes is to use an array of transducers. The main advantage of using an array for the excitation is, to some extent, to control the modes that are excited. If all the elements of an array are fired at the same time then the modes with a wavelength corresponding to the spacing between each element are excited with a larger amplitude. Figure 4.3 illustrates this principle with a 16 element array with a spacing of 2 mm between each element where the amplitude of excitation is presented as a function of the wavenumber. This spectrum was obtained by taking the spatial Fourier transform of the array pattern (element size and spacing) as explained in [54]. The reason for the maximum at zero wavenumber is that all elements of the array are firing in the same direction at the same time which produces a DC component. This DC component is not relevant in this case. More importantly, there is a local maximum at 0.5 mm^{-1} which corresponds to a wavelength of 2 mm or the spacing between each element of the array. If such an array was used to excite multiple modes, then the modes with a wavelength of 2 mm would be dominant. This is in accordance with the wavelength required for the validity of the ray theory in the case of interest. For the SH modes the wavelength is 2 mm around 2 MHz in a 10 mm aluminium plate. Figure 4.4

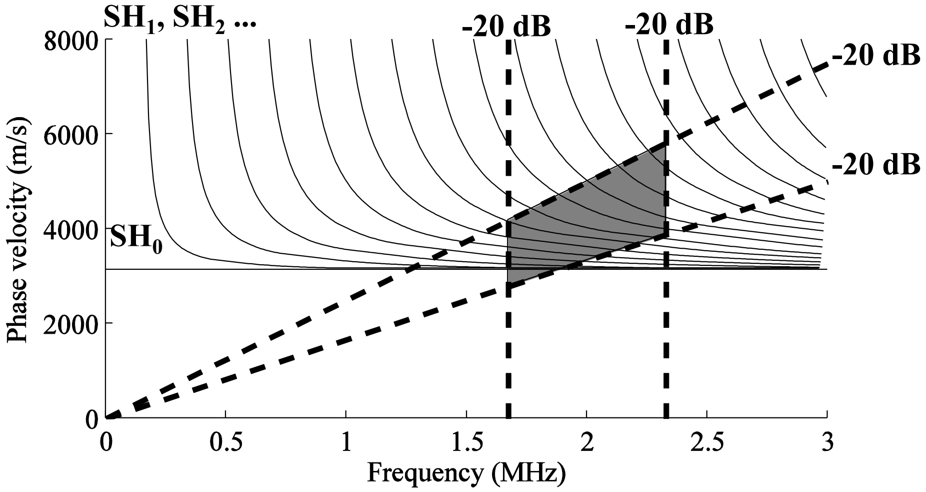

Figure 4.4: *SH modes phase velocity dispersion curves for a 10 mm aluminium plate. The grey box corresponds to the area that is dominantly excited by a 16 element array when the input signal is a 10 cycle Hanning windowed toneburst centred at 2 MHz. The vertical dashed lines correspond to the frequencies that are 20 dB down from the amplitude at 2 MHz and the diagonal dashed lines correspond to the wavenumber that are 20 dB down from the amplitude at 0.5* mm^{-1}.

presents the SH mode dispersion curves in a 10 mm aluminium plate. The grey box corresponds to the area that is dominantly excited by a 16 element array when the input signal is a 10 cycle Hanning windowed toneburst centred at 2 MHz. The vertical dashed lines correspond to the frequencies that are 20 dB down from the ampltitude at 2 MHz and the diagonal dashed lines correspond to the wavenumbers that are 20 dB down from the amplitude at 0.5 mm^{-1}.

The modes SH$_0$ to SH$_{12}$ are contained within the grey box. These modes all have a different cutoff frequency thickness product such that by identifying which modes propagate through a thickness reduction it is possible to obtain the minimum remaining thickness in the defect. The amplitude of each mode contained within the grey box also depends on the mode excitability. The excitability is defined in [44] as the ratio of displacement of a mode to applied force when both quantities are measured at the same location and direction in the cross section. Figure 4.5 shows the excitability of the SH mode up to 3 MHz in a 10 mm aluminium plate. The SH mode excitability was obtained from the ratio of surface displacement in the direc-

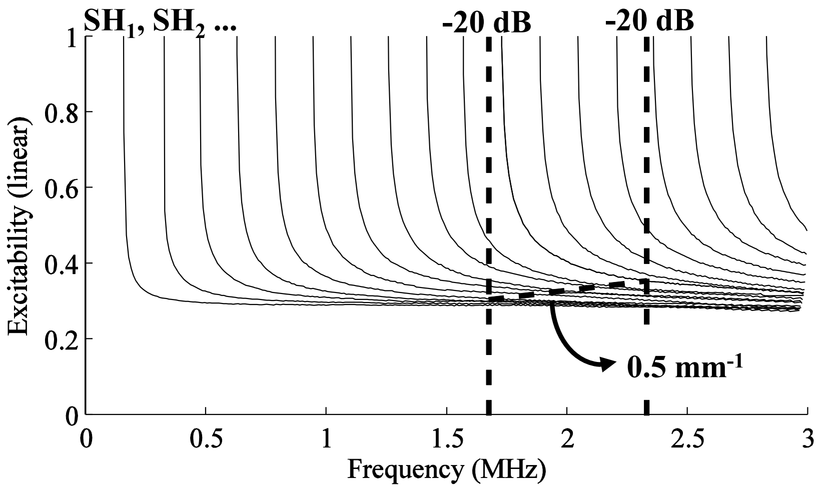

Figure 4.5: *SH modes excitability in a 10 mm aluminium plate. The vertical dashed lines correspond to the frequencies product that are 20 dB below the maximum when the input signal is a 10 cycle Hanning windowed toneburst centred at 2 MHz and the diagonal dashed line corresponds to 0.5* mm^{-1}*, the centre wavenumber excited by the 16 element array.*

tion normal to the $x-z$ plane in figure 4.2 (a) to surface force in the same direction when measured at the same point on the surface. The excitability is plotted on an arbitrary linear scale varying between 0 and 1. The vertical dashed lines correspond to the frequencies that are 20 dB down from the amplitude at 2 MHz and the diagonal dashed line corresponds to the wavenumber 0.5 mm^{-1}. The excitability of the modes crossing the 0.5 mm^{-1} diagonal line in the frequency bandwidth of interest varies between 0.3 and 0.35 or slightly more than 1 dB. Therefore in the rest of the chapter the excitability of the SH modes excited by a 16 element array in the frequency bandwidth of interest will be assumed constant.

Figure 4.6 presents a 2D frequency wavenumber map of the energy excited by the 16 element source array when the input signal is a 10 cycle Hanning windowed toneburst centred at 2 MHz. This map was obtained by multiplying the wavenumber spectrum of the 16 element array presented in figure 4.3 and the frequency spectrum of a 10 cycle Hanning windowed toneburst centred at 2 MHz.

By using this type of array most of the energy is concentrated on a vertical line around 0.5 mm^{-1}. The strategy for the detection of the modes is to use the same

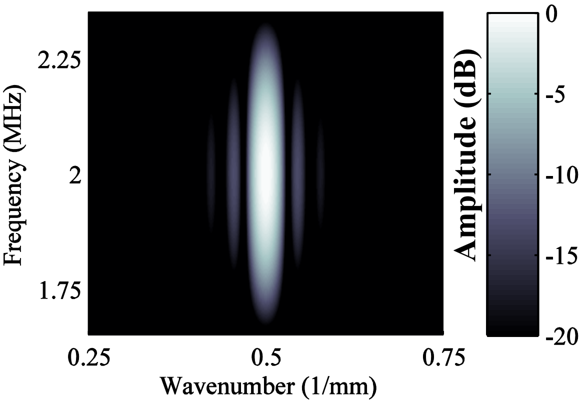

Figure 4.6: *2D frequency wavenumber map of the energy excited by a 16 element source array when the input signal is a 10 cycle Hanning windowed toneburst.*

array design as for the excitation. Using the same array design for excitation and detection provides flexibility when scanning a large area as the source and sensor arrays become interchangeable.

For the identification of the modes a 2D Fourier transform [55] is performed on the time traces detected by the individual elements of the sensor array. The 2D Fourier transform provides an excellent tool to identify the modes detected by the sensor array. In this case the issue with using the same array design for excitation and detection is that when performing the 2D Fourier transform the Nyquist wavenumber of the sensor array is below the wavenumber bandwidth of interest. In the example used above, a 16 element array with a spacing of 2 mm between each element, the Nyquist wavenumber is 0.25 mm^{-1} whereas the wavenumber bandwidth of interest is between 0.25 and 0.75 mm^{-1}. Figure 4.7 shows the relationship between the true wavenumbers and the apparent wavenumbers in the Nyquist interval (-0.25 to 0.25 mm^{-1}).

Physically the negative wavenumber simply means that the waves are traveling in the opposite direction in comparison with the positive wavenumber. The aliasing means that if there are components at 0.4 mm^{-1} and -0.6 mm^{-1}, then both these wavenumbers would appear at 0.1 mm^{-1} in the Nyquist interval. If a plate had infinite dimensions with no defects and a source/sensor configuration as in figure 4.2 then the waves will arrive at the sensor from only one direction such that the

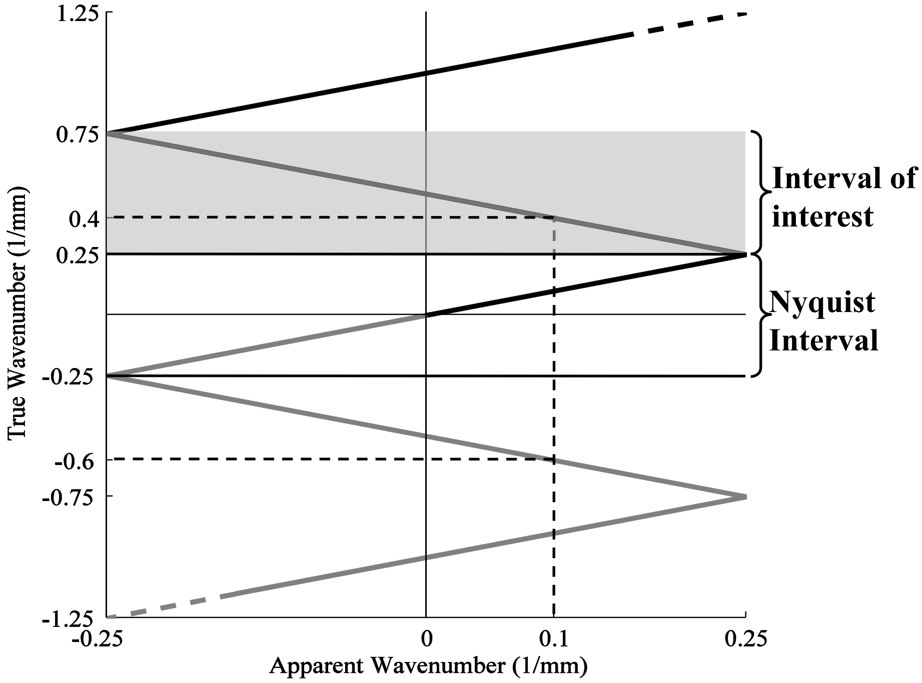

Figure 4.7: *Location where the true wavenumbers map in the apparent of Nyquist wavenumber interval. True wavenumbers 0.4* mm^{-1} *and -0.6* mm^{-1} *would both appear at 0.1* mm^{-1}*. The grey area corresponds to the wavenumber interval of interest.*

wavenumber detected will be either positive or negative depending on the convention used. Moreover if the 16 element array described above is used for excitation then most of the energy is contained in the wavenumber bandwidth between 0.25 and 0.75 mm^{-1} (see figure 4.3 and 4.6). As there is virtually no energy propagating outside of this wavenumber bandwidth, it is possible to use aliasing to detect wavenumbers outside of the Nyquist interval. In this study the interval of interest is between 0.25 and 0.75 mm^{-1} which respectively map at 0.25 and -0.25 mm^{-1} in the Nyquist interval. This implies that 0.5 mm^{-1} maps at 0 mm^{-1} and as explained earlier, 0.4 mm^{-1} maps at 0.1 mm^{-1}.

When there is no thickness reduction between a source array and a sensor array the 2D Fourier transform of the time traces detected by the individual elements of the sensor array should look very similar to figure 4.6 except that there will be gaps on the line at 0.5 mm^{-1} because only a finite number of modes is excited. If there are thickness reductions between the source and sensor arrays, then depending on the minimum thickness, the maximum frequency where there is energy at 0.5 mm^{-1}

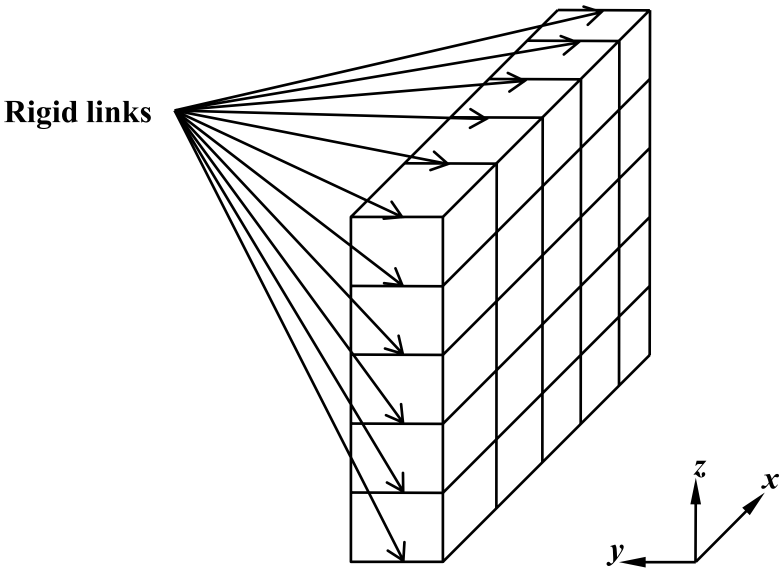

Figure 4.8: *Schematic of the FE model used to simulate the propagation of SH waves.*

will decrease. This phenomenon will be examined in the next section using an FE model.

4.3 Finite Element Simulations

4.3.1 Finite Element Model

In order to accurately model wave propagation with FE, at least 10 to 15 elements per wavelength are required [49]. When modelling high frequency wave propagation the size of the models rapidly increases. This section is interested in modelling SH wave propagation around 2 MHz in a 10 mm aluminium plate over a distance of approximately 1 m. Fortunately in this range of frequency the ray theory is valid to detect a defect of 60 mm diameter. This implies that a 2D plane strain model should be sufficient. It is unfortunately impossible to directly model SH waves in Abaqus because the 2D plane strain elements have no out of plane degree of freedom and a full 3D model was deemed too computer-intensive. Figure 4.8 presents a schematic of the method used for the modelling of SH waves in Abaqus.

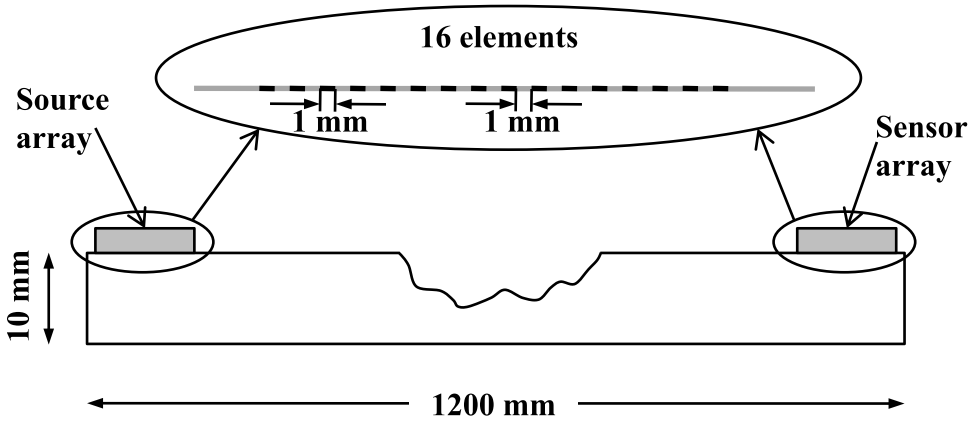

Figure 4.9: *Schematic of the FE model used in the next subsection.*

The method uses a single layer of 3D elements and for all nodes of the model the degrees of freedom in x and z are blocked such that only SH waves can propagate. Moreover each node of the $x - z$ plane is rigidly linked to its corresponding node in the other $x - z$ plane such that the displacement in the y direction is the same for all pairs of nodes as if there was only one 2D plane strain element. By using this strategy the model is approximately twice the size of a true 2D plane strain model, but much smaller than a full 3D model.

In all the simulations in the next subsection the plate was 1200 mm long and 10 mm thick. A schematic of the FE model is presented in figure 4.9. The material was aluminium (E = 70.8 GPa, ν = 0.34 and ρ = 2700 kg/m^3). Linear cubic-shaped 3D brick elements were used in the model and the length of all sides was 0.1 mm. There were therefore 100 elements in the thickness of the plate. The time step of the simulations was chosen in accordance with the element size. Absorbing boundaries [49, 50] were used to avoid reflections from both ends of the plate. Thickness reductions of various depths and lengths were introduced in the area of inspection between the source and sensor arrays.

The source and sensor arrays were modelled with 16, 1 mm wide transducer elements with a spacing between each transducer element of 1 mm, corresponding to 2 mm centre to centre. As the finite element size is 0.1 mm, each transducer element contains 10 finite elements. The reason for modelling the source and sensor arrays like this is to facilitate the experimental comparison and implementation. For each

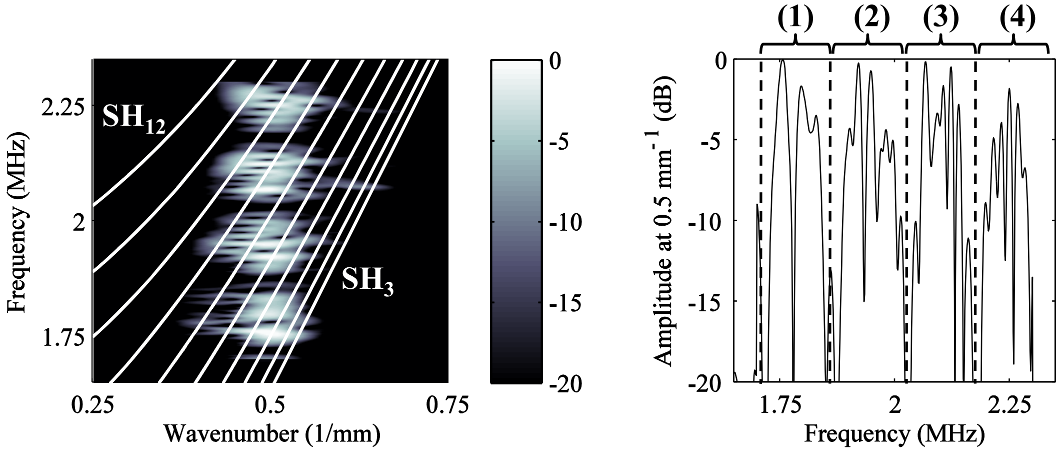

(*a*) (*b*)

Figure 4.10: *(a) 2D Fourier transform of the FE simulated signals when the plate has no defect and (b) the amplitude of the 2D Fourier transform at 0.5 mm^{-1} as a function of frequency. The white lines in (a) corresponds to the dispersion curves of the modes* SH_3 *to* SH_{12}.

node of the source array in the FE model, an out of plane force (direction y in figure 4.8) was applied with a 10 cycle Hanning windowed toneburst centred at 2 MHz as the input signal. The sensor array monitored the displacement in the out of plane direction (direction y in figure 4.8). In the sensor array the displacement detected by a 1 mm transducer element corresponded to the sum of the displacement at the 11 nodes of the transducer element.

The next subsection uses this FE model to evaluate the feasibility of using the cutoff property of the high order SH modes to evaluate the minimum remaining thickness between a source and a sensor over a distance of 1200 mm.

4.3.2 Finite Element Results

Figure 4.10 presents the 2D Fourier transform of the FE simulated signals received by a 16 element array when the plate under investigation has no thickness reduction. As the excitability of the SH modes excited by a 16 element array in the frequency bandwidth of interest is almost constant, the frequency weights of the Hanning window were compensated for in post-processing such that the amplitude of the excitation is approximately the same at all frequencies. The white lines in figure 4.10 (a) correspond to the dispersion curves for the modes SH_3 to SH_{12}.

As expected, when the plate has no defects all the modes excited are detected with the same amplitude and are confined around the wavenumber 0.5 mm^{-1}. In figure 4.10 (b) four clusters of modes can be identified in the frequency bandwidth of interest at the wavenumber 0.5 mm^{-1}. The maximum amplitude of all the clusters is the same except for the last one where the amplitude is approximately 2 dB down from the amplitude of the first cluster.

Figure 4.11 presents (a) a schematic of the FE model with a 600 mm long area where the thickness is varying randomly. To generate the randomly varying thickness area, a spline was passed through 20 points evenly distributed along the 600 mm area where the thickness was a random number in a given interval. In this case the thickness at the 20 points varied between 8 and 10 mm. The minimum remaining thickness was 8 mm, corresponding to a 20% thickness reduction. Figure 4.11 (b) is the corresponding 2D Fourier transform of the FE simulated signals received by a 16 element array and (c) corresponds to the amplitude of the 2D Fourier transform at 0.5 mm^{-1}.

The 2D Fourier transform presented in figures 4.10 (a) and 4.11 (b) are relatively similar up to approximately 2 MHz. In figure 4.11 (c) the first cluster is almost unaffected by the presence of a 20% thickness reduction. The maximum of the first cluster is still 0 dB, which corresponds to the maximum value of the 2D Fourier transform. The effect of the 20% thickness reduction is visible on the second, third and fourth clusters. The maximum amplitude of these clusters respectively decreased by approximately 2 dB, 7dB and 9 dB relative to the amplitude of the first cluster. Moreover above 2 MHz in figure 4.11 (b) the maximum amplitude is slightly shifted to higher wavenumber, which suggests that the modes excited in this frequency range have converted to lower modes. This is precisely the predicted phenomenon as the higher order modes are either reflected or converted to lower order modes when they cannot propagate at the minimum remaining thickness. From the cutoff

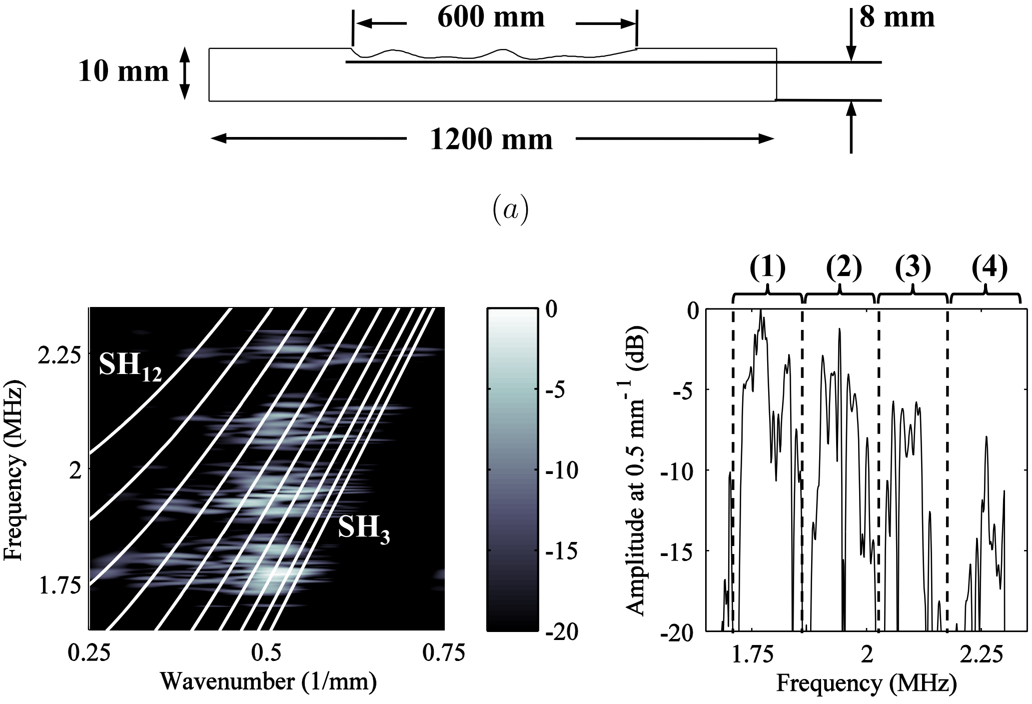

(*a*)

(*b*) (*c*)

Figure 4.11: *(a) Schematic of the plate with a 600 mm long area where the thickness is varying randomly with a maximum depth of 2 mm, (b) the corresponding 2D Fourier transform of the FE simulated signals and (c) the amplitude of the 2D Fourier transform at 0.5 mm*$^{-1}$ *as a function of frequency. The white lines in (b) corresponds to the dispersion curves of the modes* SH_3 *to* SH_{12}.

frequency thickness product of each mode in the dispersion curves (figure 4.4) the amplitude of the modes above SH_8 should be attenuated or converted to lower order modes when the minimum remaining thickness is 8 mm. The SH_8 mode is excited with a wavenumber of 0.5 mm^{-1} at 2 MHz. In the FE results an amplitude change of 7 to 9 dB was observed above 2 MHz for the third and fourth clusters relative to the amplitude of the first cluster.

Figure 4.12 presents (a) a schematic of the FE model with a 600 mm long area where the thickness is varying randomly and the minimum remaining thickness is 7 mm corresponding to a 30% thickness reduction. Figure 4.12 (b) is the corresponding 2D Fourier transform of the FE simulated signals received by a 16 element array and (c) corresponds to the amplitude of the 2D Fourier transform at 0.5 mm^{-1}.

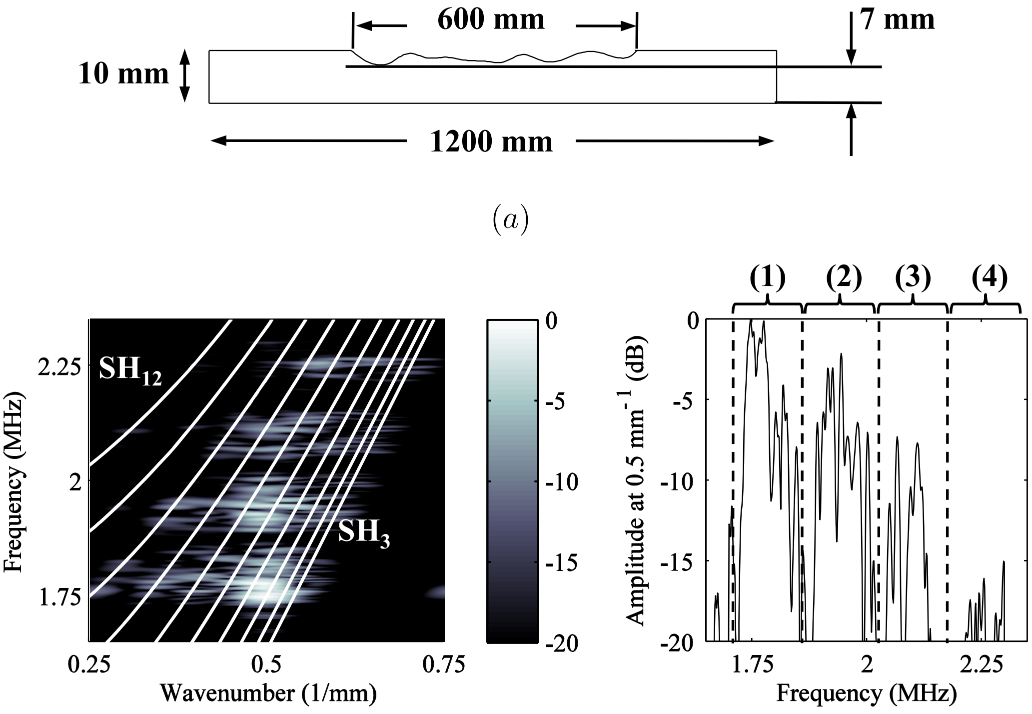

(a)

(b)

(c)

Figure 4.12: *(a) Schematic of the plate with a 600 mm long area where the thickness is varying randomly with a maximum depth of 3 mm, (b) the corresponding 2D Fourier transform of the FE simulated signals and (c) the amplitude of the 2D Fourier transform at 0.5 mm^{-1} as a function of frequency. The white lines in (b) corresponds to the dispersion curves of the modes* SH_3 *to* SH_{12}.

From figure 4.11 (b) to figure 4.12 (b) the minimum remaining thickness was reduced by 10%, from 8 mm to 7 mm and the 2D Fourier transforms have similarities. As for the 20% thickness reduction, the maximum amplitude of the first cluster is unaffected by the presence of a 30% thickness reduction. The maximum amplitude of the second, third and fourth clusters is respectively -3 dB, -8 dB and approximately -15 dB relative to the amplitude of the first cluster. In comparison with the 20% thickness the amplitude of the fourth cluster was the most affected. Once again above 2 MHz it can be observed that a significant part of the energy was converted to lower order modes which created a shift to higher wavenumbers. From the cutoff frequency thickness product of each mode in the dispersion curves (figure 4.4) the amplitude of the modes above SH_8 should once again be attenuated or converted to

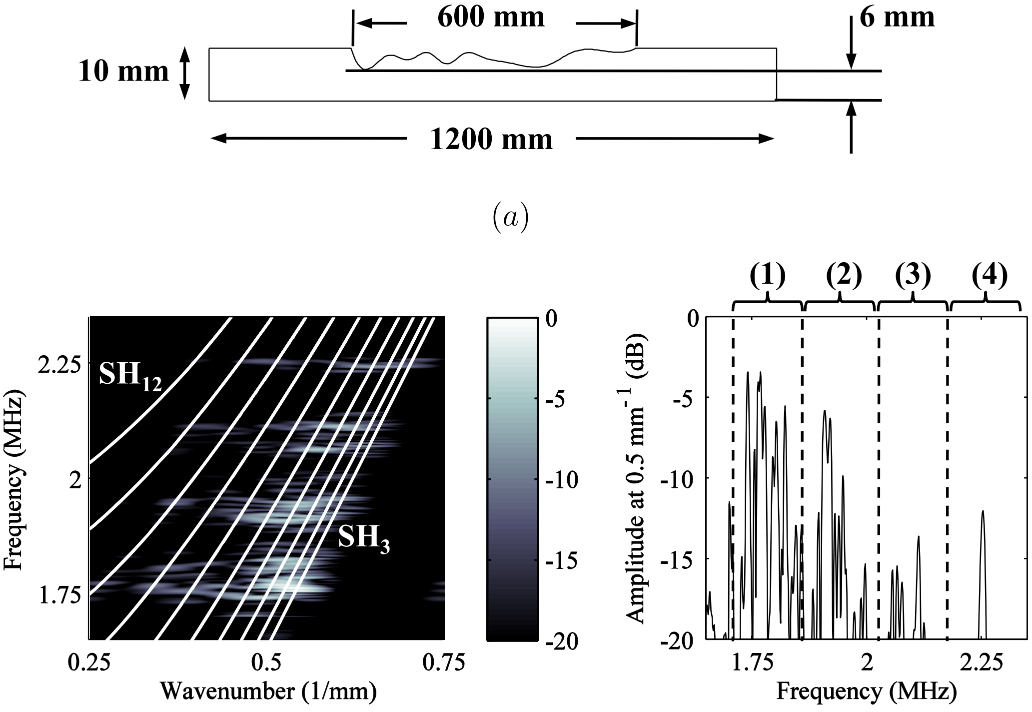

(*a*)

(*b*) (*c*)

Figure 4.13: *(a) Schematic of the plate with a 600 mm long area where the thickness is varying randomly with a maximum depth of 4 mm, (b) the corresponding 2D Fourier transform of the FE simulated signals and (c) the amplitude of the 2D Fourier transform at 0.5 mm*$^{-1}$ *as a function of frequency. The white lines in (b) corresponds to the dispersion curves of the modes* SH$_3$ *to* SH$_{12}$.

lower order modes when the minimum remaining thickness is 7 mm, which corresponds to what can be observed. The difference in the frequency thickness product between a minimum remnant thickness of 7 and 8 mm is small such that the number of modes affected by the thickness reduction remains the same.

Figure 4.13 presents (a) a schematic of the FE model with a 600 mm long area where the thickness is varying randomly and the minimum remaining thickness is 6 mm corresponding to a 40% thickness reduction. Figure 4.13 (b) is the corresponding 2D Fourier transform of the FE simulated signals received by a 16 element array and (c) corresponds to the amplitude of the 2D Fourier transform at 0.5 mm^{-1}.

From figure 4.12 (b) to figure 4.13 (b) the minimum remaining thickness was reduced by another 10%, from 7 mm to 6 mm and some changes appeared in the 2D Fourier transforms of the data. In this case the maximum amplitude of the first cluster at 0.5 mm^{-1} dropped by approximately -4 dB relative to the maximum amplitude of the 2D Fourier transform. Therefore the maximum amplitude is no longer on the wavenumber line at 0.5 mm^{-1} but at a slightly higher wavenumber at 0.52 mm^{-1}. All the modes in the frequency range of interest have shifted to higher wavenumbers, which correspond to lower order modes. The maximum amplitude of the second, third and fourth cluster is respectively -6 dB, -13 dB and -12 dB relative to the maximum value of the 2D Fourier transform map. For the fourth cluster the maximum is -12 dB but apart from that peak value, the amplitude was below below -20 dB. From the cutoff frequency thickness product of each mode in the dispersion curves (figure 4.4) the amplitude of the modes above SH_6 should be attenuated or converted to lower order and this is precisely what can be observed in figure 4.13.

Figure 4.14 presents (a) a schematic of the FE model with a 600 mm long area where the thickness is varying randomly and the minimum remaining thickness is 5 mm corresponding to a 50% thickness reduction. Figure 4.14 (b) is the corresponding 2D Fourier transform of the FE simulated signals received by a 16 element array and (c) corresponds to the amplitude of the 2D Fourier transform at 0.5 mm^{-1}.

From figure 4.13 (b) to figure 4.14 (b) the minimum remaining thickness was reduced by 10%, from 6 mm to 5 mm. In figure 4.14 (b) all the modes have further shifted to higher wavenumber in comparison with figure 4.13 (b). This is expected as the minimum thickness decreased. The maximum amplitude of the first and second clusters is respectively -4 dB and -12 dB down from the maximum amplitude of the 2D Fourier transform at 0.55 mm^{-1}. The maximum amplitude of the third and fourth cluster is now below -20 dB relative to the maximum amplitude of the 2D Fourier transform. From the cutoff frequency thickness product of each mode in the dispersion curves (figure 4.4) the amplitude of the modes above SH_4 should be attenuated or converted to lower order. It is relatively difficult to observe this in figure 4.14 as the SH_3, SH_4 and SH_5 are excited below 1.75 MHz at 0.5 mm^{-1}. However all the modes excited above 1.75 MHz have converted to lower order modes.

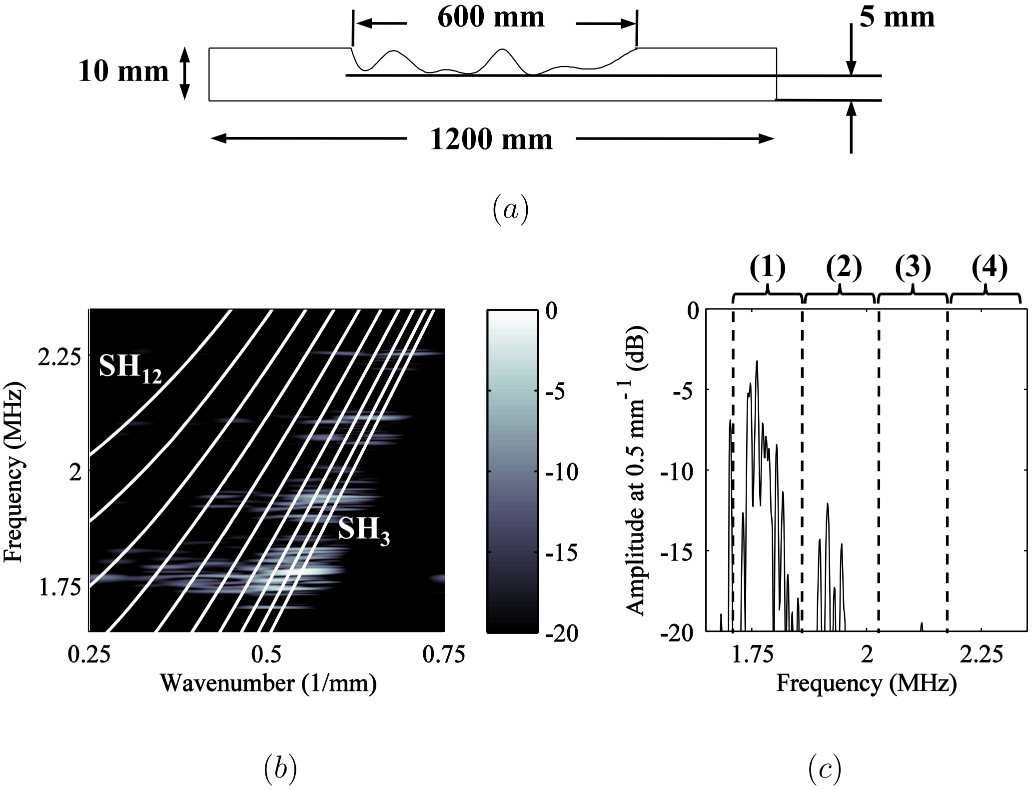

(*a*)

(*b*)

(*c*)

Figure 4.14: *(a) Schematic of the plate with a 600 mm long area where the thickness is varying randomly with a maximum depth of 5 mm, (b) the corresponding 2D Fourier transform of the FE simulated signals and (c) the amplitude of the 2D Fourier transform at 0.5 mm^{-1} as a function of frequency. The white lines in (b) corresponds to the dispersion curves of the modes* SH$_3$ *to* SH$_{12}$.

In the results presented above the amplitude of the clusters relative to the maximum amplitude of the 2D Fourier transform appears to be related to the remnant thickness between the two transducers. Figure 4.15 shows the integrated amplitude of each cluster relative to the no defect case as a function of the cluster index at 0.5 mm^{-1} for the four cases studied above. The amplitude variation of the clusters is a function of the depth of the thickness reduction, the smallest amplitude change being observed with the 20% deep case and the largest amplitude change for the 50% deep case. The amplitude of the clusters relative to the no defect case is therefore related to the remnant thickness between the two transducers.

It is interesting to note that the amplitude of the 20% and 30% deep cases are very similar up to the second cluster but lower than the amplitude of the no defect case.

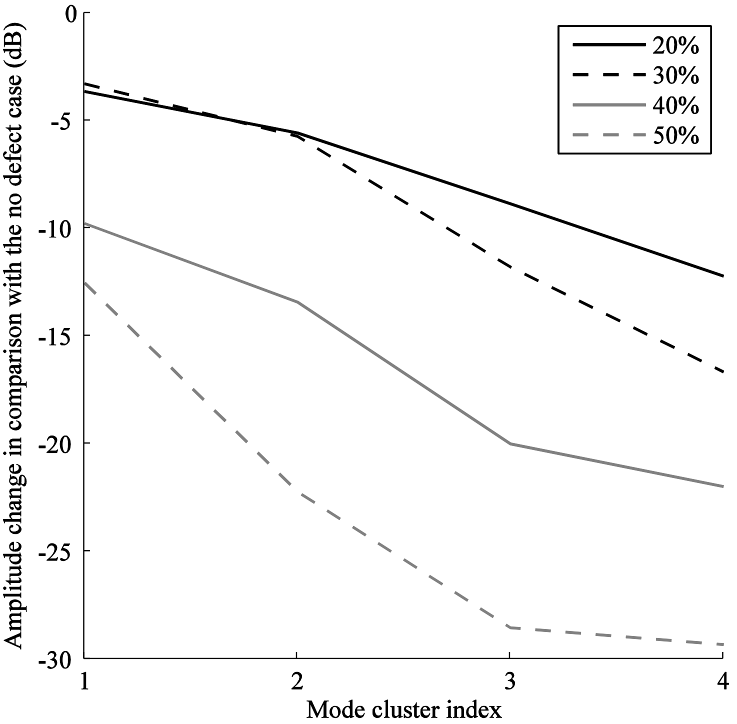

Figure 4.15: *Comparison of the integrated amplitude of each cluster relative to the amplitude of the no defect case for the 20%, 30%, 40% and 50% deep cases.*

Even if the modes contained in the first two clusters in these cases can propagate in the thinnest region of the plate, reflection will happen at the defects and the amplitude of the modes contained in these clusters will necessarily be lower than the no defect case.

The FE simulations demonstrated that the cutoff property of the high order modes can be used to obtain an indication of the minimum remaining thickness between a source and a sensor. When the frequency thickness product is shifted below the cutoff of a given mode because of a thickness change, then this mode is partially reflected and converted to lower order modes. By identifying the first mode that was converted to a lower order mode, it is possible get an approximation of the minimum remaining thickness. In the simulations above, the input signal was a 10 cycle Hanning windowed toneburst centred at 2 MHz. This input signal is well suited to detect thickness reduction between 20% and 40%. To detect deeper defect the centre frequency should be reduced. The next section investigates if the same conclusions apply experimentally.

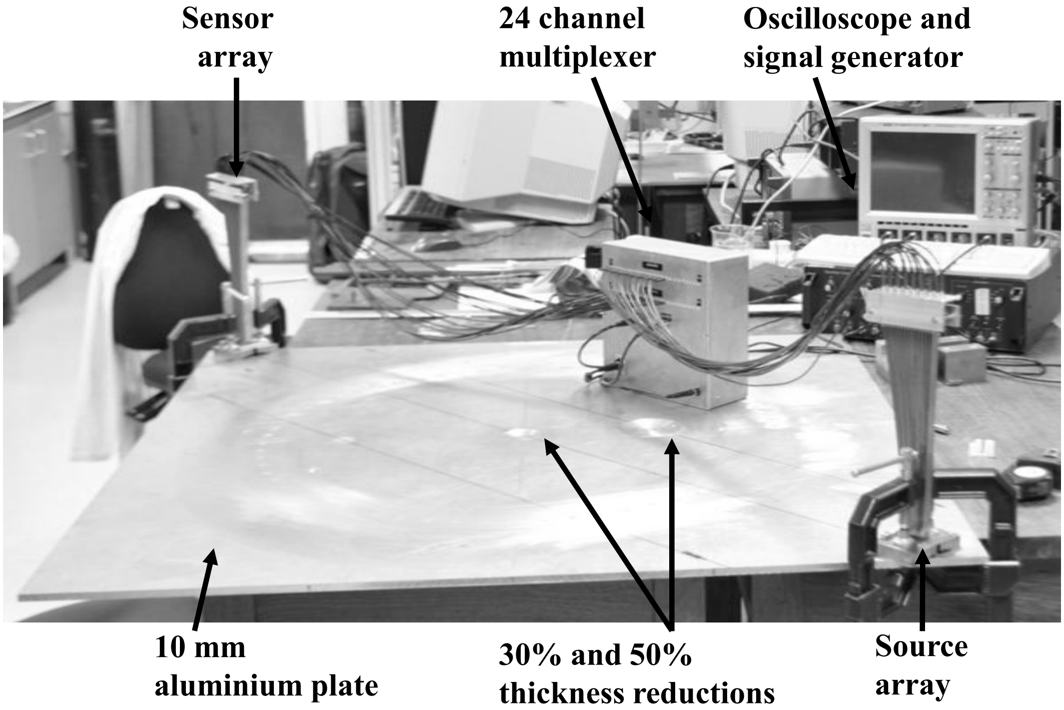

Figure 4.16: *Photo of the experimental setup with two arrays attached to a 1200 mm × 1200 mm × 10 mm aluminium plate. The plate contains two thickness reductions: a 60 mm diameter 50% deep and a 100 mm diameter 30% deep.*

4.4 Experiments

4.4.1 Experimental Setup

The experimental setup presented in figure 4.16 comprised a 1200 × 1200 × 10 mm aluminium plate with two thickness reductions: a 60 mm diameter 50 % deep defect and a 100 mm diameter 30% deep defect.

Two 16 element arrays (figure 4.17) are clamped to the plate. Each array is composed of 16 waveguide transducers designed to excite SH waves around 2 MHz. These arrays were developed for high temperature crack monitoring and more details can be found in [56] and [57]. Although this project is not interested in high temperature crack monitoring, these arrays are perfectly suited to the application investigated in this chapter. Each waveguide transducer is 1 mm thick and the spacing between each transducer in the array is 1 mm, corresponding to 2 mm centre to centre. The

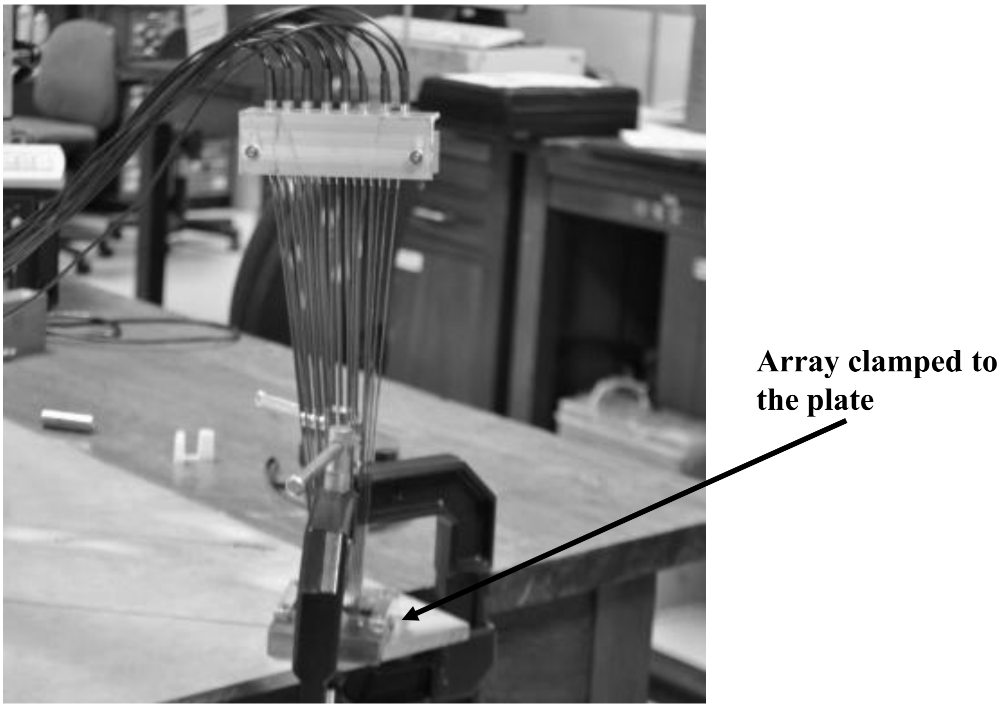

Figure 4.17: *Zoom on one of the 16 element arrays.*

size and spacing of the waveguide transducer corresponds exactly to the parameters used in the FE simulations. The contact between the transducers and the plate is maintained by two springs and two clamps and the coupling is assumed to be constant across all transducers. All the experimental data was obtained using a 10 cycle Hanning windowed toneburst centred at 2 MHz. Once again the weights given to each frequency by the Hanning window are compensated for in post-processing such that the amplitude of excitation becomes approximately constant across the frequency bandwidth of interest.

In the FE simulations absorbing boundaries were used to remove reflections from the edges of the plate. The reflections from the edges would produce negative wavenumbers and would contaminate the wavenumber outside of the Nyquist interval (see figure 4.7). In the processing of the data, aliasing is used to obtain wavenumber above the Nyquist wavenumber. In experiments the idea is to carry out the measurement on a diagonal across the plate such that the reflections from the edges would be reflected away from the sensor array. This strategy is illustrated in figure 4.18 (a).

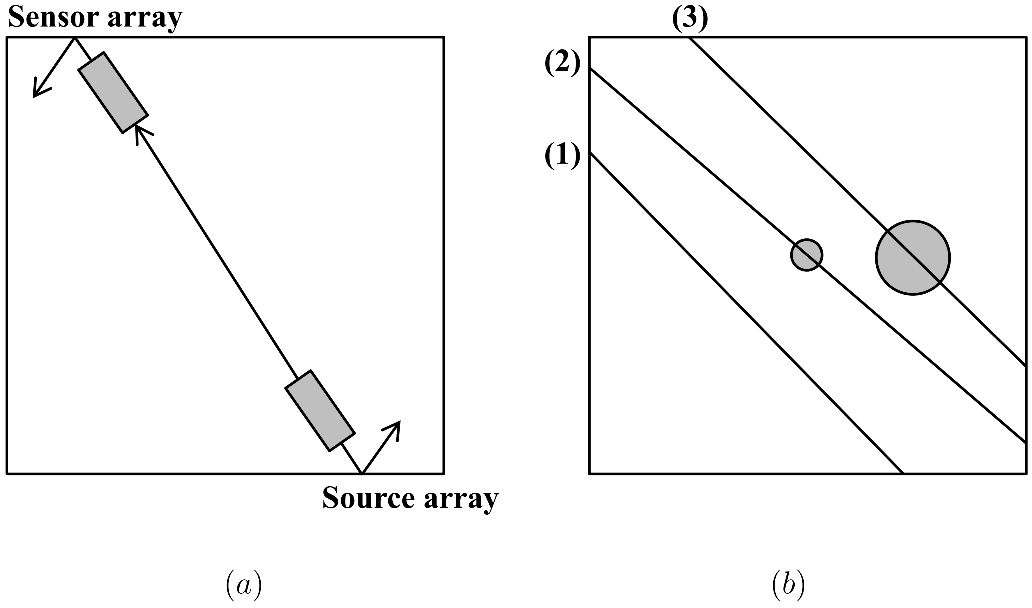

(a) (b)

Figure 4.18: *(a) Strategy to avoid that the reflection from the edges of the plate is detected by the sensor array and (b) location of the three different measurements presented in this section: (1) no defect case, (2) 60 mm diamter 50% deep and (3) 100 mm diameter 30% deep.*

Three different experimental measurements were carried out. These three measurements are illustrated in figure 4.18 (b). The first measurement is on a path where there were no thickness reductions, in the second measurement there is a 60 mm diameter 50% deep thickness reduction approximately mid way between the source and sensor arrays and finally in the third measurement there is a 100 mm diameter 30 % deep thickness reduction also approximately mid way between the source and sensor arrays. In the next subsection these three experimental cases are studied in detail.

4.4.2 Experimental Results

Figure 4.19 presents the 2D Fourier transform of the experimental signals received by a 16 element array when the ray interrogating the plate has no thickness reduction ((1) in figure 4.18). The 2D Fourier transform obtained from the experimental data is relatively similar to the corresponding 2D Fourier transform presented in figure

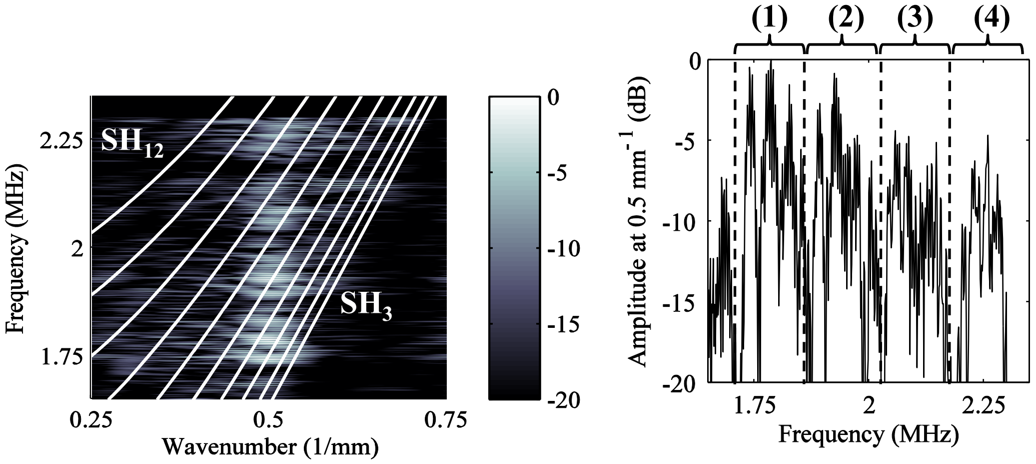

(*a*) (*b*)

Figure 4.19: *(a) 2D Fourier transform of the experimental signals when the plate has no defect and (b) the amplitude of the 2D Fourier transform at 0.5 mm^{-1} as a function of frequency. The white lines corresponds to the dispersion curves of the modes* SH_3 *to* SH_{12}.

4.10. Most of the energy is concentrated around 0.5 mm^{-1} but the amplitude is not constant across the frequency bandwidth of interest, the amplitude of the higher frequency components is lower than the lower frequency components. The variation in the amplitude of excitation of each transducer is slightly different which makes the 2D Fourier transform noisier. The cluster pattern observed in FE is still visible but in contrast with FE the maximum amplitude of the clusters is decreasing relative to the amplitude of the first cluster when the frequency increases.

Figure 4.20 presents (a) a schematic of the plate thickness when a ray travels through the 30% deep thickness reduction with a diameter of 100 mm ((3) in figure 4.18). The minimum remaining thickness was 7 mm. In figure 4.20 (b) is the corresponding 2D Fourier transform of the experimental signals received by a 16 element array.

The 2D Fourier transform presented in figures 4.20 (b) and 4.12 (b) are rather different. As for the no defect case the experimental 2D Fourier transform was noisier than the FE equivalent. All the modes above 1.75 MHz appeared to have converted to lower order modes. In figure 4.20 (c) the cluster pattern was much more difficult to observe. The amplitudes of the second, third and fourth clusters seemed to have dropped below the background noise level. Therefore it would be

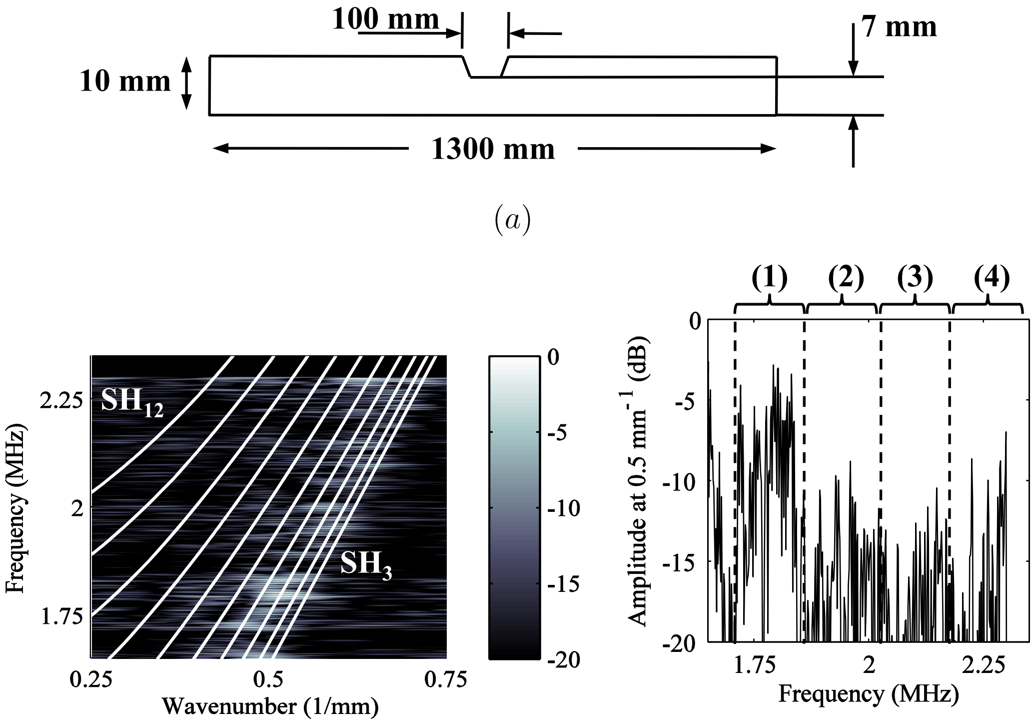

(*a*)

(*b*) (*c*)

Figure 4.20: *(a) Schematic of the plate with a 100 mm long and 30 % deep defect, (b) the corresponding 2D Fourier transform of the FE simulated signals and (c) the amplitude of the 2D Fourier transform at 0.5 mm^{-1} as a function of frequency. The white lines in (b) corresponds to the dispersion curves of the modes* SH$_3$ *to* SH$_{12}$.

difficult to obtain an accurate estimation of the thickness from this measurement as it is very different from the FE equivalent.

In order to verify the consistency of the experimental results, figure 4.21 presents (a) a schematic of the ray interrogating the plate when it travels through a 50% deep thickness reduction with a diameter of 60 mm ((2) in figure 4.18). In this case the minimum remaining thickness was 5 mm. The corresponding 2D Fourier transform of the experimental signals received by a 16 element array if shown in figure 4.21 (b). The 2D Fourier transform presented in figures 4.21 (b) and 4.14 (b) are again rather different. By comparing figures 4.20 (c) and 4.21 (c) the amplitude change across the frequency bandwidth of interest is not consistent with an increase of the defect depth of 20% as the amplitude of the first cluster should be much lower relative to the maximum amplitude of the 2D Fourier transform. The amplitude of the high

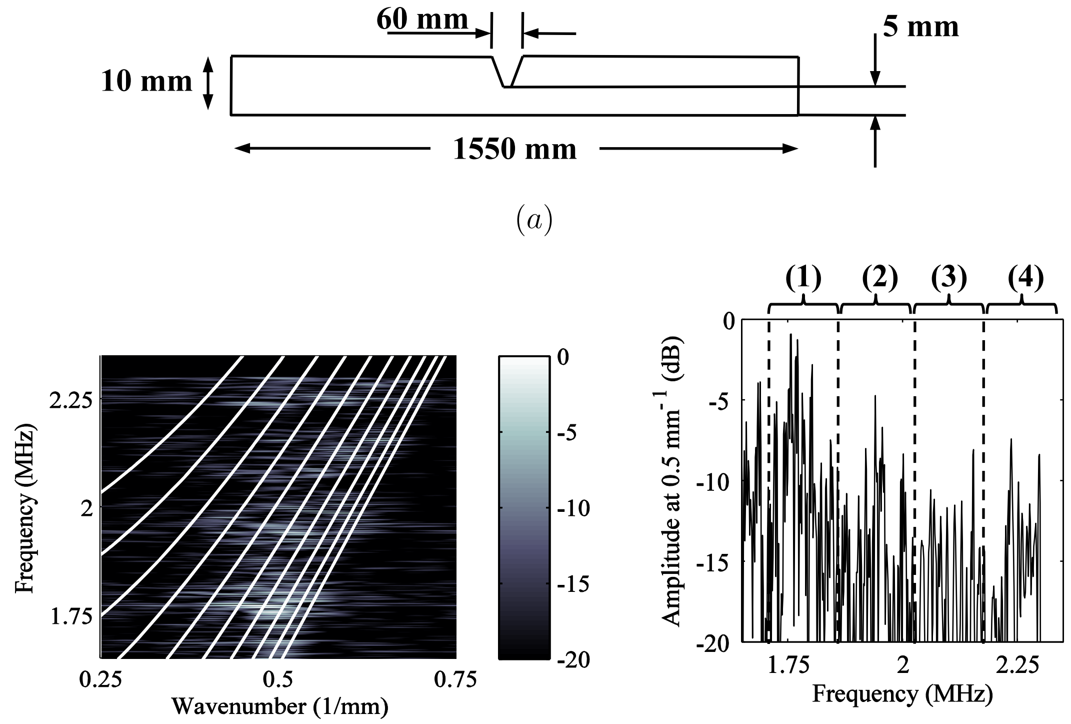

(*a*)

(*b*) (*c*)

Figure 4.21: *(a) Schematic of the plate with a 60 mm long and 50 % deep defect, (b) the corresponding 2D Fourier transform of the FE simulated signals and (c) the amplitude of the 2D Fourier transform at 0.5 mm^{-1} as a function of frequency. The white lines in (b) corresponds to the dispersion curves of the modes* SH_3 *to* SH_{12}.

frequencies relative to the low frequencies should be much lower as in figures 4.12 (c) and 4.14 (c).

Although the ray theory is valid in this case the experimental results obtained on a plate were very different from the FE predictions. The validity of the ray theory ensures that the signal is detected by a sensor without superposition from the interaction of the waves with features outside of the ray path. In the results presented above the signals recorded are relatively long so as to ensure that the slowest modes have the time to propagate to the sensor. When the time domain signal length is long it is possible that the fastest modes interact with features outside of the ray path e.g. other defects or plate boundaries and superpose with the slowest modes. Therefore increasing the length of the signal increases the size of the zone of interference of the ray for the slowest modes.

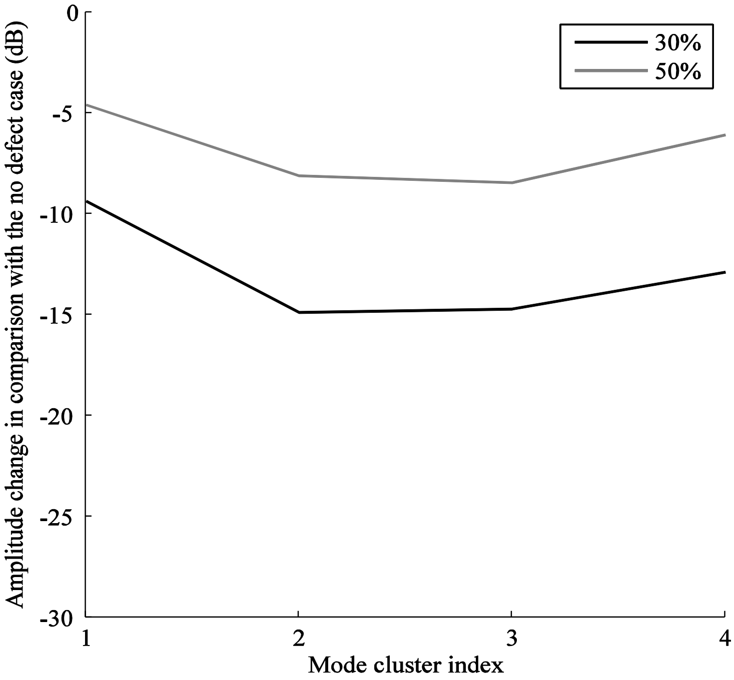

Figure 4.22: *Experimental comparison of the integrated amplitude of each cluster relative to the amplitude of the no defect case for the 30% and 50% deep cases.*

In contrast with FE, in the experimental results presented above the amplitude of the clusters relative to the maximum amplitude of the 2D Fourier transform does not appears to be related to the remnant thickness between the two transducers. Figure 4.22 shows the integrated amplitude of each cluster relative to the no defect case as a function of the cluster index at 0.5 mm^{-1} for the two experimental cases studied above. In contrast with the FE results where the amplitude of the clusters relative to the no defect case was related to the minimum remaining thickness the experimental results does not exhibit this feature. In fact precisely the opposite can be observed in figure 4.22, the amplitude of all the clusters relative to the no defect case for the 50% deep case is higher than the 30% case. This is potentially due to the fact that the surface finish at the defect is much rougher in the 30% case. In the 30% defect the roughness average i.e. the arithmetic average of the absolute vertical distance from the mean value, is of the order 50 μm whereas in the 50% defect the roughness average is of the order of 3 μm, which is the typical value for milling. The difference in roughness was due to the different processes used to machine the defects. At this stage a full understanding of the 3D interaction with thickness reduction of the SH wave at 2 MHz would be useful. However before going any further, a feasibility study of the propagation of high frequency SH waves through corrosion is essential.

4.4.3 Practical Feasibility

The idea is to evaluate if it is feasible for SH waves to propagate through corrosion when the input signal is centred at 2 MHz. A 10 mm thick steel plate lent by Shell Global Solutions with an accelerated corrosion patch was used for this measurement. The maximum depth of the corrosion was approximately 50% of the original plate thickness. Panametrics-NDT V154 shear transducers were located on either sides of the corrosion patch and the distance between the transducers was 250 mm. The corrosion patch was 130 mm long (a schematic of the setup is presented in figure 4.23 (a)). Figure 4.23 (b) shows a comparison of the Fourier transform of the signals measured in a plate free from corrosion (black line) and a plate with a severe accelerated corrosion patch between the transducers (grey line). At 2 MHz the amplitude of the Fourier transform of the signal propagating through the corrosion patch is 35 dB below the signal recorded in a defect free plate. This level of attenuation over a corrosion patch of 130 mm corresponds to approximately 270 dB/m, so propagation over 1 m would not be feasible.

The interaction of the incoming guided wave modes with corrosion creates mode conversion and scattering leading to an overall attenuation of the transmitted signal. The attenuation of the transmitted signal is a function of multiple parameters i.e. length and severity of the corrosion patch as well as the properties of the guided wave modes. Amongst other parameters, the attenuation of guided waves in the corrosion patch largely depends on the wavelength of the incoming modes. In general it is desirable to use long wavelength or low frequency to reduce the effect of attenuation due to corrosion or surface roughness [58]. For this application the wavelength cannot be increased as the ray theory would become invalid and the validity of the ray is required for the successful implementation of this technique. Consequently the attenuation of the SH modes around 2 MHz due to severe corrosion is too high

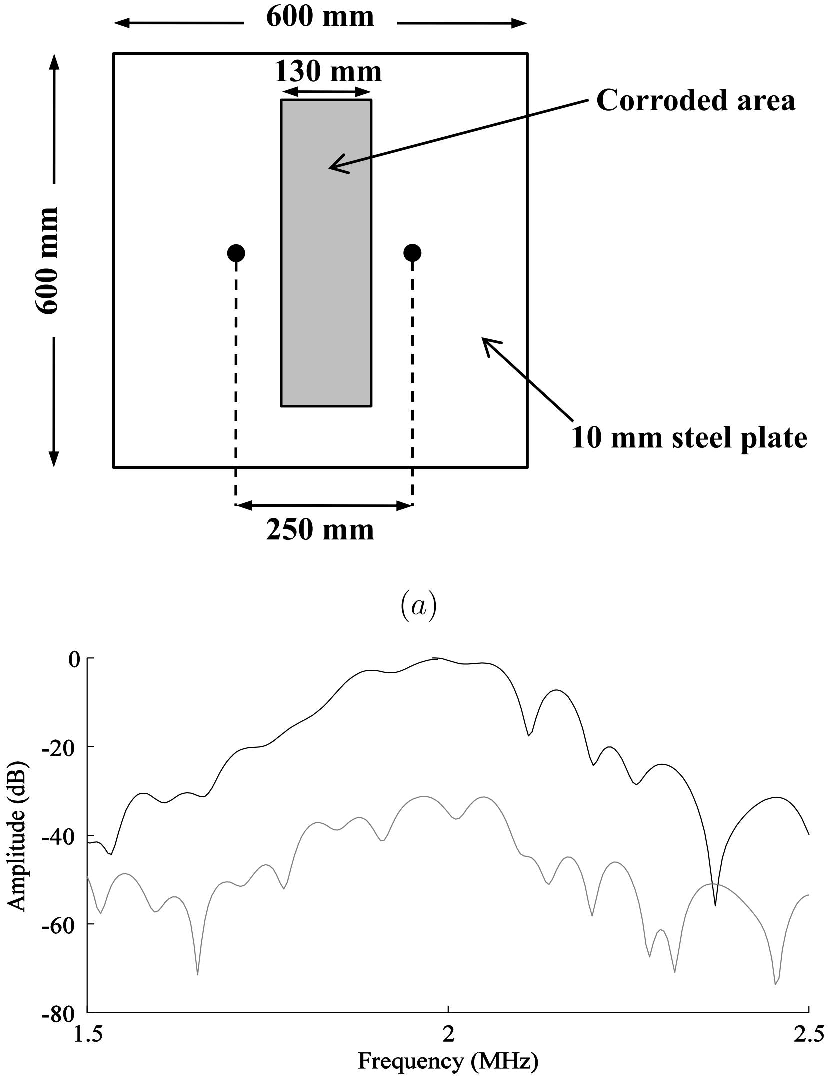

(*a*)

(*b*)

Figure 4.23: *(a) Schematic of the measurement through a corroded area (b) Comparison of the Fourier transform of the signals measured in a plate free from corrosion (black line) and a plate with an actual corrosion patch between the transducers (grey line).*

to be of practical interest. The amplitude of the signal at a sensor array on the other side of a corrosion patch would be severely attenuated if the required propagation distance is of the order of 1 m and therefore this approach was abandoned.

4.5 Summary

Fundamentally the presence of corrosion is simply a change in the waveguide thickness. A guided wave mode will only propagate through a thickness reduction if at the minimum thickness the corresponding frequency thickness product is above the cutoff frequency thickness product of this mode. Therefore by exciting multiple guided wave modes with a source it may be possible to get an approximation of the minimum thickness along the propagation path if the modes that propagated through the reduced thickness area are identified. A novel approach using the validity of the ray theory to select the frequency of excitation was proposed. The investigation was carried at a frequency of 2 MHz in a 10 mm aluminium plate. This frequency was chosen based on the validity of the ray theory to detect a 60 mm diameter defect over a propagation distance of 1 m. The validity of the ray theory ensures that the signal is detected by a sensor without superposition from the interaction of the waves with features outside of the ray path.

2D plane strain FE simulations have shown that it is possible to use SH waves around 2 MHz with two 16 element arrays for excitation and detection of the signals to obtain an estimation of the minimum remaining thickness in the path between the two arrays. The guided wave modes are identified by performing a 2D Fourier transform of the data received by the sensor array.

The experimental results obtained on 30% and 50% machined defects gave results that were significantly different from the FE predictions. In the experimental results, in contrast with the FE predictions, the amplitude of the clusters relative to the maximum amplitude of the 2D Fourier transform does not appear to be related to the remnant thickness between the two transducers. One likely reason for this is that the ray theory approximation may not be valid in this case because the length of the signals recorded is too long. Therefore the slowest excited modes superpose with the interaction of the fastest excited modes and features outside of the ray path e.g. other defects or plate boundaries. Moreover the integrated amplitude of the cluster relative to the no defect case was not consistent with the depth of the defect. This is potentially due to the difference in surface roughness of the 2 defects studied. More importantly it was shown that virtually no energy propagated through a 50% deep accelerated corrosion patch at 2 MHz. Therefore the attenuation of SH waves around 2 MHz due to severe corrosion is too high to be of practical interest if the required propagation distance is of the order of 1 m and this approach was abandoned.

Chapter 5

Guided Wave Diffraction Tomography

5.1 Introduction

Time-of-flight tomography is based on straight ray propagation, thus ignoring diffraction effects. Chapter 3 demonstrated that the ray theory is not valid when using low frequency guided waves to detect and size defects of the dimension of interest in this project: 60 mm diameter over a propagation distance of approximately 1 m. Straight ray tomography and diffraction tomography are equivalent when the wavelength approaches zero [21]. In contrast with the time-of-flight straight ray tomography algorithms which reconstruct the thickness from time-of-flight projections, the input to a diffraction tomography algorithm is the wave field scattered by the defects to be imaged. In order to perform a diffraction tomography reconstruction, an approximation of the wave equation must be used with the incident and total fields. The incident field corresponds to the wave field when the structure has no defect whereas the total field is the superposition of the incident and scattered fields. Obtaining the incident field on structures that have been in service for many years can be challenging. Rohde et al [38] recently examined diffraction tomographic imaging of flexural inhomogeneities i.e. change in thickness, density, Young's modulus or shear modulus in plates within the Born approximation (see chapter 2) for structural health monitoring applications. Using a structural health monitoring approach greatly simplifies the implementation of diffraction tomography because it implies that baseline measurement can be used as the incident field in the evaluation of the scattered field. That paper presented simulation results for a single defect within the area of inspection. A simulated incident field was used in the evaluation of the Born approximation. Parallel linear arrays of sources and sensors were revolved around the area of inspection to obtain the data required for the reconstruction.

This chapter considers the practical implementation of low frequency guided wave diffraction tomography for the reconstruction of thickness in a plate containing multiple thickness reductions using a circular array of transducers. The reconstruction is based on the scattering due to the change in velocity of a guided wave mode during propagation through thickness changes. This chapter describes two different possibilities to deal with the incident field subtraction of the Born approximation: the so-called structural health monitoring approach and a novel approach which does not require the incident field subtraction. In this chapter the first section explains the theory of diffraction tomography based on scattering due to velocity change and its main difference compared to straight ray tomography. The second section discusses details of the FE simulations and thickness reconstruction with multiple defects in the area of inspection. In the third section the challenges of the experimental implementation of guided wave diffraction tomography are examined. The results presented in this chapter were recently submitted for publication in IEEE Transactions on Ultrasonics, Ferroelectrics and Frequency Control (P5 in the list of publications).

5.2 Theory

The principle of diffraction tomography is very different from the more conventional straight-ray tomography approach. Schematics of the principle of diffraction and

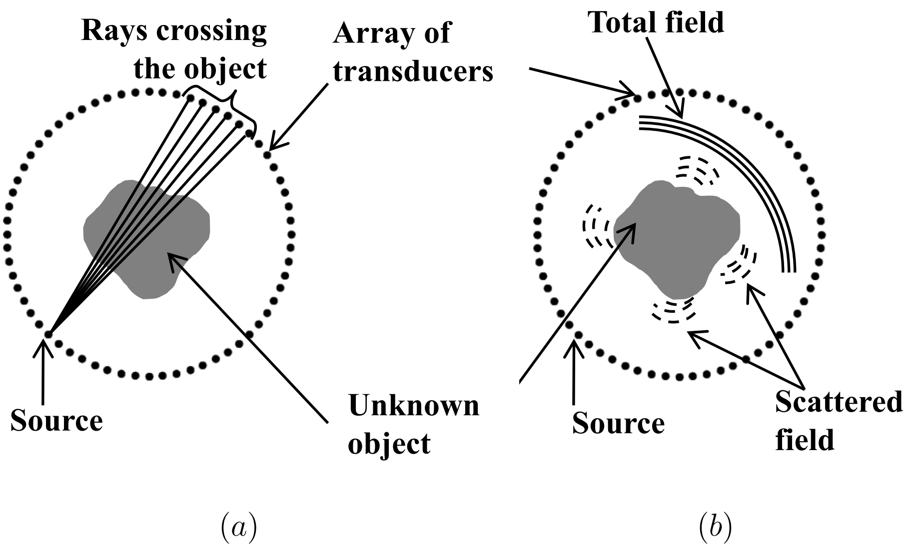

Figure 5.1: *(a) A source excites a wave field that propagates in straight lines across the unknown object. The array of transducers receives the projection of a parameter that corresponds to line integrals along the rays. (b) A source excites an incident wave field that interacts with an unknown object to produce a scattered field. The superposition of the scattered and incident fields, the so-called total field, is received at the array of transducers.*

straight-ray tomography are presented in figure 5.1 in the case of a circular array of transducers.

In straight-ray tomography (figure 5.1 (a)) the waves are assumed to travel in straight lines between a source and the sensors. At the sensors a parameter that can be represented by a line integral along the propagation ray is evaluated. The most common parameters for straight-ray tomography are the time-of-flight and the attenuation. An array of transducers measures the changes in the value of the parameter due to the presence of an unknown object. By backprojecting the parameter detected at the array it is possible to reconstruct the object, subject to the validity of the ray theory. Straight-ray tomography implies that the ray theory is valid. The ray approximation is respected when the size of the object to be imaged is much larger than the wavelength and much larger than the width of the first Fresnel zone [46]; this is thus a high frequency approximation.

When the ray theory is not valid, diffraction effects become dominant and one must use wave propagation theory rather than the straight-ray approximation to

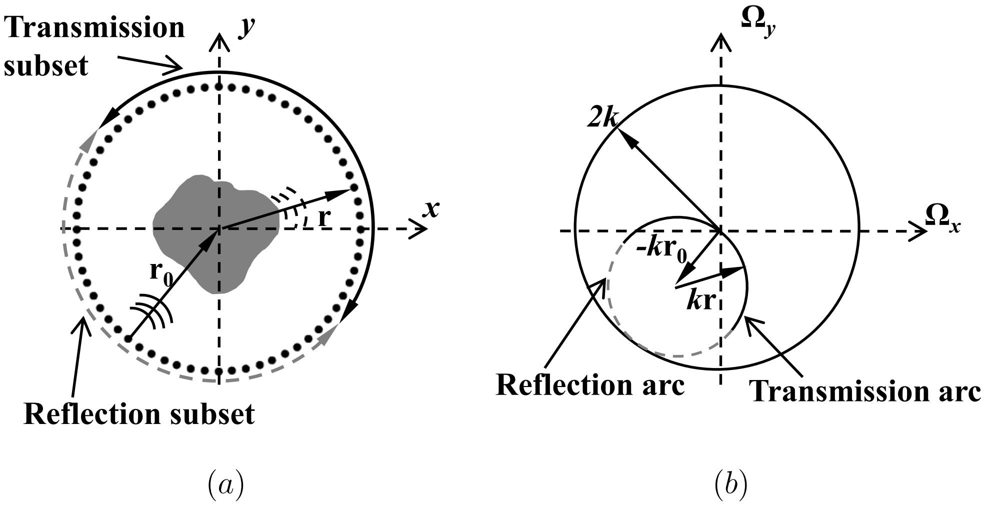

Figure 5.2: *(a) A circular array that can illuminate an unknown object from all directions* $\mathbf{r_0}$ *and detect the scattered field from any direction* $\mathbf{r}$*.* $\mathbf{r_0}$ *and* $\mathbf{r}$ *can only take discrete values which correspond to the locations of the transducers. (b) Two-dimensional K space showing the mapping of the scattered field measured in direction* $\mathbf{r}$ *from an incident direction* $\mathbf{r_0}$*. The solid semicircular arc corresponds to all directions* $\mathbf{r}$ *in transmission and the dashed semicircular arc corresponds to those in reflection from an incident direction* $\mathbf{r_0}$*.*

achieve the reconstruction. The majority of the diffraction tomography algorithms were developed in ultrasonic medical and geophysical imaging where the purpose is to reconstruct objects with different propagation velocity in comparison with the background medium. These objects are reconstructed from the phase and amplitude of the scattered field. The scattered field (figure 5.1 (b)) corresponds to the field generated by the objects when illuminated by an incident field. In a typical measurement the array of transducers measures the total field: the superposition of the incident and scattered fields. In order to perform a diffraction tomography reconstruction, an approximation of the wave equation must be used to generate the data necessary for the reconstruction. The Born and the Rytov approximations (see chapter 2) are the most common. These two approximations will be examined for guided wave diffraction tomography with FE simulations in the next section.

The processing of the scattered field is carried out in the spatial frequency domain. Figure 5.2 shows how the scattered field measured with the array maps in the spatial frequency domain. In figure 5.2 (a) a circular array is illuminating an unknown object from a direction $\mathbf{r}_0$ and the scattered field is detected in direction $\mathbf{r}$. The array can excite and detect at a discrete number of directions which corresponds to the number of transducers in the array. The scattered field measured in direction $\mathbf{r}$ maps in the K space at $k(\mathbf{r}-\mathbf{r}_0)$, where k is the wavenumber at the frequency of interest. As the position of the source rotates around the array, a disk in the K space with a radius $2k$ is populated. This disk is known as the Ewald limiting disk [59]. For any source in the array the sensors can be divided into two subsets: the transmission and reflection subsets. The scattered field measured by the transmission subset maps in the K space on the transmission arc and the reflection subset maps on the reflection arc. For any direction $\mathbf{r}_0$ the transmission subset is contained within a circle of radius $\sqrt{2}k$ in the K space and the reflection subset is contained between $\sqrt{2}k$ and $2k$ [60]. Therefore the transmission subset contains the lower spatial frequencies and the reflection subset the higher spatial frequencies.

The purpose of this chapter is to investigate the possibility of using low frequency guided waves for thickness reconstruction in plates and pipes with defect size of the order of 60 mm and propagation distance of the order of 1 m. It has been demonstrated in chapter 3 that the ray theory in such a case is not valid and consequently it is not possible to use the straight-ray tomography algorithms. As mentioned earlier, most of the diffraction tomography algorithms are used to produce a map of the velocity of a given area. Therefore in order to use diffraction tomography for thickness reconstruction with guided waves the velocity of propagation of the guided wave mode of interest must vary with the thickness. Once the map of velocity is obtained, it is easily converted into a thickness map by using the dispersion curves of the guided wave mode of interest. If the point of operation, guided wave mode and frequency, is carefully selected, it is possible to have velocity dependence on the thickness. Figure 5.3 presents the low frequency phase velocity dispersion curves in an aluminium plate. The vertical dashed line corresponds to the maximum frequency if one wants to avoid contamination from the higher order modes. Above this frequency the signal processing becomes much more complex due to the presence of multiple guided wave modes. The selection of the point of operation has already been detailed in chapter 3 and is only briefly covered here. Below 2 MHz.mm there

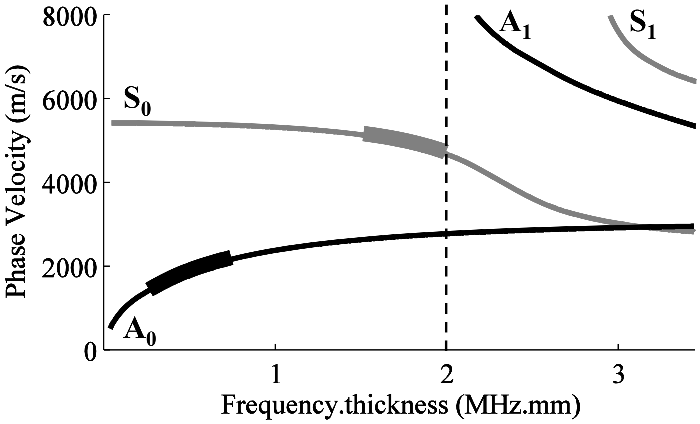

Figure 5.3: *Phase velocity dispersion curves in an aluminium plate. The vertical dashed line corresponds to the maximum frequency if one wants to avoid contamination from the higher order modes.*

are two likely points of operation: A_0 around 0.5 MHz.mm and S_0 around 1.75 MHz.mm. When A_0 at 0.5 MHz.mm is used the phase velocity decreases in a thickness reduction. On the other hand, due to the shape of the dispersion curve for S_0 at 1.75 MHz.mm, the phase velocity increases in a thickness reduction. The rest of this chapter will use only A_0 as an example because experimentally the transduction is easier; however all the conclusions apply to S_0 at 1.75 MHz.mm as well. The frequency-thickness products of the points of operation were quoted for aluminium. However it is possible to use the same guided wave mode in steel or other materials at slightly different frequency-thickness product, such that results presented here would apply.

The algorithm used in this chapter assumes that the scattered field was generated by an unknown object with a propagation velocity different from the background medium. All other properties of the unknown object are the same as the background medium. This is not strictly true for thickness reconstruction with guided waves. The local stiffness and local mass are lower in the reduced thickness area but more importantly part of the energy of the incident wave field will convert into other guided wave modes at the defect boundary. The severity of the reflection and mode conversion depends on the thickness profile of the defect; a smooth variation of the thickness in comparison with the wavelength tends to reduce the amplitude of mode conversion [7]. In this study the scattered field from the change in stiffness and mass as well as the mode conversion are not taken into account and will be shown to have little influence on the reconstruction at the selected point of operation. Simonetti and Huang [61] demonstrated, for a circular array, the existence of a linear mapping between beamforming and diffraction tomography which is represented by a linear filter in the spatial frequency domain. The beamforming image is produced by phase shifting and integrating over the aperture of the array the data set obtained with an approximation of the wave equation for all the points (x, y) in the image space. The focusing process allows the contribution to the scattered field of a given point (x, y) to be separated from all the other points in the image space. The combination of focusing in transmission and reception leads to the beamforming image at $\mathbf{z} = (x, y)$

$$i_{BF}(\mathbf{z}) = \langle g_{\mathbf{z}} | T_{\infty} | g_{\mathbf{z}} \rangle, \tag{5.1}$$

where $|g_{\mathbf{z}}\rangle$ is the steering function of the incident beam at the point $\mathbf{z} = (x, y)$ which can be expressed as

$$|g_{\mathbf{z}}\rangle = \exp(-ik\mathbf{r_0} \cdot \mathbf{z}) \tag{5.2}$$

where $\mathbf{r_0}$ is the direction of propagation of the incident plane wave. T_{∞} is the far field pattern of the scattered field due to a linear combination of incident plane waves. As the far field operator T_{∞} is a singular system it is possible to write [61]

$$T_{\infty} = \sum_{n=-\infty}^{\infty} \mu_n |\phi^n\rangle\langle\nu^n|, \tag{5.3}$$

then

$$i_{BF}(\mathbf{z}) = \sum_{n=-\infty}^{\infty} \mu_n \langle g_{\mathbf{z}} | \phi^n \rangle \langle \nu^n | g_{\mathbf{z}} \rangle. \tag{5.4}$$

Once the beamforming image is obtained, it is filtered to obtain the diffraction tomography reconstruction. The filter can be expressed as

$$H_{BP}(\Omega) = G(\Omega) H_{DT}(\Omega) \tag{5.5}$$

where H_{BP} is the 2D Fourier transform of the point spread function associated with beamforming, H_{DT} is the 2D Fourier transform of the point spread function associated with the diffraction tomography image and

$$G(\Omega) = \frac{8\pi^2\Pi}{k|\Omega|\sqrt{1 - |\Omega|^2/4k^2}} \tag{5.6}$$

with

$$\Pi = \frac{\exp(i\pi/4)}{\sqrt{8\pi k}}. \tag{5.7}$$

$G(\Omega)$ is the filter which directly links the point spread function of beamforming to that of diffraction tomography. G diverges for $|\Omega| = 0$ and $|\Omega| = 2k$ giving maximum weight to the low spatial frequencies of the object and to a lesser extent the high spatial frequencies close to $2k$ in the beamforming image. A beamforming image is thus a distorted version of the diffraction tomography image. If $I_{BF}(\Omega)$ is the 2D Fourier transform of the beamforming image then the 2D Fourier transform of the diffraction tomography image ($I_{DT}(\Omega)$) is obtained with

$$I_{DT}(\Omega) = \frac{I_{BF}(\Omega)}{G(\Omega)} \times C \tag{5.8}$$

where C is a calibration factor used to obtain the correct thickness in the diffraction tomography reconstruction. This factor relates the amplitude of the scattered field to the thickness in the reconstruction. In this study the calibration factor is obtained by calculating the factor C required to reconstruct the correct thickness at a defect in the first finite element simulation presented in the next section.

The diffraction tomography algorithm used in this chapter is a two stage algorithm where a beamforming image is produced in the first stage and is then filtered to give the same weight to all spatial frequencies and produce a diffraction tomography image in the second stage.

The performance of this diffraction tomography algorithm for guided wave thickness reconstruction is evaluated with FE simulations in the next section.

5.3 Finite Element Simulations

5.3.1 Comparison of the Born and Rytov Approximations

The two most common approximations of the wave equation are the Born and Rytov approximations. The data generated with the Born or Rytov approximation can be used with the diffraction tomography algorithm described in section 5.2. These approximations can be expressed as

$$
\begin{aligned}
\text{Born: } U_a &= U_t - U_i \\
\text{Rytov: } U_a &= U_i \log\left(\frac{U_t}{U_i}\right)
\end{aligned}
\tag{5.9}
$$

where U_a is the data for the diffraction tomography algorithm when using either the Born or the Rytov approximation, U_t is the total field and U_i is the incident field.

The implementation of the Born approximation is very simple; the estimated scattered field is obtained by subtracting the incident field from the total field. The Rytov approximation is, however, more complex to implement because a complex logarithm needs to be evaluated and thus the phase of U_t and U_i needs to be unwrapped. It is relatively straightforward to unwrap the phase on simulated data, but errors are easily introduced when using experimental data giving errors in the resulting scattered field.

As explained in chapter 2, the two approximations have quite different validity criteria. For the Born approximation the phase difference between the incident field and the wave propagating through the unknown object must be less than π. Consequently this approximation is only valid for small or low contrast objects, the contrast being defined as the difference between the background medium velocity and the velocity in the unknown object. For the Rytov approximation it is the change in the scattered phase over a wavelength that is important and not the total phase change.

In order to compare the Born and Rytov approximations an acoustic FE model was

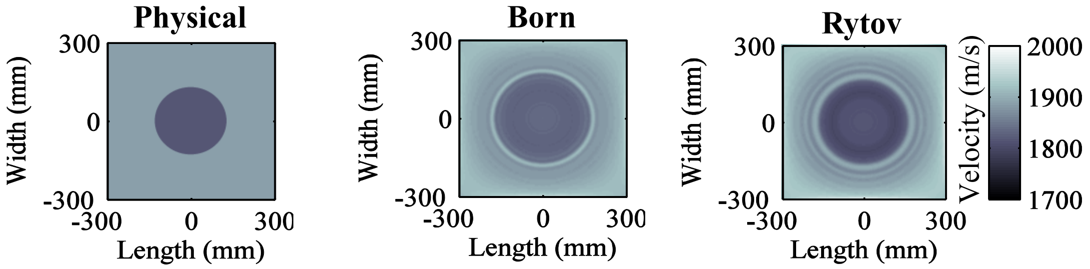

(*a*) (*b*) (*c*)

Figure 5.4: *Comparison of the diffraction tomography reconstruction between the Born and the Rytov approximation. The diameter of the inhomogeneity is 380 mm. The velocity in the inhomogeneity is 1816 m/s and the background medium velocity is 1886 m/s. (a) theoretical map, (b) diffraction tomography reconstruction with the Born data set and (c) diffraction tomography reconstruction with the Rytov data set.*

designed in Abaqus. Using the acoustic model for this comparison provides two major advantages. In contrast with an elastic FE model, only compressional waves can propagate in the acoustic model and there is therefore no mode conversion. The bulk modulus of the acoustic medium was chosen such that the velocity of propagation of the compressional wave in the acoustic medium corresponded to the phase velocity of A_0 at 50 kHz in a 10 mm aluminium plate. A 2D plane stress model was used with 32 square-shaped elements per wavelength. Absorbing boundaries were added to the model to avoid reflections from the edges. A circular array of 128 source/sensor nodes with diameter 800 mm was used to generate the data required to assess the performance of the Born and Rytov approximations.

An unknown object was introduced within the array of source/sensor nodes in the form of a velocity inhomogeneity. The inhomogeneity simply corresponds to a change in the velocity of propagation of the compressional wave which was obtained by modifying the bulk modulus of a subset of elements. The following examples are used to compare the Born and Rytov approximations for a large velocity inhomogeneity. Figure 5.4 presents a comparison of the diffraction tomography reconstruction between the Born and the Rytov approximations for a single inhomogeneity in the centre of the array. The diameter of the inhomogeneity is 380 mm. A large inhomogeneity is used to demonstrate the limit of the validity of the Born approximation.

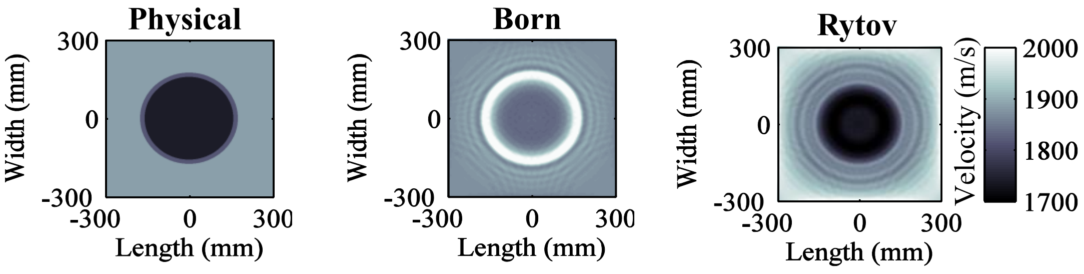

(*a*) (*b*) (*c*)

Figure 5.5: *Comparison of the diffraction tomography reconstruction between the Born and the Rytov approximation. The diameter of the inhomogeneity is 380 mm. The velocity in the inhomogeneity is 1738 m/s and the background medium velocity is 1886 m/s. (a) theoretical map, (b) diffraction tomography reconstruction with the Born data set and (c) diffraction tomography reconstruction with the Rytov data set.*

The velocity in the inhomogeneity is 1816 m/s and the background medium velocity is 1886 m/s. This difference in velocity corresponds to a 10% defect in a 10 mm aluminium plate at 50 kHz with the A_0 mode. The theoretical map is presented in (a), the diffraction tomography reconstruction with the Born data set in (b) and the diffraction tomography reconstruction with the Rytov data set in (c). As there is only a single inhomogeneity within the array, the phase is easily unwrapped for the implementation of the Rytov approximation. In this case the reconstructions using the Born and Rytov approximations are very similar. The shape and contrast of the inhomogeneity is well reconstructed and is close to the theoretical map. Figure 5.5 presents the same comparison but this time the contrast is increased. The velocity in the inhomogeneity is 1738 m/s and the background medium velocity is again 1886 m/s. This difference in velocity corresponds to a 20% defect in a 10 mm aluminium plate at 50 kHz with the A_0 mode. The theoretical map is presented in (a), the diffraction tomography reconstruction with the Born data set in (b) and the diffraction tomography reconstruction with the Rytov data set in (c). In this case the reconstructions using the Born and Rytov approximation are rather different. The reconstructed velocity at the centre of the Born reconstruction is far from the real velocity. On the other hand the Rytov reconstruction is again very accurate in shape and contrast. In this case the phase change through the inhomogeneity

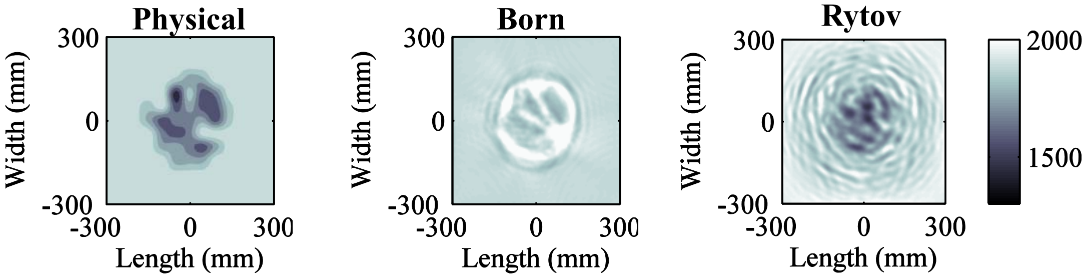

(*a*) (*b*) (*c*)

Figure 5.6: *Comparison of the diffraction tomography reconstruction between the Born and the Rytov approximation. The diameter of the inhomogeneity is 380 mm. The velocity in the inhomogeneity is varying randomly and the minimum is 1440 m/s and the background medium velocity is 1886 m/s. (a) theoretical map, (b) diffraction tomography reconstruction with the Born data set and (c) diffraction tomography reconstruction with the Rytov data set.*

is too large such that the scattering mechanism cannot be represented accurately with the Born approximation. Figure 5.6 presents a comparison of the Born and Rytov approximation when the velocity in the inhomogeneity is varying randomly. Neither of the reconstructions is accurate in this case. The Born reconstruction is not accurate because the phase change through the object is too large and the therefore the scattering mechanism cannot be represented by the Born approximation. The problem for the Rytov reconstruction is that in this case the phase is very difficult to unwrap because the inhomogeneity is much more complex than a single defect. However if the phase was perfectly unwrapped, the reconstruction would be accurate. Although the Rytov approximation is valid over a wider range of objects the difficulties in its practical implementation ultimately made us chose the Born approximation for this initial study. Therefore all the cases studied in this chapter were designed to be within the validity of the Born approximation. The next subsection describes the FE model to simulate guided wave interaction with thickness reductions.

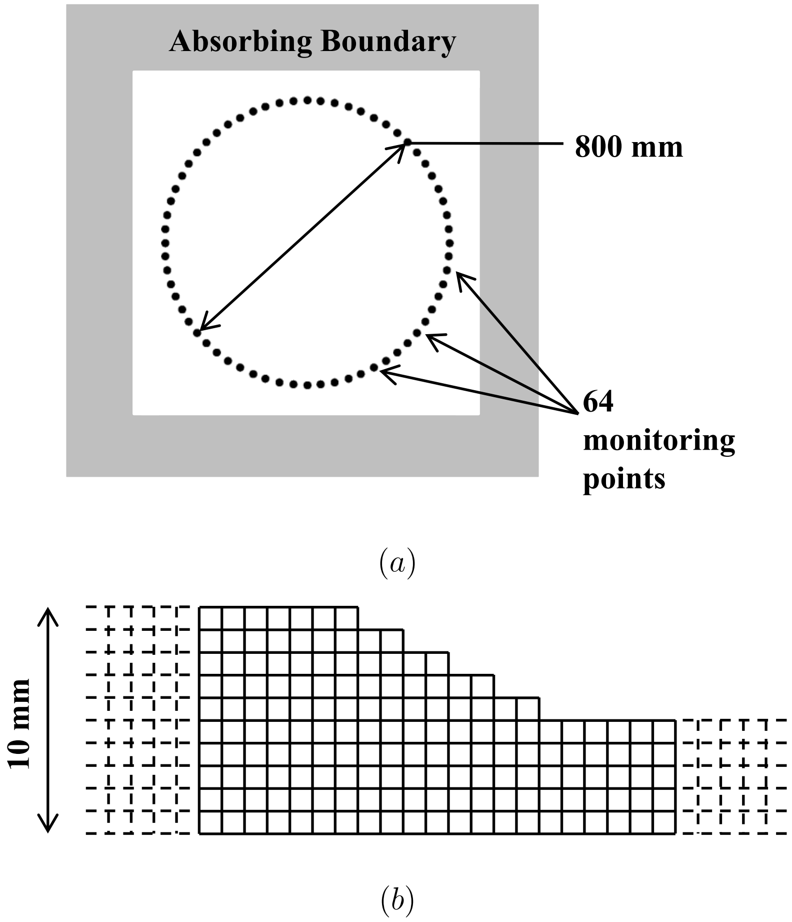

Figure 5.7: *Schematic of the FE model, (a) plan view and (b) detail of defect.*

5.3.2 Finite Element Model

In order to investigate the performance of diffraction tomography for thickness reconstruction with guided waves a FE model was designed in Abaqus. The FE modeling was carried out on a plate (a schematic of the FE model is presented in figure 5.7 (a)); the simulations are also valid for large diameter pipes as the effect of curvature becomes negligible [8].

The FE model consisted of a 10mm plate with a circular array of 64 exciting/monitoring points across a diameter of 800 mm. Thickness reductions were then introduced at various locations within the array. The material was aluminium (E = 70.8 GPa, ν = 0.34 and ρ = 2700 kg/m^3), there were 10 cubic-shaped 3D linear brick elements in the thickness and the input signal was a 5 cycle Hanning windowed toneburst centered at 50 kHz. Actual corrosion patches are not like flat-bottomed holes so stepped boundaries are a better representation. Hence in order to model more realistic corrosion patches the elements in the thickness were used to model the part-through defect edges in steps as shown in figure 5.7 (b). Absorbing boundaries [49, 50] were used to remove the reflections from the edges of the plate, so simulating an infinite plate. For a given excitation location an out of plane force excited the A_0 guided wave mode and the out of plane displacement was detected at the 63 other monitoring points. Using an out of plane point force at 50 kHz ensured that the ratio of surface displacement of A_0 to S_0 at the excitation was approximately 40 dB, see chapter 3. Moreover by detecting only the out of plane displacement at the monitoring points the A_0 mode was detected with an amplitude 40 dB higher than S_0 and consequently was almost insensitive to mode conversion.

The FE model was run both with and without defects, the case without defects being used as the incident field in the evaluation of the scattered field. The Born data set was then processed by the diffraction tomography algorithm.

5.3.3 Finite Element Results

Figure 5.8 presents a monochromatic diffraction tomography reconstruction of the thickness in a plate with a single defect in the centre of the array at 50 kHz. This first simulation was used to calculate the calibration factor C of equation 5.8 and therefore the depth of the defect corresponds exactly to the theoretical profile. The same value of C was used in all the FE simulations. The defect has a diameter of 60 mm, which corresponds to approximately 1.5 λ at 50 kHz and is 50% deep. The map of the reconstructed thickness is free from artefacts and the defect is easily identified in the centre of the map. Figure 5.8 (b) shows the thickness profile across the defect where the black line corresponds to the reconstructed profile and the light grey line corresponds to the theoretical profile. The depth of the reconstructed defect is slightly underestimated at the centre of the defect in comparison with the actual thickness profile, but the location and diameter are very accurate. This reconstruction confirms that assuming that the scattered field is only due to a change

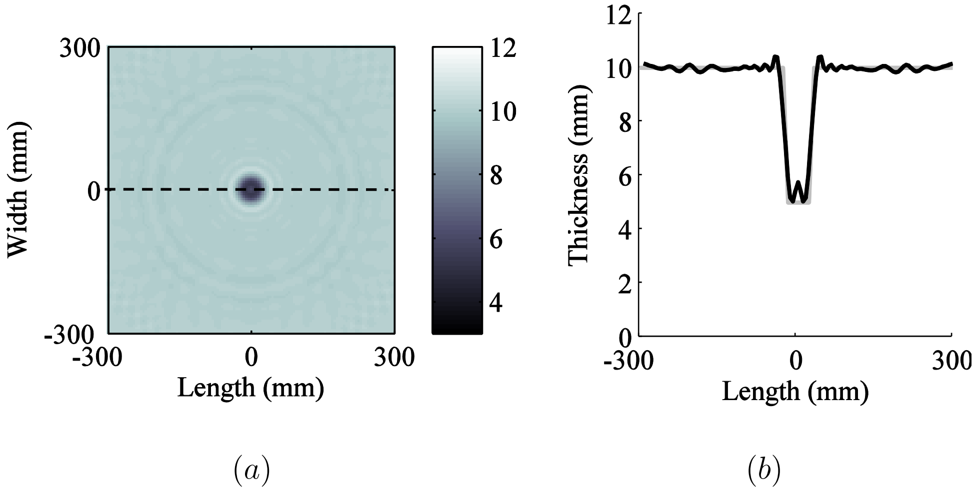

Figure 5.8: *FE monochromatic diffraction tomography reconstruction at 50 kHz with one thickness reduction within the array of transducers. The thickness reduction has a diameter of 60 mm ($\approx 1.5\lambda$ at 50 kHz) and is 50% deep. (a) Map of the reconstructed thickness and (b) thickness profile across the defect. The black line corresponds to the reconstructed thickness profile and the light grey line to the actual thickness profile.*

in velocity is a reasonable assumption in this case, showing that the amplitude reduction of the A_0 mode due to mode conversion is not large enough to affect the reconstructed thickness. Moreover the order of magnitude of the scattered field due to the changes in stiffness and mass is much lower than the component due to the change in velocity.

Figure 5.9 shows a monochromatic diffraction tomography reconstruction of the thickness in a plate with two defects within the array at 50 kHz. The defect in the centre of the array is identical to the one in figure 5.8 and the second defect has a diameter of 100 mm, which corresponds to approximately 2.5 λ at 50 kHz and is 30% deep. In the map of the reconstructed thickness (figure 5.9 (a)) the two defects are once again easily identified. In the thickness profile the depth, diameter and location of both defects are reasonably accurate, with the depth of the shallower defect being slightly overestimated. Apart from the two defects there are two interesting features in the reconstruction.

Firstly multiple scattering between the two defects increased the reconstructed thickness in the area between the two defects on the thickness profile. The scattered field

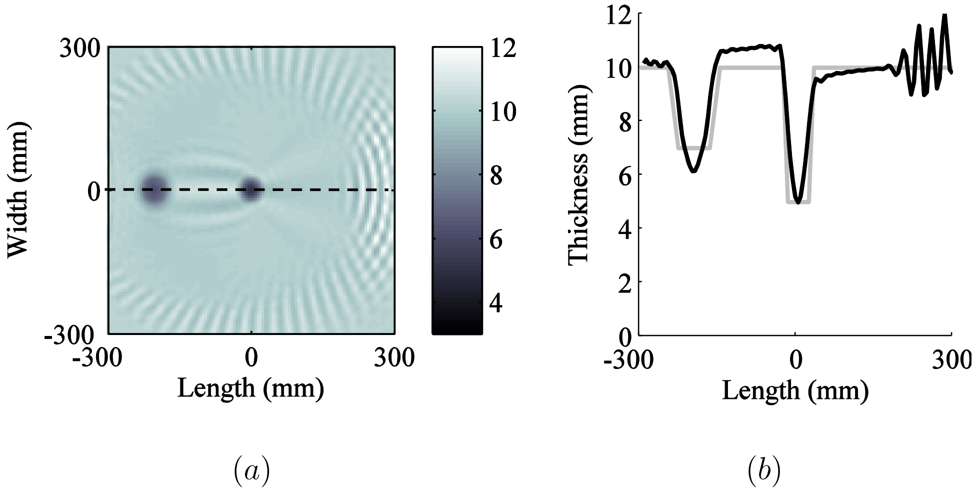

(*a*) (*b*)

Figure 5.9: *FE monochromatic diffraction tomography reconstruction at 50 kHz with two thickness reductions within the array. The added thickness reduction has a diameter of 100 mm (*$\approx 2.5\lambda$ *at 50 kHz) and is 30% deep. The other thickness reduction is identical to the one in figure 5.8. (a) Map of the reconstructed thickness and (b) thickness profile across the defects. The black line corresponds to the reconstructed thickness profile and the light grey line to the actual thickness profile.*

generated by one of the defects interacts with the second defect and this second order scattered field is detected by the array and appears as a modification of the thickness in the area between the two defects. The effect of multiple scattering cannot be removed by adding more transducers in the array and is inherent to the presence of multiple defects. Although multiple scattering contains valuable information about the defects, it is not interpreted in this chapter.

Secondly relatively large amplitude grating lobes appeared to the far right of the length axis of the thickness profile. These grating lobes are due to the undersampling of the wave field in the circular array. Simonetti et al [62] demonstrated that the minimum number of transducers in a circular array in order to correctly sample a wave field of wavelength λ can be expressed as

$$N \geqslant \frac{2\pi D}{\lambda} \tag{5.10}$$

where D is the diameter of the image to be free from grating lobes. This relationship is the circular array equivalent of Shannon's sampling theorem of $\lambda/2$ spacing of the transducers in a linear array. The second defect in figure 5.9 is located just outside

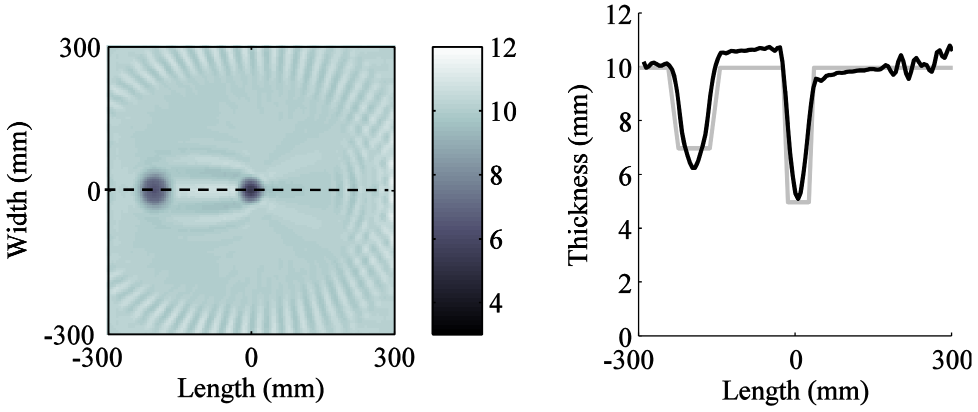

(*a*) (*b*)

Figure 5.10: *FE polychromatic diffraction tomography reconstruction between 45 and 55 kHz with two thickness reductions within the array. The two defects are identical to figure 5.9 (a) Map of the reconstructed thickness and (b) thickness profile across the defects. The black line corresponds to the reconstructed thickness profile and the light grey line to the actual thickness profile.*

of D for $N = 64$, hence the grating lobes in the reconstruction. If the diameter of the array is kept constant, 80 transducers would be required to obtain a reconstruction free from grating lobes. It is however unrealistic to use more than 64 transducers because the spacing between them would become too small and impractical in a field implementation. The location of these grating lobes is frequency dependent so that by averaging multiple monochromatic reconstructions the amplitude of the grating lobes should decrease. Figure 5.10 shows a polychromatic diffraction tomography reconstruction between 45 and 55 kHz with the same parameters as figure 5.9. The polychromatic reconstruction is almost identical to the monochromatic reconstruction but with lower amplitude grating lobes to the far right of the length axis of the thickness profile since, as expected by taking the average of multiple frequencies, their amplitude decreases. The thickness between the two defects is again higher than expected because the multiple scattering between the two defects is not strongly frequency dependent over a narrow range of frequencies. The rest of the chapter will only present polychromatic reconstructions.

Figure 5.11 shows a polychromatic diffraction tomography reconstruction between

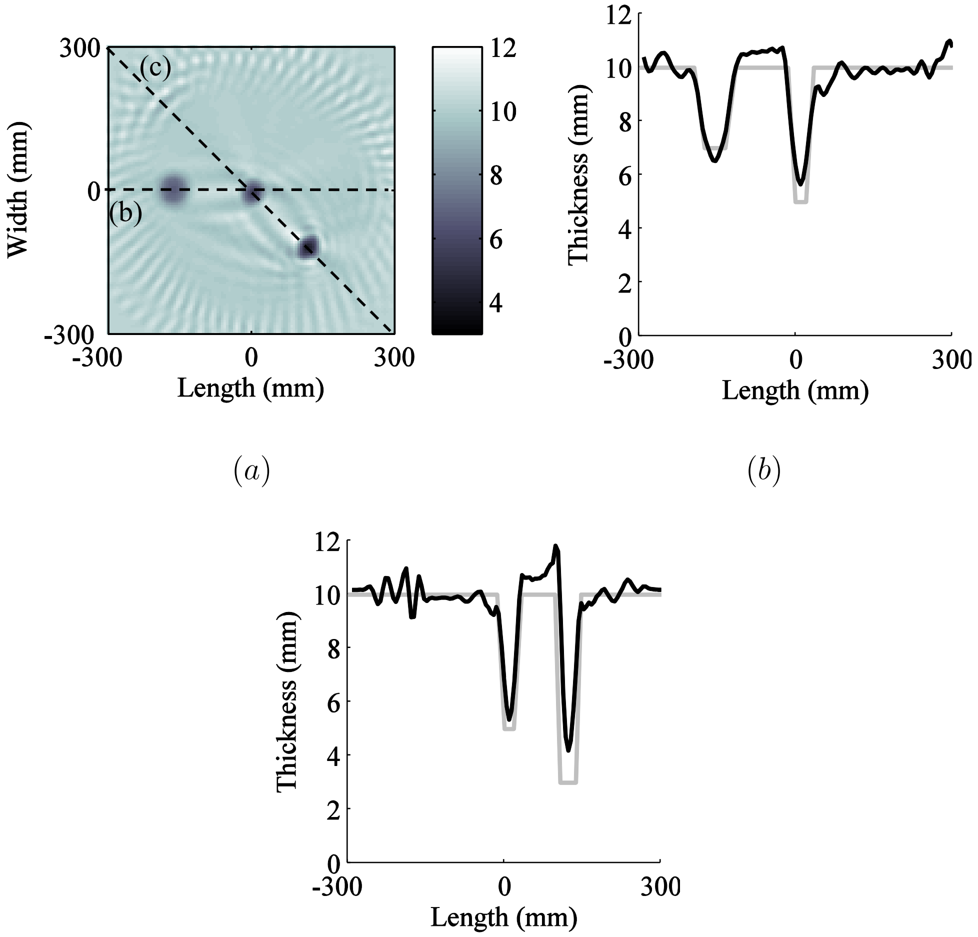

(*a*) (*b*)

(*c*)

Figure 5.11: *FE polychromatic diffraction tomography reconstruction between 45 and 55 kHz with three thickness reductions within the array of transducers. The added thickness reduction has a diameter of 50 mm (*$\approx 1.25\lambda$ *at 50 kHz) and is 70% deep. The other two thickness reductions are identical to the one in figure 5.9 but slightly shifted from their original location. (a) Map of the reconstructed thickness, (b) horizontal thickness profile and (c) diagonal thickness profile. The black line corresponds to the reconstructed thickness profile and the light grey line to the actual thickness profile.*

45 and 55 kHz of the thickness in a plate with three defects within the array. Two of the defects are identical to those in figure 5.11 but at a slightly different location. The defect in the centre was moved by 5 mm in the length direction and by -5 mm in the width direction and the defect on the left hand side was moved by 16 mm in the length direction. The third defect has a diameter of 50 mm, which corresponds

to approximately 1.25 λ at 50 kHz and is 70% deep. Once again the map of the reconstructed thickness is free from large artefacts and the three defects are easily identified. In the two thickness profiles the location and diameter of the three defects is excellent but the depth of the deepest defect is underestimated by a little over 1 mm. As expected from the previous reconstructions multiple scattering and grating lobes are present in the reconstruction.

This section demonstrated that if the thickness reductions within the array respect the Born approximation, a diffraction tomography algorithm can be used to locate and accurately size them. The next section discusses the challenges of experimentally implementing diffraction tomography for thickness reconstruction with guided waves.

5.4 Experiments

5.4.1 Experimental Setup

The experimental setup presented in figure 5.12 (a) comprised a 1200 × 1200 × 10 mm aluminium plate with 64 low frequency A_0 transducers bonded across a diameter 800 mm. The transducers (figure 5.12 (b)) were developed to excite the A_0 mode at low frequency with excellent mode purity. Each transducer has three layers: a thin layer of polyoxymethylene plastic (POM) bonded on the surface of the plate, a piezoceramic element and a brass backing mass. The POM layer and the backing mass are used to decrease the resonance frequency and helps to obtain good transduction at low frequency. The POM layer also has the advantage of decoupling the out-of-plane and in plane displacement of the piezoceramic element and transmitting mainly the out-of-plane displacement to the plate. Further details on the design of these transducers are given in [53] where it is reported that the ratio of A_0 to S_0 is more than 30 dB in the frequency range of interest. The diameter of the transducers is 10 mm which corresponds to approximately $\lambda/4$ for A_0 at 50 kHz and ensures that a point source is a reasonable approximation. For each

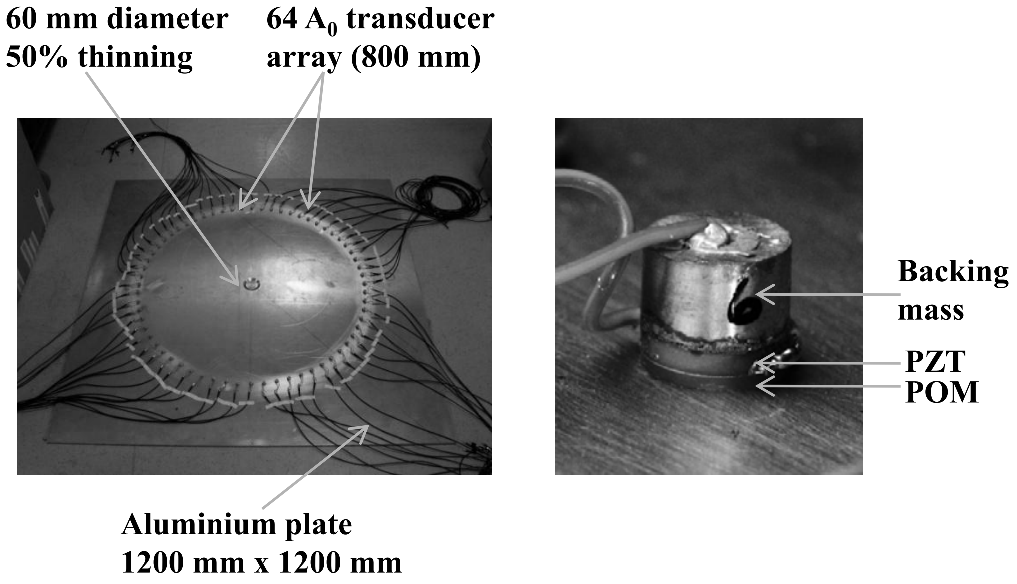

(*a*) (*b*)

Figure 5.12: *(a) Photograph of the experimental setup with a single defect in the centre of array. (b) Zoom on one of the transducer composed of three layers: a backing mass, a piezoceramic element (PZT) and a layer of polyoxymethylene plastic (POM).*

transducer the frequency response function (FRF) between the input signal and the out-of-plane displacement was measured on top of the backing mass with a Polytec laser vibrometer. Although all transducers were assembled and bonded on the plate in exactly the same way, some variability was observed. Figure 5.13 presents (a) the amplitude and (b) the phase of these FRFs between 40 and 60 kHz. At 50 kHz the maximum amplitude difference between the transducers is approximately 15 dB and the maximum phase difference is 30°. These FRFs were used in the experimental reconstruction to compensate for the phase and amplitude difference between each transducer. This is to ensure that each transducer is exciting with the same amplitude and phase. The transducers were bonded on the plate with a position error of approximately ±2 mm. Once the transducers were bonded, their exact location was measured with an accuracy of ±0.5 mm with a laser pointer mounted on a scanning frame. The measured locations were then used in the backpropagation stage of the diffraction tomography algorithm.

Experimentally the plate used was cold rolled and was therefore slightly anisotropic.

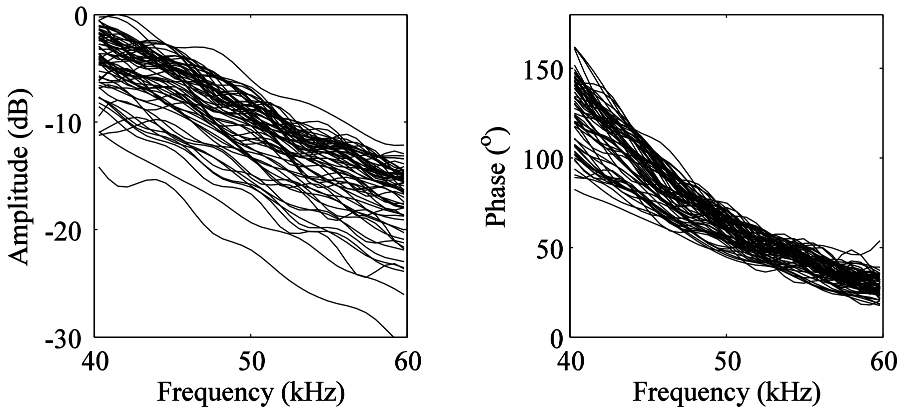

(*a*) (*b*)

Figure 5.13: *Frequency response functions between the input to the transducer and the displacement measured on top of the transducer for the 64 transducers of the array. (a) amplitude normalised to maximum in dB and (b) phase in degrees.*

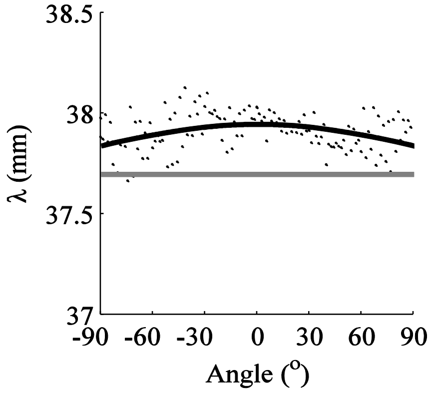

Figure 5.14: *Variation of the wavelength of the* A_0 *mode in the plate as a function of the angle of propagation in degrees. The black line corresponds to a polynomial fit of the wavelength measured (black dots) on the plate and light grey line corresponds to the theoretical value of the wavelength for this type of aluminium (*$E = 70.8$ *GPa,* $\nu = 0.34$ *and* $\rho = 2700$ *kg/m*^{3}*).*

The wavelength was measured as a function of the angle of propagation. The wavelength was obtained by measuring the phase change between two concentric semi circular arcs separated by 50 mm at multiple frequencies between 45 and 55 kHz. Figure 5.14 presents a polynomial fit (black line) of the wavelength at 50 kHz measured experimentally (black dots) as a function of the direction of propagation. The variation of the wavelength as a function of the angle of propagation is approximately

±0.2% compared to the mean value which is 0.5% above the theoretical value for this type of aluminium (E = 70.8 GPa, $\nu = 0.34$ and $\rho = 2700$ kg/m^3). In this study the variation of the wavelength with the angle of propagation was not taken into account but the mean of the measured wavelength was used in the algorithm.

Another major difference between the FE simulations and the experimental implementation is that the reflections from the edges of the plate were removed by using absorbing boundaries around the plate in the simulations. It is, however, difficult to avoid the reflections from the edges experimentally. In this experimental setup the dimensions of the plate were chosen such that the first wave packet to arrive at any transducer in the array does not superpose with the reflections from the edges. During the post-processing of the experimental time traces the signals were gated to remove the reflections from the edges.. The implication of gating the signals is that the scattered field detected by the reflection subset (see figure 5.2) for a given source will not be used in the experimental reconstructions because the reflection from the defect will, in all cases, arrive after the arrival of the reflection from the edges which corresponds to the directly transmitted signal. Consequently, for a given source, only the data detected by the transmission subset will be used in the experimental reconstructions. By using only the transmission subset, the transmission diffraction tomography image produced is a low-pass filtered image with a spatial frequency cutoff of $\sqrt{2}k$ rather than $2k$ in a full diffraction tomography reconstruction. Figure 5.15 presents the FE polychromatic reconstruction between 45 kHz and 55 kHz when only the first wave packet of the transmission subsets of the incident and total fields are used in the reconstruction. The thickness reconstruction is very similar to the one obtained when the full time traces of both the reflections and transmission subsets are used (see figure 5.10); the depth, diameter and location of the defects are again excellent. The only area that was affected by only taking into account the first wave packet of the transmission subsets is between the two defects; this was expected because the multiple scattering between the two defects is likely to arrive after the first arrival and hence was gated out from the time traces. This result indicates that most of the information regarding the defects within the array is contained in the transmission subsets.

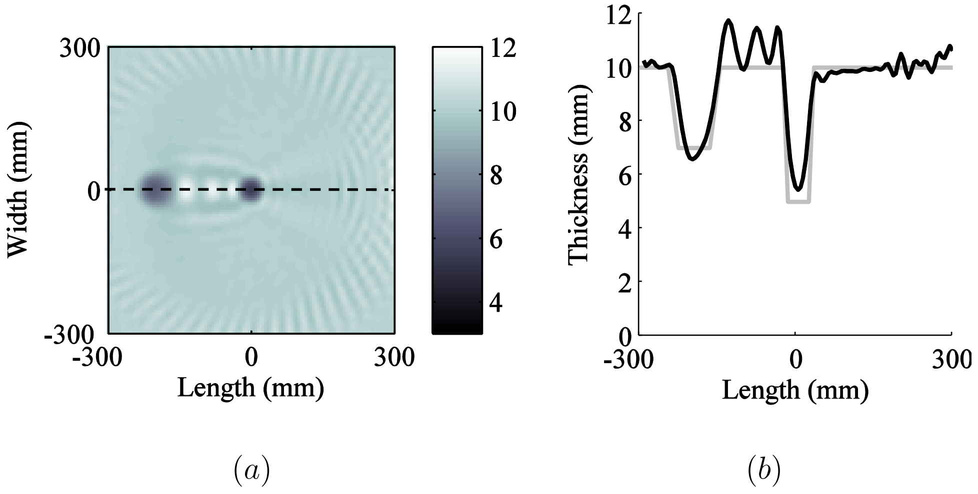

Figure 5.15: *FE polychromatic diffraction tomography reconstruction between 45 and 55 kHz with two thickness reductions within the array and using only the first wave packet to arrive in the transmission subsets. The model is the same as figure 5.10. (a) Map of the reconstructed thickness and (b) thickness profile across the defect. The black line corresponds to the reconstructed thickness profile and the grey line to the actual thickness profile.*

As mentioned earlier, the factor C of equation 5.8 relates the amplitude of the scattered field to the correct thickness in the reconstruction. In FE simulations the factor C was tuned to obtain the correct thickness in a calibration case and then all simulations used the same factor C because the amplitude of excitation was constant. The amplitude of excitation in experiments is different from the one in FE simulations such that a new factor C must be calculated. The experimental factor C_{EXP} is calculated with

$$C_{EXP} = C\frac{A_{FE}}{A_{EXP}} \tag{5.11}$$

where C is the factor obtained from the calibration simulation, A_{FE} is the mean amplitude of the scattering matrix in the calibration simulation and A_{EXP} is the mean amplitude of the scattering matrix in experiments. The scattering matrix contains the scattered field for all source/sensor combinations.

5.4.2 Experimental Implementation

In all the FE results presented in the previous section the incident field was simulated. However obtaining the incident field on structures that have been in service for many years could be difficult. There are consequently two possibilities: omitting the incident field subtraction in the Born approximation or using diffraction tomography in a structural health monitoring approach with transducers permanently installed on the structure. In the latter case the initial measurement would be used as the incident field and the defects would be detected from the difference between the initial measurement and the total field measured at a later time. These two possibilities will be explored in the following subsections.

No Incident Field Subtraction

If it was possible to omit the incident field subtraction in the evaluation of the Born approximation it would be possible to perform a diffraction tomography reconstruction with a single measurement of the total field. Diffraction tomography is a linear transformation that can be expressed, within the Born approximation, as

$$\mathtt{DT}(u_{scattered}) = \mathtt{DT}(u_{total} - u_{incident}) = \mathtt{DT}(u_{total}) - \mathtt{DT}(u_{incident}). \tag{5.12}$$

Figure 5.16 presents the monochromatic diffraction tomography thickness reconstruction of a 10 mm thick uniform plate at 50 kHz obtained when using only the incident field ($\mathtt{DT}(u_{incident})$) (a) when considering the full incident field, i.e. the reflection and transmission subsets (see section 5.2) and (b) when using only the transmission subset. Figure 5.16 (c) and (d) shows the corresponding normalised 2D Fourier transforms.

The thickness reconstruction obtained when using both the reflection and transmission subsets of figure 5.16 (a) contains large amplitude oscillations. The thickness reconstructed using the reflection and transmission subsets of the incident field is very similar to the point spread function of diffraction tomography [63]. The thickness is therefore very high in the centre of the array, several times the plate thickness,

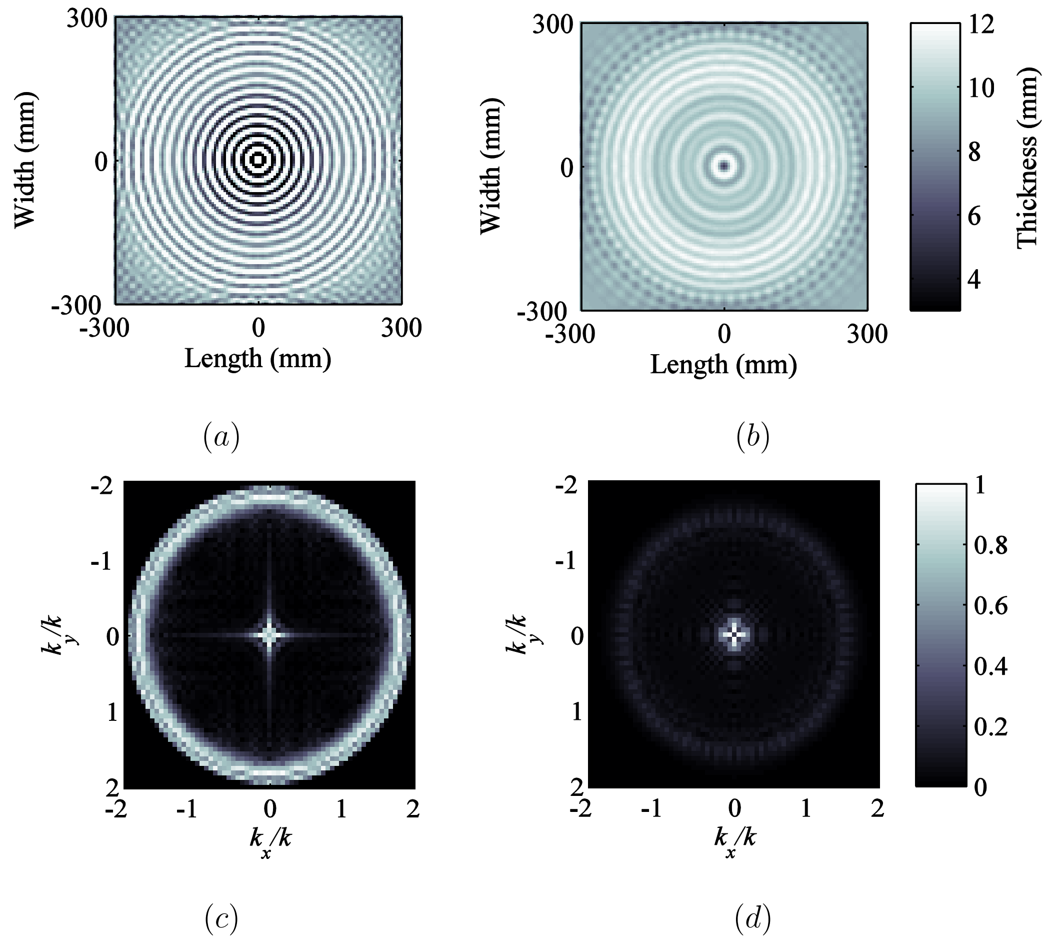

(a) (b)

(c) (d)

Figure 5.16: *Monochromatic diffraction tomography reconstruction of the thickness at 50 kHz in a 10 mm thick uniform plate when using only the incident field (a) when considering the full incident field and (b) when using only the transmission subset. (c) and (d) shows the corresponding normalised 2D Fourier transforms.*

and is heavily clipped in figure 5.16 (a). The amplitude of the oscillations decreases away from the centre of the array. The 2D Fourier transform of this reconstruction shown in figure 5.16 (c) mainly contains spatial frequency components around the origin and between circles of radius $\sqrt{2}k$ and $2k$, where k is the wavenumber at the frequency of interest. By considering only the transmission subset the spatial frequency is limited to $\sqrt{2}k$ as shown in figure 5.16 (d) and the oscillations in the reconstructed thickness are much lower amplitude as shown in figure 5.16 (b). In this case the amplitude range of the oscillations is from 7 mm to 12 mm.

As diffraction tomography is a linear transformation, the incident field subtraction

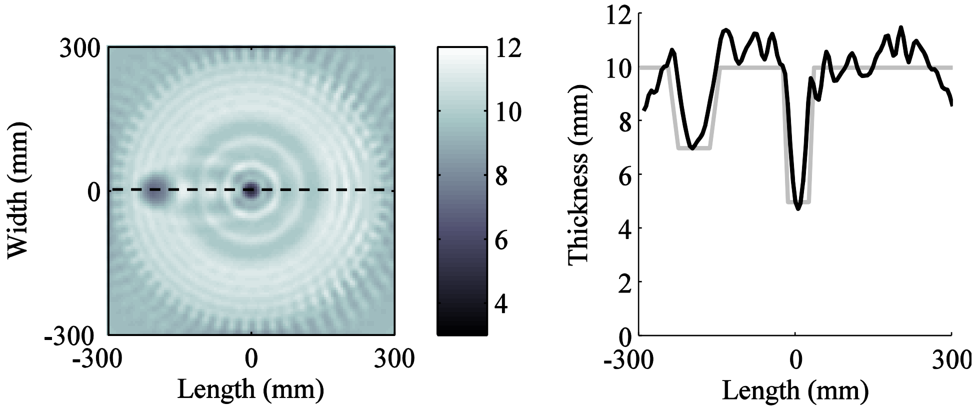

(*a*) (*b*)

Figure 5.17: *FE polychromatic diffraction tomography reconstruction between 45 and 55 kHz with two thickness reductions within the array and using only the transmission data of the total field. The model is the same as figure 5.10. (a) Map of the reconstructed thickness and (b) thickness profile across the defect. The black line corresponds to the reconstructed thickness profile and the grey line to the actual thickness profile.*

is equivalent to subtracting the map shown in figure 5.16 (a) and (b) from the map obtained with the total field. As the variation of the reconstructed thickness when both the reflection and transmission subsets are considered is large, it is not possible to omit the incident field subtraction as it would result in large artefacts in the reconstruction. However when only the transmission subset is considered these oscillations are much smaller amplitude. Consequently when using only transmission data and omitting the incident field subtraction, these oscillations appear as small artefacts in the reconstruction. Therefore by taking only the transmission data an approximation of diffraction tomography within the Born approximation is obtained and the incident field subtraction can be omitted:

$$\mathtt{DT}(u_{total} - u_{incident}) \approx \mathtt{DT}(u_{total}). \tag{5.13}$$

Figure 5.17 presents the FE polychromatic reconstruction between 45 kHz and 55 kHz when only the transmission data of the total field are used in the reconstruction. The number and amplitude of artefacts have increased in comparison with figure 5.10, but the reconstruction is very similar to figure 5.15; the depth and location of both defects are still reasonably accurate. This demonstrates that it is possible to approximate transmission diffraction tomography within the Born approximation by taking only the transmission data of the total field into account in the processing and therefore it is possible to perform a thickness reconstruction from a single measurement of the total field. Experimental results for one and two defect cases will be shown in the results subsection.

Structural Health Monitoring Approach

If the array of transducers is permanently attached to the structure it is possible to use the initial measurement as the incident field in the evaluation of the Born approximation and detect and size the defects that appear thereafter. It is important that the array of transducers remains permanently attached to the structure as if it is removed the location and coupling of the transducers would be modify and it would become impossible to use the measured incident field.

Rohde et al [38] have studied diffraction tomography with a structural health monitoring approach in simulation. In their simulations the incident field was generated from a plate without defects. In the next subsection the structural health monitoring approach is briefly studied with experimental data.

5.4.3 Experimental Results

The following experimental results are separated in two subsections, firstly when the incident field subtraction is omitted and secondly using the structural health monitoring approach.

No Incident Field Subtraction

Figure 5.18 presents an experimental polychromatic reconstruction between 45 kHz and 55 kHz with one thickness reduction in the centre of the array when only the transmission data of the total field is used in the reconstruction, the thickness

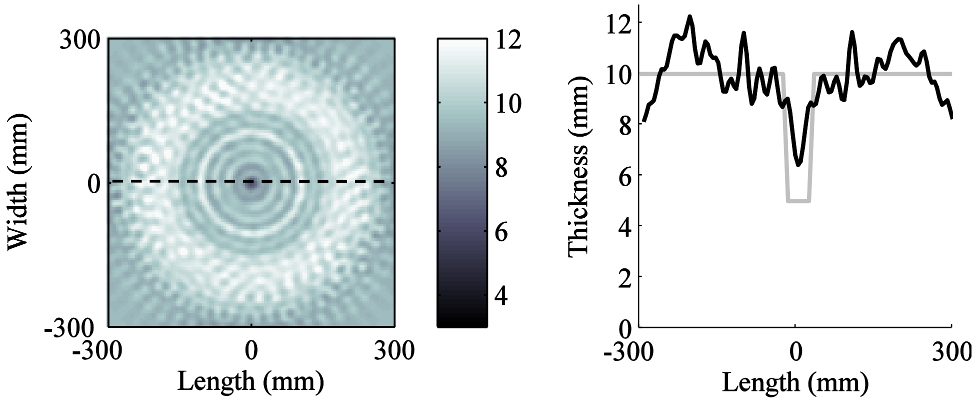

(*a*) (*b*)

Figure 5.18: *Experimental polychromatic diffraction tomography reconstruction between 45 and 55 kHz with one thickness reduction at the centre of the array and using only the transmission data of the total field. The defect has the same properties as figure 5.8. (a) Map of the reconstructed thickness and (b) thickness profile across the defect. The black line corresponds to the reconstructed thickness profile and the grey line to the actual thickness profile.*

reduction having a diameter of 60 mm and 50% deep. The reconstruction is not satisfactory; there are multiple large artefacts with some of them going above 12 mm. Moreover the depth of the thickness reduction is not accurately reconstructed. It was found that the poor reconstruction in this case is due to scattering from the array of transducers. The incident field interacts with each individual transducer and produce a wave field that superposes with the scattered field from the defect to produce large artefacts in the reconstruction.

The wave field scattered by a transducer was measured by scanning an area of a 10 mm aluminium plate with a Polytec laser vibrometer. The technique used to estimate the scattered field required two measurements. A transducer, the source, was bonded on the plate and the wave field it generated was measured. Then a second transducer, the scattering transducer, was bonded 100 mm from the source and the wave field generated by the source was measured again. The difference between these two wave fields corresponds to the wave field scattered by the scattering transducer and is presented in figure 5.19. The wave field scattered by the scattering

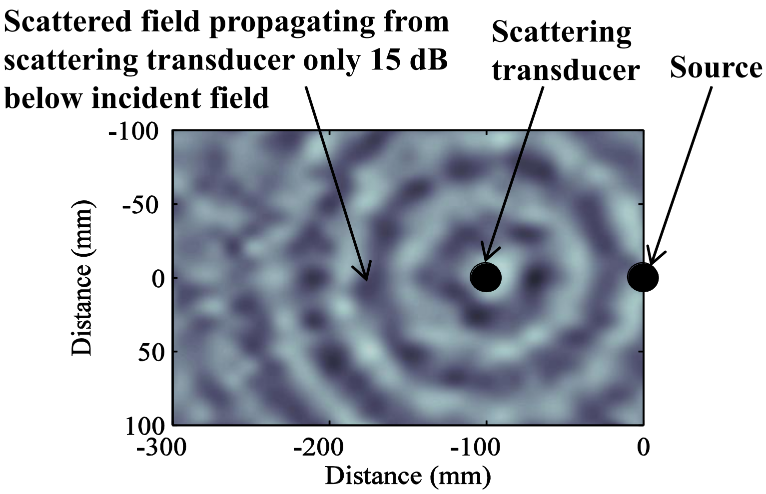

Figure 5.19: *Wave field scattered by a transducer bonded on a 10 mm aluminium plate. The displacement field corresponds to the difference between the displacement field measured with and without the scattering transducer. The wave field scattered by the transducer is only 15 dB below the incident field.*

transducer is only 15 dB below the the wave field generated by the source.

In order to confirm that the large artefacts are due to the scattering of the array of transducers, all but one of the transducers were removed from the plate. When there is a single defect in the centre of the array of transducers the scattered field is the same for all source locations because of symmetry. Hence all the data required can be generated from a single source location and 32 sensor locations, as shown in figure 5.20. The signal at the 32 sensor location was measured with a Polytec laser vibrometer. In this case there is no variation in the coupling of the transducer because all the data is generated from a single source location. Figure 5.21 presents an experimental polychromatic reconstruction between 45 kHz and 55 kHz with one thickness reduction in the centre of the array when only the transmission data of the total field is used in the reconstruction. In the reconstruction the defect location, size and depth are accurate. In the thickness profile the grey dotted line corresponds to the FE reconstruction using the same parameters. The FE and experimental profile are almost perfectly superposed. Therefore the artefacts in the reconstruction of figure 5.18 were due to the array of transducers.

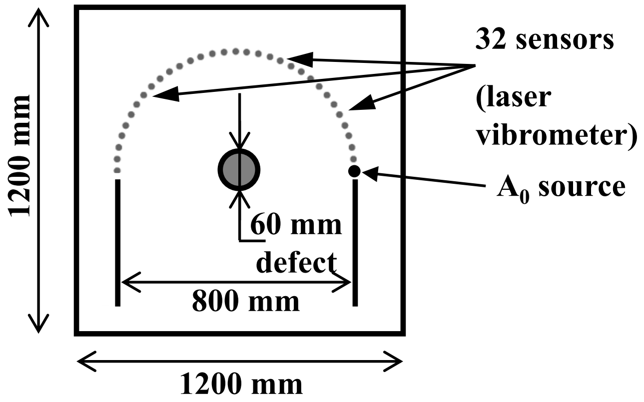

Figure 5.20: *Schematic of the measurement for a single defect in the centre of the array taking advantage of the symmetry of this case with one source location and 32 sensor locations measured with a Polytec laser vibrometer.*

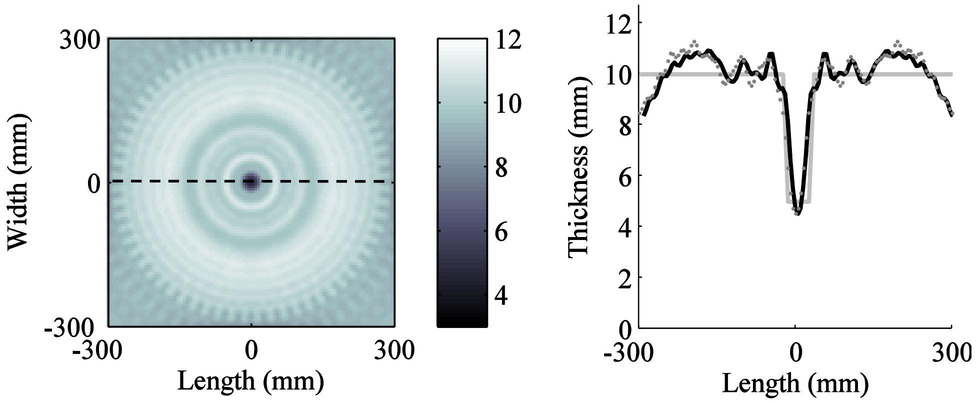

(*a*) (*b*)

Figure 5.21: *Experimental polychromatic diffraction tomography reconstruction between 45 and 55 kHz with one thickness reduction at the centre of the array and using only the transmission data of the total field. The measurement is carried out with a Polytec laser vibrometer. The defect has the same properties as figure 5.8. (a) Map of the reconstructed thickness and (b) thickness profile across the defect. The black line corresponds to the experimental reconstructed thickness profile, the grey dotted line to the FE reconstructed thickness profile and the grey line to the actual thickness profile.*

A similar measurement was performed with two defects within the array. In this case it was not possible to use symmetry to the same extent as in the single defect case and the source had to be moved for each measurement. There was therefore a variation in the coupling of the transducer with the plate between each measurement. From

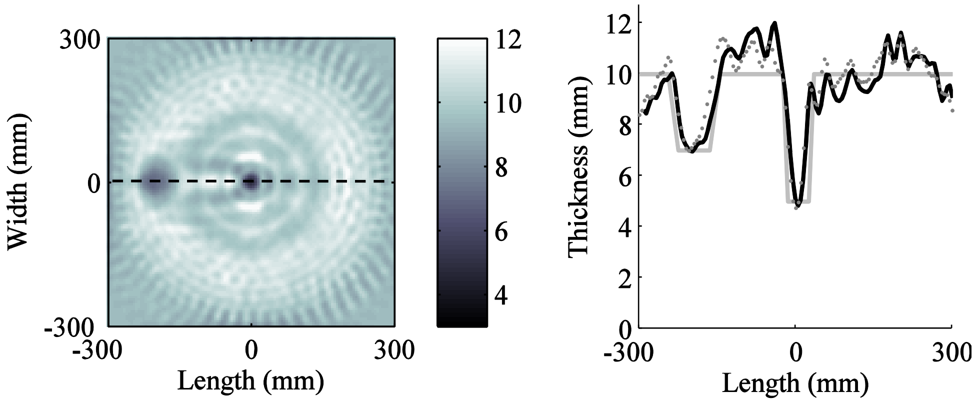

(*a*) (*b*)

Figure 5.22: *Experimental polychromatic diffraction tomography reconstruction between 45 and 55 kHz with two thickness reductions within the array and using only the transmission data of the total field. The measurement is carried out with a Polytec laser vibrometer. The defects have the same properties as figure 5.9. (a) Map of the reconstructed thickness and (b) thickness profile across the defect. The black line corresponds to the experimental reconstructed thickness profile, the grey dotted line to the FE reconstructed thickness profile and the grey line to the actual thickness profile.*

the amplitude of the recorded wave field, it was observed that this variation was up to 8 dB. The variation in the coupling of the source was not compensated for in the reconstruction. Figure 5.22 presents an experimental polychromatic reconstruction between 45 kHz and 55 kHz with two thickness reductions within the array when only the transmission data of the total field is used in the reconstruction. The experimental reconstruction is very similar to the FE reconstruction of figure 5.17. In the thickness profile the grey dotted line corresponds to the FE reconstruction using the same parameters. Once again the FE and experimental profile are almost identical. This therefore demonstrates that it is possible to reconstruct the thickness of a plate with low frequency guided waves by using only the transmission data of the total field when there is no scattering from the array of transducers.

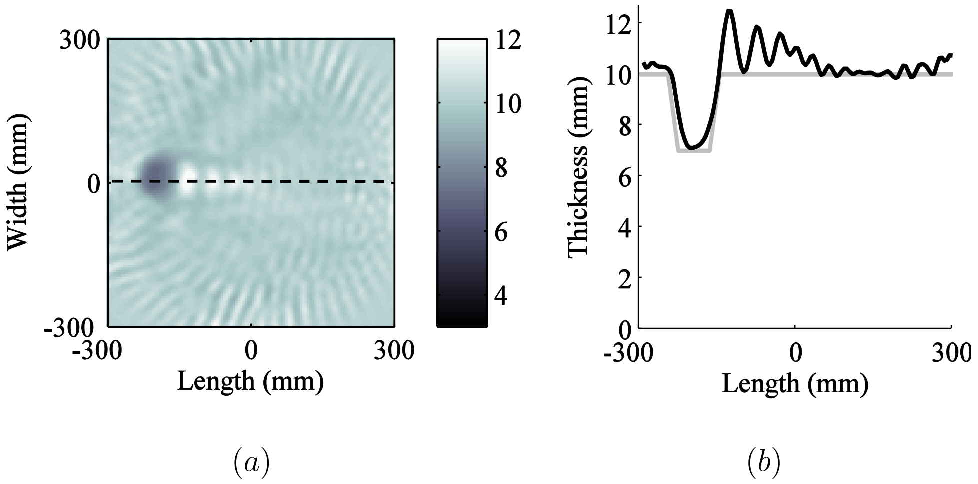

Figure 5.23: *Experimental polychromatic diffraction tomography reconstruction between 45 and 55 kHz with two thickness reductions within the array and using the measurement with the single defect in the centre of the array as the incident field in the evaluation of the Born approximation. The measurement is carried out with the array of transducers. The reconstructed defect is 30% deep and has a diameter of 100mm. (a) Map of the reconstructed thickness and (b) thickness profile across the defect. The black line corresponds to the experimental reconstructed thickness profile and the grey line to the actual thickness profile.*

Structural Health Monitoring Approach

Figure 5.23 presents an experimental polychromatic reconstruction between 45 kHz and 55 kHz with two thickness reductions within the array when the measurement with the defect in the centre of the array is used as the incident field in the evaluation of the Born approximation. The array of 64 bonded transducers was used for the the two measurements required in this case.

The location, size and depth of the defect are accurate. The large artefacts next to the reconstructed defect are due to the multiple scattering between the two defects. As expected the scattering from the array of transducers has no effect in this case because it is included in the measurement with the single defect in the centre of the array. Although structural health monitoring contains many challenges such as long term stability between measurements or transducer durability, low frequency guided wave tomography can potentially be used to detect and accurately size defects within an array of transducers.

5.5 Summary

Diffraction tomography can reconstruct a map of the velocity from the scattered field produced by the interaction of an incoming wave field and a velocity inhomogeneity. The velocity inhomogeneity has the same properties as the background medium except a different propagation velocity. Although a corrosion patch does not have all the same properties as a clean plate, this concept can be applied to guided waves if the point of operation, frequency and guided wave mode, is carefully selected.

It has been shown, with FE simulations and experiments, that low frequency guided waves can be used for thickness reconstruction of plates or large diameter pipes with diffraction tomography within the Born approximation. Multiple defects of diameter as small as 50 mm were accurately detected and sized in FE simulations. It has been demonstrated that an approximation of diffraction tomography within the Born approximation can be obtained by using only the transmission data of the total field. This is potentially very useful as thickness can be reconstructed over a large area of a plate or large diameter pipe from a single measurement of the total field. It has been shown that the scattering from the array of transducers needs to be minimised in order to reconstruct thickness accurately. However when the scattering from the array of transducers is large it is possible to use guided wave diffraction tomography in a structural health monitoring approach and obtain accurate thickness reconstruction.

Non contact transducers such as EMATs could potentially be used instead of the bonded piezoelectric devices used here. They would generate less scattering and should therefore improve the diffraction tomography thickness reconstruction.

Chapter 6

Conclusions

6.1 Thesis review

In this thesis the use of ultrasonic guided waves for thickness mapping of large, partially accessible areas was investigated. The problem of interest is to evaluate the minimum remaining plate thickness over a large area where the defects have a minimum diameter of 60 mm and the separation distance between the source and the sensor is approximately 1 m. Guided waves have multiple properties that can be used for thickness mapping over large areas.

Firstly, the dispersive nature, variation of the phase velocity as a function of the frequency thickness product, of guided waves make them potentially suitable for time-of-flight tomography and diffraction tomography based on the variation of the velocity in the inhomogeneities. In time-of-flight tomography the time that the mode of interest takes to propagate through a thickness reduction can be used to produce a map of the velocity which can be transformed into a map of the thickness with the dispersion curve of the mode of interest. Time-of-flight tomography will only work when the ray theory is valid. Guided wave time-of-flight tomography was investigated in chapter 3. Diffraction tomography on the other hand uses the scattered field produced by the interaction of the incoming wave field with an inhomogeneity in which the velocity of propagation is different from the velocity of propagation in the background medium to reconstruct a map of the velocity. This map can also be transformed into a map of thickness with the dispersion curve of the mode of interest. Diffraction tomography was examined in chapter 5.

Secondly, the cutoff property of the high order modes can potentially be used to estimate the minimum remaining thickness between a source and a sensor. The significance of the high order modes cutoff property is that if a thickness reduction is present along the propagation path such that the frequency thickness product was shifted below the cutoff frequency thickness product of a given mode, then no energy of that mode would propagate through the thickness reduction. Therefore by identifying which modes are detected after propagation through an area of inspection it is possible to work out the minimum remaining thickness in the propagation path. The cutoff property of the high order modes was studied in chapter 4

6.2 Main findings of this thesis

6.2.1 Time-of-flight Tomography

In time-of-flight tomography the idea is to use the dispersive nature of the guided waves to generate a map of the thickness. For this technique to work, the point of operation, frequency and guided wave mode, needs to be carefully selected. Two points of operation were identified below the cutoff of the higher order modes using three criteria: the velocity sensitivity to thickness change, the mode excitability and detectability and the attenuation due to fluid loading. If fluid loading is taken into account, S_0 at a frequency around 1.75 MHz-mm, where the velocity difference between S_0 and the other modes is still high, is the best choice provided the propagation distances before and after the defect are long enough for the wave packets to separate. However when there is no fluid loading, the 40 dB difference in normal excitability and detectability shifts the choice to A_0 at a frequency around 0.5 MHz-mm.

It has been shown, with FE simulations and experiments, that these points of operation cannot be used for time-of-flight straight-ray tomography to evaluate the maximum depth of defects of the diameter of interest in practice due to the invalidity of the ray theory. When the ray theory is violated the incident and scattered signals interfere which changes the received wave packet and thus makes the time-of-flight calculations inaccurate.

If the propagation distance is reduced, the ray theory becomes valid in the low frequency regime, but the required reduction is too large to be of practical use. The characteristic size of the defect can also be increased to satisfy the ray theory but again this is not of interest in practical applications.

6.2.2 Guided Wave Mode Cutoff for Thickness Gauging

Fundamentally the presence of corrosion is simply a change in the waveguide thickness. A guided wave mode will only propagate through a thickness reduction if at the minimum thickness the corresponding frequency thickness product is above the cutoff frequency thickness product of this mode. Therefore by exciting multiple guided wave modes with a source it may be possible to get an approximation of the minimum thickness along the propagation path if the modes that propagated through the reduced thickness area are identified. A novel approach using the validity of the ray theory to select the frequency of excitation was proposed. The investigation was carried at a frequency of 2 MHz in a 10 mm aluminium plate. This frequency was chosen based on the validity of the ray theory to detect a 60 mm diameter defect over a propagation distance of 1 m. The validity of the ray theory ensures that the signal is detected by a sensor without superposition from the interaction of the waves with features outside of the ray path.

2D plane strain FE simulations have shown that it is possible to use SH waves at around 2 MHz with two 16 element arrays for excitation and detection of the signals to obtain an estimation of the minimum remaining thickness in the path between the two arrays. The guided wave modes are identified by performing a 2D Fourier transform of the data received by the sensor array.

The experimental results obtained on 30% and 50% machined defects gave results that were significantly different from the FE predictions. In the experimental results, in contrast with the FE predictions, the amplitude of the guided wave mode clusters relative to the maximum amplitude of the 2D Fourier transform does not appear to be related to the minimum remnant thickness between the two transducers. One likely reason for this is that the ray theory approximation may not be valid in this case because the length of the signals recorded is too long. Therefore the slowest excited modes superpose with the interaction of the fastest excited modes with features outside of the ray path e.g. other defects or plate boundaries. Moreover the integrated amplitude of the cluster relative to the no defect case was not consistent with the depth of the defect. This is potentially due to the difference in surface roughness of the two defects studied. More importantly it was shown that virtually no energy is propagating through a 50% deep accelerated corrosion patch at 2 MHz. Therefore the attenuation of SH waves around 2 MHz due to severe corrosion is too high to be of practical interest if the required propagation distance is of the order of 1 m and this approach was abandoned.

6.2.3 Guided Wave Diffraction Tomography

Diffraction tomography can reconstruct a map of the velocity from the scattered field produced by the interaction of an incoming wave field and a velocity inhomogeneity. The velocity inhomogeneity must have all the same properties as the background medium except a different propagation velocity. Although a corrosion patch does not have all the same properties as a clean plate, this concept can be applied to guided waves if the point of operation is carefully selected. In the diffraction tomography investigation the points of operation were the same as for time-of-flight tomography.

It has been shown, with FE simulations and experiments, that low frequency guided waves can be used for thickness reconstruction of plates or large diameter pipes with diffraction tomography within the Born approximation. Multiple defects of diameter as small as 50 mm were accurately detected and sized in FE simulations in a 10 mm plate. It has been demonstrated that an approximation of diffraction tomography within the Born approximation can be obtained by using only the transmission data of the total field. This is potentially very useful as thickness can be reconstructed over a large area of a plate or large diameter pipe from a single measurement of the total field. It has been shown that the scattering from the array of transducers needs to be minimised in order to reconstruct thickness accurately. However when the scattering from the array of transducers is large it is possible to use guided wave diffraction tomography in a structural health monitoring approach and obtain accurate thickness reconstruction.

6.3 Suggestions of future work

A considerable amount of work is required before implementing diffraction tomography in the field. In the experimental implementation of guided wave diffraction tomography in chapter 5 the scattering from the array of transducers was shown to generate large artefacts in the thickness reconstruction. Non contact transducers such as EMATs could potentially be used instead of the bonded piezoelectric devices used here. They would generate less scattering and should therefore improve the diffraction tomography thickness reconstruction.

The algorithm used in chapter 5 was developed for circular array applications. The circular array geometry is not suitable for pipe inspection. In a pipe inspection the idea is to use two rings of transducers on either side of the area that needs inspection. The algorithm required for this application is very similar to the one used in geophysical tomography with the crosshole scanning geometry as explained in chapter 2. The main difference between the crosshole scanning geometry in geophysics and its implementation on pipe is the infinite number of circumferential guided wave modes that can propagate around the pipe. The direction of propagation of these circumferential modes around the pipe would need to be taken into account as it will carry the information regarding the location of the defects.

All the FE and experimental results presented in chapter 5 were valid within the Born approximation. The Born approximation becomes invalid when the phase change through the defect is too large. In guided wave diffraction tomography for thickness reconstruction the phase change in the defect is a function of the defect depth and diameter as well as the level of dispersion at the point of operation. The more dispersive the mode of interest is around the frequency of excitation the larger the phase change is in a thickness reduction. It is therefore possible to choose a less dispersive point of operation when inspecting deep corrosion. However this is not practical. Section 5.3.1 showed that the Rytov approximation is valid over a wider range of inhomogeneities but its implementation is more difficult. The Rytov approximation is potentially better suited to guided wave diffraction tomography for thickness reconstruction if a reliable phase unwrapping algorithm can be used. However before using the Rytov approximation in industrial applications it would be required to investigate the possibility to avoid using the incident field in the evaluation of the approximation as was shown in section 5.4.2 for the Born approximation.

References

[1] J. Krautkramer and H. Krautkramer. *Ultrasonic Testing of Materials*. Springer, Berlin, 1969.

[2] B.A. Auld and J.C. Moulder. Review of advances in quantitative eddy current nondestructive evaluation. *Journal of Nondestructive Evaluation*, 18(1):3–36, 1999.

[3] D. Alleyne, M. Lowe, and P. Cawley. The reflection of guided waves from circumferential notches in pipes. *Journal of applied mechanics*, 65:635–641, 1998.

[4] D. Alleyne, B. Pavlakovic, M. Lowe, and P. Cawley. Rapid, long range inspection of chemical plant pipework using guided waves. *Insight*, 43(2):93–96, 2001.

[5] P. Mudge. Field application of the teletest long range ultrasonic testing technique. *Insight*, 43(2):74–77, 2001.

[6] P. Cawley, M.J.S. Lowe, D.N. Alleyne, B. Pavlakovic, and P. Wilcox. Practical long range guided wave testing: Applications to pipes and rail. *Material evaluation*, 61(1):66–75, 2003.

[7] A. Demma, P. Cawley, M. Lowe, A. G. Roosenbrand, and B. Pavlakovic. The reflection of guided waves from notches in pipes: A guide for interpreting corrosion measurements. *NDT and E International*, 37(3):167–180, 2004.

[8] J. Fong and M.J.S. Lowe. Curvature effect on the properties of guided waves in plates. In D. Chimenti and D. Thompson, editors, *Review of Progress in*

Quantitative Nondestructive Evaluation, volume 23, pages 126–133, Green Bay, WI, USA, 2004. AIP.

[9] Lord Rayleigh. On the free vibrations of an infinite plate of homogeneous isotropic elastic matter. *Proc. Lond. Math. Soc.*, 20:225–237, 1888.

[10] H. Lamb. On waves in an elastic plate. *Proceedings of the Royal Society of London*, 93(648):114–128, 1917.

[11] R. Stoneley. Elastic waves at the surface of separation of two solids. *Proceedings of the Royal Society of London*, 106(738):416–428, 1924.

[12] L.M. Brekhovskikh. *Waves in layered media.* Academic Press, 1980.

[13] K.F. Graff. *Wave Motion in Elastic Solids.* Dover Publications inc., 1991.

[14] J.L. Rose. *Ultrasonic Waves in Solid Media.* Cambridge Univeristy Press, 1999.

[15] B.A. Auld. *Acoustic fields and waves in solids.* Krieger Publishing Company, 1990.

[16] L.M. Brekhovskikh and V. Goncharov. *Mechanics of continua and wave dynamics.* Springer-Verlag, 1985.

[17] D. Alleyne and P. Cawley. The long range detection of corrosion in pipes using lamb waves. In D. Chimenti and D. Thompson, editors, *Review of Progress in Quantitative Nondestructive Evaluation*, volume 14, pages 2073–2080, Snowmass Village, CO, USA, 1994. Plenum Press.

[18] P. Wilcox, M. Lowe, and P. Cawley. Long range lamb wave inspection: The effect of dispersion and modal selectivity. In D. Chimenti and D. Thompson, editors, *Review of Progress in Quantitative Nondestructive Evaluation*, volume 18, pages 151–158, Snowbird, UT, USA, 1999. Plenum Press.

[19] B. Pavlakovic, M. Lowe, D. Alleyne, and P. Cawley. Disperse: A general purpose program for creating dispersion curves. In D. Chimenti and D. Thompson, editors, *Review of Progress in Quantitative NDE*, volume 16, pages 185–192, San Diego, CA, USA, 1997. AIP.

[20] J. Radon. Über die bestimmung von funktionen durch ihre integralwerte längs gewisser mannigfaltigkeiten. *Berichte Sächsische Akademie der Wissenschaften*, 69:262–267, 1917.

[21] A. Kak and M. Slaney. *Principles of Computerized Tomography Imaging.* IEEE Press, 1988.

[22] G.N. Ramachandran and A.V. Lakshminarayanan. Three-dimensional reconstruction from radiographs and electron micrographs: Application of convolutions instead of fourier transforms. *Proc. Nat. Acad. Sci.*, 68:2236–2240, 1971.

[23] L.A. Shepp and B.F. Logan. The fourier reconstruction of a head section. *IEEE Trans. Nucl. Sci*, NS-21:21–43, 1974.

[24] D. P. Jansen and D. A. Hutchins. Lamb wave tomography. IEEE 1990 Ultrasonics Symposium Proceedings (Cat. No.90CH2938-9), pages 1017–20, Honolulu, HI, USA, 1990. IEEE.

[25] D. A. Hutchins, D. P. Jansen, and C. Edwards. Non-contact lamb wave tomography. IEEE 1992 Ultrasonics Symposium (Cat. No.92CH3118-7), pages 883–6, Tucson, AZ, USA, 1992. IEEE.

[26] W. Wright, D. Hutchins, D. Jansen, and D. Schindel. Air-coupled lamb wave tomography. *IEEE Transactions on Ultrasonics, Ferroelectrics and Frequency Control*, 44(1):53–9, 1997.

[27] J. Pei, M. I. Yousuf, F. L. Degertekin, B. V. Honein, and B. T. Khuri-Yakub. Lamb wave tomography and its application in pipe erosion/corrosion monitoring. *Research in Nondestructive Evaluation*, 8(4):189–197, 1996.

[28] B.T. Khuri-Yakub, Sanjay Bhardwaj, and Krishna Saraswat. Thin film process monitoring techniques using acoustic waves. *United States Patent*, (5,271,274), 1993.

[29] J. C. P. McKeon and M. K. Hinders. Parallel projection and crosshole lamb wave contact scanning tomography. *Journal of the Acoustical Society of America*, 106(5):2568–77, 1999.

[30] E. V. Malyarenko and M. K. Hinders. Fan beam and double crosshole lamb wave tomography for mapping flaws in aging aircraft structures. *Journal of the Acoustical Society of America*, 108(4):1631–9, 2000.

[31] K. R. Leonard and M. K. Hinders. Guided wave helical ultrasonic tomography of pipes. *Journal of the Acoustical Society of America*, 114(2):767–74, 2003.

[32] K. R. Leonard and M. K. Hinders. Lamb wave tomography of pipe-like structures. *Ultrasonics*, 43(7):574–83, 2005.

[33] E. V. Malyarenko and M. K. Hinders. Ultrasonic lamb wave diffraction tomography. *Ultrasonics*, 39(4):269–81, 2001.

[34] H. Hochstadt. *Integral Equations.* John Wiley and Sons, 1973.

[35] D. Colton and R. Kress. *Integral Equation Methods in Scattering Theory.* John Wiley and Sons, 1983.

[36] L.A. Chernov. *Wave Propagation in a Random Medium.* McGraw-Hill, 1960.

[37] J.B. Keller. Accuracy and validity of the born and rytov approximations. *Journal of the Optical Society of America*, 59:1003–1004.

[38] A.H. Rohde, M. Veidt, L.R.F. Rose, and J. Homer. A computer simulation study of imaging flexural inhomogeneities using plate-wave diffraction tomography. *Ultrasonics*, 48:6–15, 2008.

[39] J.L. Rose and J.N. Barshinger. Using ultrasonic guided wave mode cutoff for corrosion detection and classification. In *IEEE Ultrasonics Symposium*, volume 1, pages 851–854. IEEE, 1998.

[40] W. Zhu, J.L. Rose, J.N. Barshinger, and V.S. Agarwala. Ultrasonic guided wave ndt for hidden corrosion detection. *Research in Nondestructive Evaluation*, 10:205–225, 1998.

[41] M. Z. Silva, R. Gouyon, and F. Lepoutre. Hidden corrosion detection in aircraft aluminum structures using laser ultrasonics and wavelet transform signal analysis. *Ultrasonics*, 41(4):301–5, 2003.

[42] D. Tuzzeo and F. Lanza di Scalea. Noncontact air-coupled guided wave ultrasonics for detection of thinning defects in aluminium plates. *Research in Nondestructive Evaluation*, pages 61–77, 2001.

[43] Geir Instanes, Lakshminarayan Balachander, Mads Toppe, and P. B. Nagy. The use of non-intrusive ultrasonic intelligent sensors for corrosion and erosion monitoring. In *Offshore Europe 2005*, Aberdeen, 2005. Society of Petroleum Engineers.

[44] P. Wilcox, M. J. S. Lowe, and P. Cawley. Mode and transducer selection for long range lamb wave inspection. *Journal of Intelligent Material Systems and Structures*, 12(8):553–65, 2001.

[45] W. Menke and D. Abbott. *Geophysical Theory.* Columbia University Press, 1990.

[46] V. Červenỷ. *Seismic Ray Theory.* Cambridge Univeristy Press, 2001.

[47] F. E. Ernst and G. C. Herman. Tomography of dispersive media. *Journal of the Acoustical Society of America*, 108(1):105–16, 2000.

[48] Jidong Hou, Kevin R. Leonard, and Mark K. Hinders. Automatic multi-mode lamb wave arrival time extraction for improved tomographic reconstruction. *Inverse Problems*, 20(6):1873–1888, 2004.

[49] M. Drozdz, L. Moreau, M. Castaings, M.J.S. Lowe, and P. Cawley. Efficient numerical modelling of absorbing regions for boundaries of guided waves problems. In D. Chimenti and D. Thompson, editors, *Review of Progress in Quantitative Nondestructive Evaluation*, volume 25, pages 126–133, Brunswick, ME, USA, 2006. AIP.

[50] M. Drozdz, E. Skelton, R.V. Craster, and M.J.S. Lowe. Modeling bulk and guided waves in unbounded elastic media using absorbing layers in commercial finite element packages. In D. Chimenti and D. Thompson, editors, *Review of Progress in Quantitative Nondestructive Evaluation*, volume 26, pages 87–94, Portland, OR, USA, 2007. AIP.

[51] J. Spetzler and R. Snieder. The effect of small-scale heterogeneity on the arrival time of waves. *Geophysical Journal International*, 145(3):786–96, 2001.

[52] D.W. Vasco, J.E. Peterson, and E.L. Majer. Beyond ray tomography: Wavepaths and fresnel volumes. *Geophysics*, 60(6):1790–1804, 1995.

[53] T. Clarke, F. Simonetti, S. Rohklin, and P. Cawley. Development of a low-frequency high purity a_0 mode transducer for shm applications. *IEEE Transactions on Ultrasonics, Ferroelectrics and Frequency Control*, 56(7):1457–1468.

[54] Wilcox P.D. Cawley P. Monkhouse, R.S.C. Flexible interdigital pvdf transducers for the generation of lamb waves in structures. *Ultrasonics*, 35:489–498, 1997.

[55] D. Alleyne and P. Cawley. A two-dimensional fourier transform method for the measurement of propagating multimode signals. *Journal of the Acoustical Society of America*, 89(3):1159–68, 1991.

[56] P. Cawley and F. Cegla. Ultrasonic Non-Destructive Testing, European Patent EP1954413, 14 September 2006.

[57] F. Cegla. Ultrasonic crack monitoring using sh waves in extreme and inaccessible environments. In *17th World Conference on Nondestructive Testing*, 2008.

[58] D.E. Chimenti and O.I. Lobkis. Effect of rough surfaces on guided waves in plates. In D. Chimenti and D. Thompson, editors, *Review of Progress in Quantitative Nondestructive Evaluation*, volume 17, pages 129–136, San Diego, CA, USA, 1998. Plenum Press.

[59] P. P. Ewald. Introduction to the dynamical theory of X-ray diffraction. *Acta Crystallographica Section A*, 25(1):103–108, 1969.

[60] F. Simonetti, L. Huang, N. Duric, and P. Littrup. Diffraction and coherence in breast ultrasound tomography: A study with a toroidal array. *Medical Physics*, 36:2955–2965, 2009.

[61] F. Simonetti and L. Huang. From beamforming to diffraction algorithm. *Journal of Applied Physics*, 103:103110, 2008.

[62] F. Simonetti, L. Huang, and N. Duric. On the spatial sampling of wave fields with circular ring apertures. *Journal of Applied Physics*, 101:083103, 2007.

[63] F. Simonetti, L. Huang, and N. Duric. Transmission and reflection diffraction tomography in breast imaging. In *International Conference on BioMedical Engineering and Informatics*, volume 2, pages 723–272, 2008.

List of Publications

[P1] P. Belanger and P. Cawley. Lamb wave tomography to evaluate the maximum depth of corrosion patches. In D. O. Thompson and D. E. Chimenti, editors, *Review of Progress in Quantitative NDE*, volume 27, pages 1290-1297, Golden, CO, USA. 2008. AIP.

[P2] P. Belanger and P. Cawley. Feasibility of Low-Frequency Straight-Ray Guided Wave Tomography. In D. O. Thompson and D. E. Chimenti, editors, *Review of Progress in Quantitative NDE*, volume 28, pages 153-160, Chicago, IL, USA. 2009. AIP.

[P3] P. Belanger and P. Cawley. Feasibility of low frequency straight-ray guided wave tomography. NDT & E International, vol. 42 (2), 2009, pp. 113-119.

[P4] P. Belanger and P. Cawley. Lamb wave tomography to evaluate the maximum depth of corrosion patches. In D. O. Thompson and D. E. Chimenti, editors, *Review of Progress in Quantitative NDE*, In Press.

[P5] P. Belanger and P. Cawley. Feasibility of low frequency straight-ray guided wave tomography. Submitted to IEEE Trans. Ultrason. Ferroelectr. Freq. Control.